Ion Spectroscopies for Surface Analysis

Edited by

A. W. Czanderna

Solar Energy Research Institute
Golden, Colorado

and

David M. Hercules

University of Pittsburgh
Pittsburgh, Pennsylvania

PLENUM PRESS • NEW YORK AND LONDON

Surface Structure and Reaction Studies by Ion–Solid Collisions

Nicholas Winograd and Barbara J. Garrison

1. Introduction

Bombardment of targets by energetic particle beams has become an important tool for the characterization and modification of solids and surfaces. With this approach, the kinetic energy of the primary particle, typically a few eV to a few thousand eV, exceeds the binding interactions normally present in chemical bonds. Because of this energy difference, a novel and intriguing chain of events is rapidly set in motion subsequent to the impact event. Atoms may be significantly displaced from their equilibrium positions. Original chemical bonds may be broken with new ones formed. Energetic collisions may give rise to electronic excitation, ionization, and desorption of atomic or molecular components of the bombarded solid.

These phenomena have led to important applications. A major impetus for research has been, of course, in the microelectronics area, where ion implantation of dopant ions[1] and reactive ion etching of semiconductors are hot topics.[2] There is also interest in evaluating surface processes which occur when energetic ions and molecules present

Nicholas Winograd and Barbara J. Garrison • Department of Chemistry, Pennsylvania State University, University Park, Pennsylvania 16802.

Ion Spectroscopies for Surface Analysis (Methods of Surface Characterization series, Volume 2), edited by Alvin W. Czanderna and David M. Hercules. Plenum Press, New York, 1991.

in the space environment impinge on a diverse array of synthetic materials ranging from light metallic composites to protective polymer overlayers deposited on nonlinear optical materials.[3] The morphology of extraterrestrial surfaces is believed to be dominated to some degree by interaction with the solar wind or other energetic ions.[4]

Other applications involve an analysis of the primary particle or of the desorbed material. Examination of the fate of the scattered primary particle forms the basis of ion scattering spectrometry (ISS) in the 10–10,000-eV range and Rutherford backscattering at still higher energies. These are important structural tools since the scattering trajectories are strongly influenced by the nuclear positions of surface atoms. Both approaches are extensively utilized as surface analytical techniques. Complete reviews of both of these ion-beam methods are presented by Taglauer in Chapter 6 and Feldman in Chapter 5.

Measurement of the intensity and mass of the ions that desorb from the surface forms the basis of secondary ion mass spectrometry (SIMS). Since the initial observation of these ions by J. J. Thomson n 1910,[5] this field has expanded almost exponentially. Currently, SIMS is widely utilized in trace analysis in combination with depth profiling of the near surface region.[6] This profiling is accomplished by eroding the surface layers of the target using the same energetic particle used to produce the secondary ions. It is also possible to produce spectacular element-specific images of surfaces with a spatial resolution below 100 nm using either a highly focused, rastered ion beam[7] or a specially designed imaging detector.[8]

Perhaps the most important aspect of SIMS for chemical analysis is that many of the desorbed ions may be molecular in nature and may reflect the composition of the bombarded surface. Since Benninghoven[9] suggested that these experiments be performed at very low ion doses—before the surface composition is significantly altered—it has been found that a vast array of normally nonvolatile molecules may be desorbed intact, without significant fragmentation. Similar observations have been made from bombarded liquid targets, even at higher doses.[10] The weight of some molecular ions has exceeded 10,000 amu.[11] These species are now detectable, largely because of the highly sensitive time-of-flight (TOF) detectors also being developed by the Benninghoven group.[12] It is an apparent paradox that fragile, heavy molecules such as insulin thermally decompose at slightly elevated temperatures, yet desorb intact when the solid is belted with a keV particle. A complete discussion of these topics by Busch is included in Chapter 3. As a bonus to all of this, the desorption occurs specifically from surface layers,[13] opening important applications in catalysis studies where it may be possible to directly identify heterogeneous reaction intermediates.

Detection of the desorbed neutral material from bombarded solids dates to the 1850s where erosion of cathodes in gas discharge sources was of concern.[14] Although we find the term most offensive, this desorption is commonly referred to as "sputtering." The study of this phenomenon was thought to be important to gain a fundamental picture of the particle/solid interaction. Early experimental results were of dubious value, however, owing to poor vacuum conditions and inefficient detection schemes. During the last 10 years, several new approaches using methods whereby the desorbed neutral species is ionized either by plasma,[15] electron,[16] or laser[17] has basically solved the detection problem. In fact, as Becker points out in Chapter 4, the most sensitive surface analyses are now performed with desorbed neutral species. High-quality measurements are now posible which finally are yielding to their promise of providing data directly comparable to theory. In addition, this development perhaps offers a new direction for explosive research growth leading to even more particle/solid interaction applications.

Although these experiments have certainly had a diverse and important impact on materials science research, it is apparent that the details of the particle-impact event are very complicated. In fact, at first glance, it might appear that it is not possible to go beyond the simple "hand-waving" stage. After one of our lectures, a doubting observer referred to our experiments as "hand-grenade science." A major goal of this chapter, then, is to convince the reader that there is, indeed, a great deal known about the nuclear motion that leads to radiation damage and desorption. Further, there are impressive attempts to quantitatively understand the basis for electronic excitation and ionization. The tools for leap-frogging beyond the hand-waving stage are at least with us, if not completely developed.

The basic idea behind our strategy of gaining an atomic-level understanding of this process is illustrated by examining the possible parameters that are measurable and calculable. These are shown schematically in Fig. 1. The incident particle is usually ionized,[18]

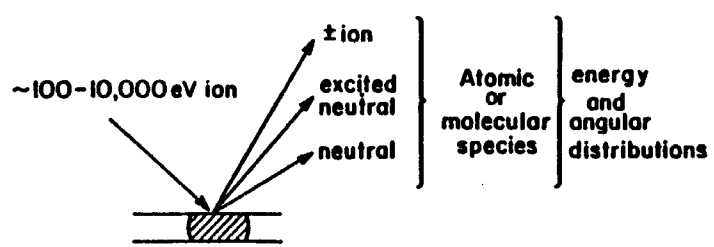

Figure 1. Representation of the experimental geometry of a typical ion–solid interaction experiment with important measurable quantities.

accelerated and directed at a specific incident angle toward the target. As we have mentioned, the kinetic energy of this particle initiates atomic motion near the point of impact. A portion of these atoms may have a momentum component that is directed away from the target and thus desorption of various species is observed to occur. Note also that radiation damage resulting in chemical modification of the surface region is an integral part of the bombardment process. From the figure, however, it is apparent that there is a wealth of experimental information potentially available to help us fully understand the dynamics of this complex event. Particles may desorb by way of a variety of channels to produce ground state and excited state neutral atoms, positive or negative ions as well as a multitude of molecular cluster species. Of particular importance is that each component possesses its own kinetic energy and angular distribution. These distributions play an essential role in validating proposed theories of either the nuclear motion or of the electronic excitation. It is our view that predictions of an angle-integrated and/or a kinetic energy-integrated quantity are not sufficient for such validation.

The focus of this chapter will be quite narrow relative to the wide scope of this field. We shall concentrate only on developing ideas and experiments that can yield quantitative comparisons between experiment and theory and shall emphasize those applications that translate directly into new insights into the chemistry or structure of surfaces. We shall try as hard as we can to avoid any hand-waving discussions and will only present the formalism behind fairly rigorous approaches. Specifically, we will be interested in presenting techniques that can perform detailed trajectory measurements for most of the reaction channels given in Fig. 1. A critical theme will be to emphasize the interrelationship of all these observables and to develop the best theoretical and experimental approaches that result in quantitative models for each process. We will begin with a discussion of the relevant experimental tools that are needed to obtain the information in Fig. 1. We will next provide a short review of the theory of sputtering, followed by an extensive development of the use of computer simulations to model the nuclear motion near the point of impact of the primary ion. A discussion of the current state of the theory of excitation and ionization will precede a section on the application of these ideas to problems of particular relevance to surface science.

2. The Experimental Approach

Within our narrow focus, the experimental goals are painfully clear. The target should be a well-characterized single crystal so that the initial

atomic locations are as well known as possible. The particle beam source should be flexible with regard to incident energy, mass, and angle. The detector must be able to count desorbed particles with doses well below that of the number of surface atoms or molecules. Ideally, the device should also be able to selectively detect ionic and neutral components in ground and excited states and to resolve energy and angular distributions. It is with these measurements that theories can be carefully checked, the implications of beam methods for surface structure studies can be fully assessed, and the analytical and technological uses can be exploited to the maximum extent.

Through the early 1960s, experiments were restricted largely to weight-loss measurements on uncharacterized single-crystal surfaces.[19] After this time, a rapid series of advances greatly expanded our understanding of this process. Mass spectrometric detectors became popular for detection of secondary ions.[20] At about the same time, Thompson reported his elegant time-of-flight experiments performed on ejected neutral atoms to yield velocity measurements.[21] The legendary work of Wehner to unravel many angular distribution patterns from single crystals and his fluorescence technique to obtain velocity distributions still has an enormous influence on present day designs.[22] Yet all of these experiments were performed using poor vacuums and high incident ion doses. Electron micrographs of the experimental surfaces with the eery morphological features left one somewhat uneasy.[23]

Two critical developments from Benninghoven's laboratory sparked the development of modern experiments. First, he showed that using mass spectrometric detectors in the SIMS mode, a measurable signal could be obtained from just $\sim 10^{12}$ incident ions/cm^2.[9] This observation allowed the study of monolayers by bombarding only 1 in a thousand surface atoms—a configuration he termed "static" SIMS since the surface condition remained unchanged to the observer during the time of measurement.

His second major contribution was that he noted the appearance of organic molecular ions in these static SIMS spectra which were representative of the organic surface under investigation.[24] These early studies have, of course, given way to fast atom bombardment (FAB) measurements[10,18] with all their associated hoopla. The relevant experimental details for these studies are given in Chapter 3.

No apparatus yet exists that satisfies all of our initial measurement criteria. Advances in experimental surface science during the 1970s allowed major progress in this direction, however. A first attempt at performing detailed trajectory measurements in UHV under static-mode conditions was first initiated about 8 years ago.[25] This apparatus, shown in Fig. 2, is capable of detecting a wide variety of azimuthal and polar

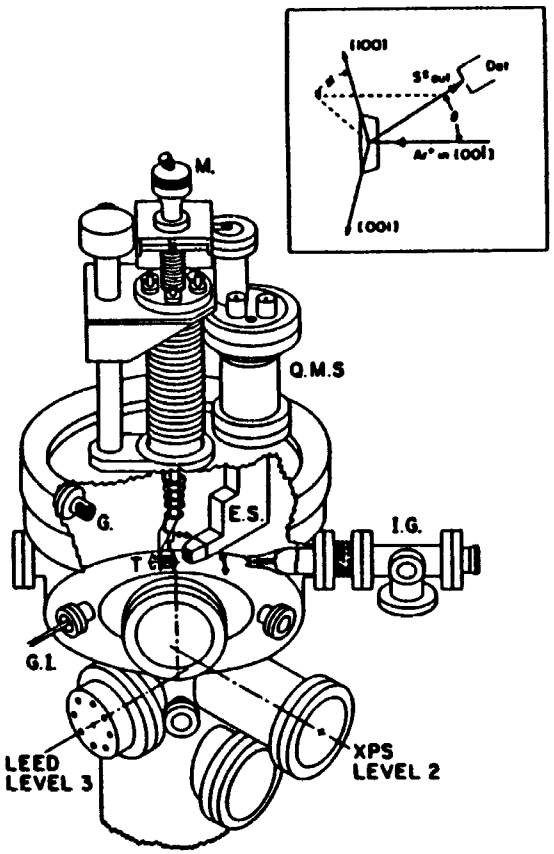

Figure 2. Schematic view of the spectrometer. The components illustrated include M, crystal manipulator; Q.M.S., quadrupole mass spectrometer; I.G., primary ion source; E.S., energy spectrometer; G, Bayard–Alpert gauge; T, crystal target; and G.I., gas inlet. Auxiliary components are omitted for graphical clarity. The SIMS experimental geometry and coordinate system are defined in the inset. (From Ref. 25.)

angles for a normally incident beam. The detector is a quadrupole mass spectrometer that could be rotated under UHV conditions with respect to the incident ion beam. Moreover, a medium resolution energy selector consisting of a 90° sector provides the capability of examining how the angular distributions change with secondary ion energy. The chamber was designed with two levels. The SIMS measurements are performed on the top level while LEED/Auger/XPS analysis could be obtained by vertically translating the sample to a lower level. This instrument has been very successful in providing ion trajectory data, as presented in the

next sections, and has yielded a measure of understanding about differences in behavior between ions and the predicted behavior of the neutral flux obtained from molecular dynamics simulations. It provides no information about neutral trajectories nor does it yield state-selective information about electronically excited species.

The neutral data are potentially obtainable using efficient postionization sources to excite the atom or molecule after it has desorbed from the surface but before it has reached the detector. The first promising experiments involving lasers utilized fluorescence spectroscopy to probe these species.[26] The wavelengths of the fluorescence could be tied to the original electronic states of the desorbing atoms. As a bonus, the speed of the desorbing component could be determined by measuring its Doppler shift.[27] Unfortunately, this method was never sufficiently sensitive to be utilized in the static mode. Other schemes, including efficient electron impact ionization of the desorbed particles[16] and low-energy plasma ionization[15] offer the potential for static measurements on monolayers. As of yet, however, the necessary sensitivity does not appear to have been demonstrated.

Laser-induced ionization overcomes many of the deficiencies of current approaches. Successful experiments have been possible using both multiphoton resonance ionization (MPRI)[17] and nonresonant ionization.[28] These methods are described in detail by Becker in Chapter 4. Here, we summarize only several inherent advantages of MPRI detection specific to carrying out ion beam experiments on well-defined surfaces. First, a pulsed laser is used to create ions from the ejected neutral species. This pulse generates an ideal timing signature for time-of-flight (TOF) detection, one of the most efficient mass analysis techniques. Secondly, MPRI requires relatively low power to achieve nearly 100% ionization efficiency. This means that the laser beam may be quite large in size, permitting the spatial imaging of subsequently ionized species. Finally, MPRI is highly selective. Using tunable dye lasers, it is possible to excite only those atoms whose electronic spacings match the laser frequency. This aspect of MPRI means that it is possible to achieve extremely low background signals and to accurately count just a few particles.

A schematic diagram of an instrument designed to measure both the energy- and angle-resolved neutral (EARN) distributions[29] is shown in Fig. 3. The sample is placed in the top level of a two-level chamber similar in design to that shown in Fig. 2. This level is equipped with quartz laser ports, the EARN detector, and a differentially pumped pulsed ion gun. The bottom level is equipped in the usual fashion with Auger/LEED for auxiliary surface analysis. The tunable photon radiation

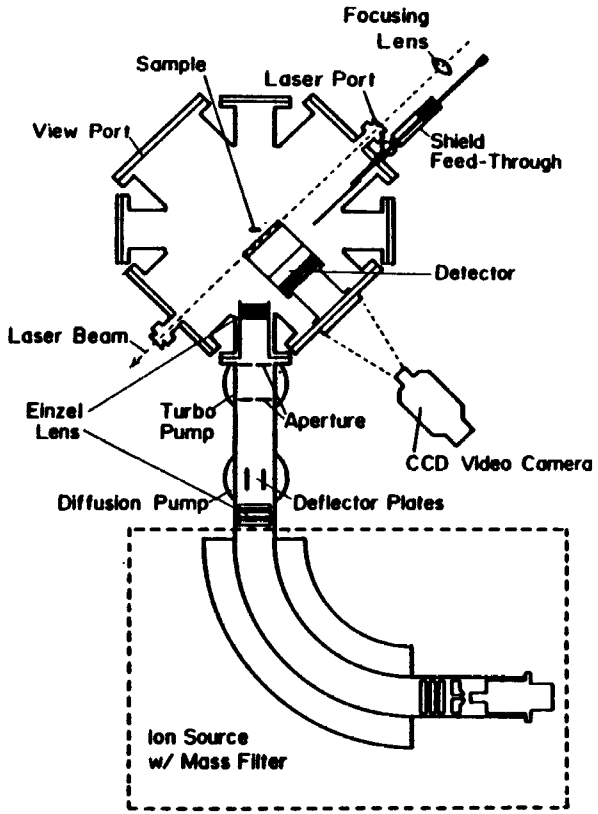

Figure 3. Schematic cross section of the EARN apparatus. The sample is shown in the position for normal-incident ($\theta_i = 0°$) ion bombardment. Not drawn to scale. (From Ref. 29.)

is generated using commercially available dye lasers pumped by a Q-switched Nd:YAG laser. This laser system is equipped with standard nonlinear optical mixing capabilities so that tunability over the range of 2–7 eV is possible. The resulting radiation takes the form of a 6-ns pulse which is repeated at a rate of up to 30 Hz. The laser beam itself is reshaped from an initial 0.5-cm circular configuration to a 0.1-cm-thick ribbon using a 225-cm local length cylindrical lens. Note that it is positioned about 1.5 cm above and parallel to the target.

The timing scheme for the EARN experiments is critical and is shown schematically in Fig. 4. In general terms, the experiment proceeds as follows: (i) A 200-ns pulse of approximately 2.5×10^6 ions is focused to a 2-mm spot on the sample; (2) upon impact of the ion pulse, an ion

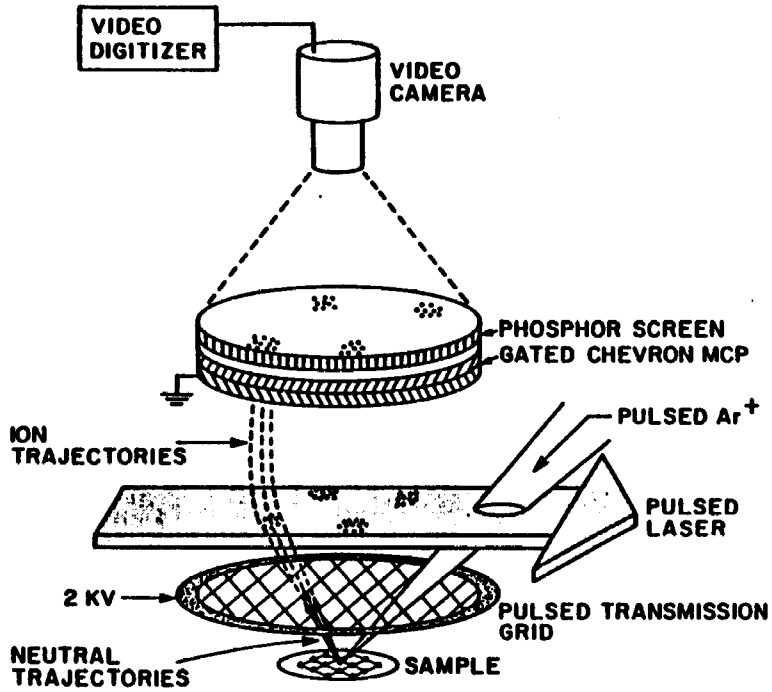

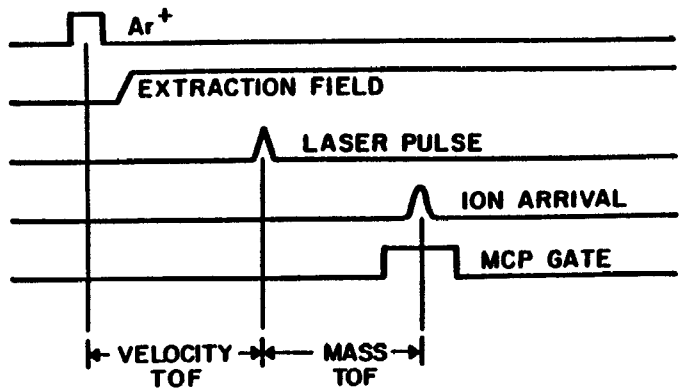

Figure 4. Schematic representation of the timing scheme for the EARN experiment. Note that the velocity of the desorbing atom is defined by the time between the ion pulse and the laser pulse. The MCP is gated to reduce unwanted signal. See text for more details.

extraction field is activated for the duration of the measure; (3) the laser pulse (~1 mJ) selectively ionizes a small volume of neutral particles at a time τ_E after the ion-pulse impact, thus defining the time of flight (TOF) of the probed particles; (4) the ionized particles are then accelerated by the ion-extraction field and arrive at the front of a microchannel plate (MCP) assembly at a time τ_m later, τ_m being governed primarily by the mass-to-charge ratio of the ionized particles. The impacting particles are detected on a phosphor screen by a CCD video camera during a time when the MCP is gated to an active state. The gate is used to discriminate against signals from scattered laser light and from ions striking the MCP at other times due to differences in either mass or ionization scheme. This image can then be accessed by a computer system for digital image data processing.

Depending on the count rate for a given experiment, 400–1000 individual images are integrated to give an average ejection pattern for one value of τ_E. During the course of a full experiment, 30–60 images, each corresponding to a different τ_E value, are recorded. The collection of τ_E images are then corrected for differences in the integration volume elements between the desired energy and angle space and the Cartesian-integrated space in which the data are recorded. After application of the appropriate transformation Jacobian, the images are sorted into an intensity map of ejection angles and kinetic energies. The geometry of the detection system allows determination of all polar angles for a given azimuthal direction with kinetic energies ranging from 0 to 50 eV. The angle resolution of about 8° is determined solely by the size of the incident ion beam, while the energy resolution of 15% for 50-eV particles and 4% for 5-eV particles is determined mainly by the incident ion beam pulse-width. This device is very important to a number of the basic ideas developed in this chapter. The data from this instrument provide a set of high-quality state-selected trajectory information which puts enormous constraints on theoretical models.

There are many other exciting new approaches to performing ion-beam/solid experiments involving liquid-metal ion sources, double-focusing mass spectrometers, fourier transform methods, triple quadrupoles, and advanced TOF analyzers, to name just a few. These schemes are beyond the scope of this work but certainly indicate that the level of sophistication of measurement is rapidly improving, boding well for the quality of data forthcoming from future experiments. In the next section, we begin to see how these measurements are intertwined with rapid theoretical advances to provide a fairly complete atomic and molecular view of the entire ion-bombardment event.

3. How To View The Process

To understand the bombardment process in detail, it is necessary to describe the series of events following the impact of the primary particle. Chronologically, the incoming particle first strikes a target atom. This atom usually attains considerable momentum directed into the bulk and collides with neighboring atoms, which produce secondary displacements. Some of these atoms have the possibility of being scattered back toward the surface with sufficient kinetic energy to escape from the sample. Many of the other atoms in the target continue moving inside the solid, slowing down only as they experience more and more collisions. The primary particle and the first target atom finally either come to rest inside the solid (implantation) or are ejected themselves. A schematic picture of some of these events, calculated using computer simulations we will describe in this section, is shown in Fig. 5. The ejection process is a complex event involving multiple atomic or molecular collisions initiated by the primary particle. Besides these atomic motions within the solid, there are concurrent electronic processes which cause species to leave the solid as secondary ions, neutrals, and electronically excited ions or neutral particles.

As shown in Figs 1 and 5 there is a multitude of events that are associated with this process including the ejection of atoms and molecules from the solid, reflection of the primary particle, implantation of the primary particle, lattice damage, and mixing within the solid, to name a few. The emphasis in this section is on the nature of the species that eject and how their properties give us insight into the characteristics of the original surface. In addition, it is our belief that models that predict detailed experimental observables are the only ones that are possible to use in a predictive mode. This emphasis thus controls which models we choose to describe most fully and which ones we only mention in passing. In addition since our goal is to ultimately describe the original surface properties, it is convenient to start with a well-defined and reproducible surface. Many of the examples described below are applicable to single-crystal targets.

The actions of interest are those in which ionic and neutral atoms and molecules eject from the surface and reach a detector. In the laboratory, it is possible to make measurements of the energy distributions, angular distributions, yields (number of particles ejected per incident particle), and cluster yields as shown in Fig. 1. The goal of the theoretical models is to predict and explain all or some subset of the experimental data. If there is good agreement between the calculated and

Figure 5. Positions of the atoms in a Rh{111} surface before and after 3-keV Ar ion bombardment. In the final positions the Ar ion appears near the center of the crystal. This trajectory was chosen at random. In some cases there is considerably more atomic motion and in some cases less.

experimental results then hopefully the model can give insight into the physical processes. Ideally, the model can also be a guiding light for new experiments. In this section we shall briefly review some of the existing approaches to predicting nuclear motion but will place perhaps undue emphasis on the model preferred by the authors. An extensive review has recently been compiled by Harrison[30] which provides excellent background information. Electronic excitations will be considered in Section 4.

There are basically two approaches to calculating the energy dissipation of the primary ion. The first utilizes a statistical model to solve the transport equations for the momentum deposition. This approach allows the yield to be expressed in terms of a simple formula which can be easily used by experimentalists. The second approach receiving considerable attention is to model the impact more explicitly using classical trajectory methods to follow the motion of the relevant particles. This method requires a large computer and generally does not provide simple formulas.

3.1. Transport Theories

There have been a number of attempts to derive analytical expressions that predict various properties of the sputtering phenomenon. The most widely used are those of Sigmund,[31–33] whose yield formulas are ubiquitous throughout the sputtering literature and of Thompson,[21] who has provided a relationship for the yield as a function of secondary particle energy. In both of these approaches, the initial assumption is that each target atom generates one secondary collision cascade in which energy is shared by a series of collisions. Next, it is assumed that the collisions themselves occur only between two atoms at a time. This assumption is referred to as the binary collision approximation (BCA). These approximations have a number of important consequences. First, any electronic energy loss processes are ignored. This is probably a realistic approximation for metals bombarded at less than 50 keV by heavy particles, although for insulators such as alkali halides,[34] coulombic interactions may contribute to sputtering. For elastic collisions, the assumption that each collision sequence can be treated separately restricts application of the theory to the region of so-called linear collision cascades.[31,35] As shown in Fig. 6a, this condition applies only when a small fraction of all atoms within a given volume are in motion. When more than one cascade is initiated by the primary ion, as shown in Fig. 6b, or when a large fraction of the atoms near the impact point are moving, the approach begins to breakdown. This region is often referred

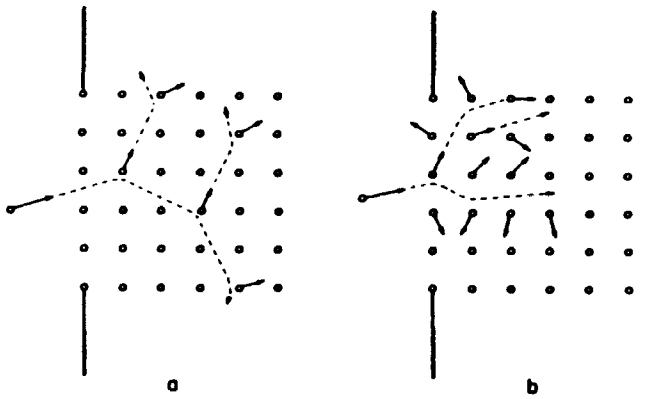

Figure 6. (a) Linear collision cascade. The structure is preserved and a small fraction of the atoms is in motion. (b) Dense cascade (spike). The structure is destroyed locally. All atoms within the spike volume are in motion. (From Ref. 35.)

to as a dense cascade or a spike. One final consequence is that the BCA should only apply to collisions which exceed several hundred eV. For example, in Fig. 6a, the sizes of the atoms are drawn such that it is impossible for more than two atoms to interact simultaneously. If the atomic radii had been drawn such that adjacent atoms nearly touched, as in the case for collision energies below ~10 eV, then binary collisions are indeed improbable. It is disturbing that most of the collisions that lead to the ejection of atoms in the solid are those whose energies are below 10 eV as illustrated by the secondary particle energy distributions shown in Fig. 7a.

In the Sigmund theory, the solid is approximated by an amorphous array of atoms that interact with differential cross sections developed for calculations aimed toward predicting the range of energetic atoms in solids.[31] The nuclear stopping cross section $S_n(E)$, where E is the energy of the ejected particle, can be evaluated from these quantities. The flow of energy through the cascade is then determined using the Boltzmann transport equation. The sputtering yield is evaluated from the flux of particles that crosses an imaginary plane at a point in the solid where the target atom is given its initial energy. To include the effect of the surface, it is assumed that the atom must surmount a potential barrier, U, acting on the perpendicular component of the velocity. This potential will act to keep slow-moving particles from escaping the barrier and will deflect the faster-moving ejecting particles away from the surface normal. This approximation is described as the planar surface binding model.[31,32] If the collision cascade is restricted to the linear regime by utilizing

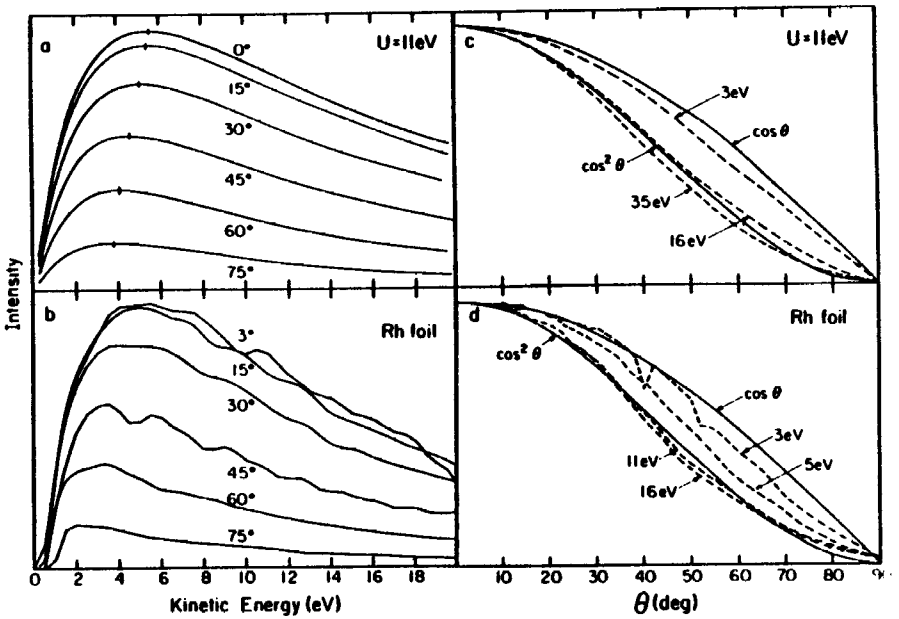

Figure 7. Energy distributions of Rh atoms ejected from a Rh foil for various polar angles, θ, as measured from the surface normal. (a) Calculated from Eq. (5). The cross marks denote the positions of the maxima. (b) Experimental results from Ref. 46. The primary ion beam was Ar^+ with a kinetic energy of 5 keV aimed perpendicular to the surface. (c) Calculated from Eq. (5). (From Ref. 47.) (d) Polar distributions of Rh atoms ejected from a Rh foil for various energies. All curves are peaked normalized at $\theta = 0°$. Experimental results from Ref. 46. The energy ranges are ±1 eV.

bombardment energies below a few keV and by utilizing light ion and target masses, the equation for the sputtering yield becomes

$$S = \frac{CS_n(E)}{U} \tag{1}$$

where C is a constant for a given primary ion energy and target material. The simplicity of this result—that the sputtering yield is proportional to the nuclear stopping power of the solid and inversely proportional to the surface binding energy—accounts, in part, for the popularity of the Sigmund theory. In fact, it has been rather successfully applied in a number of instances.[36] The direct correlation between the stopping power and the yield is particularly striking as is illustrated in Fig. 8 for Ar^+ on Cu.[32,37] The relationship between yield and surface binding

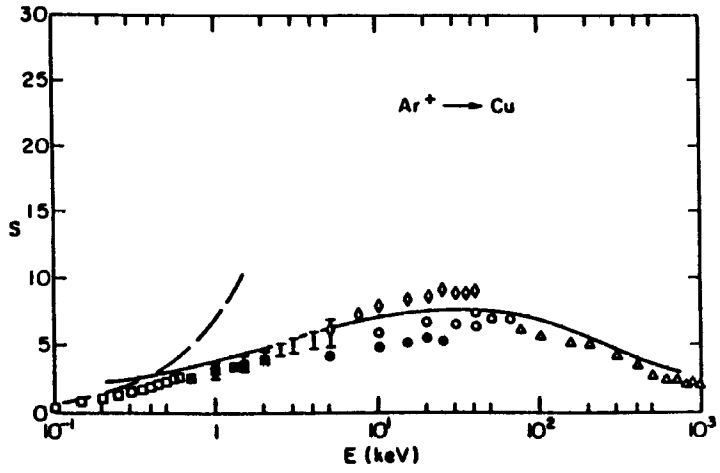

Figure 8. Sputtering yield as a function of the primary ion energy. The lines are calculated yields from $S_n(E)$ while the points are experiment curves taken from various groups. From Refs. 31 and 32.

energy (or sublimation energy of the solid) has been used to explain differential sputtering[38] and variations in sputtering yield across the periodic table.[31,39] The theory has also been applied to situations where it should not work, probably since for many years it was the only real theoretical approach available to experimentalists.

A similar theoretical model has been developed by Thompson to explain the energy distribution of ejected atoms.[21] His model grows from an expression for the flux of atoms inside the solid crossing any internal surface plane. For an ejecting particle of kinetic energy E, this flux is given as

$$\phi(E)\,dE\,d\Omega = [C'E\cos\theta/(E+U)^{n+1}](2\pi\sin\theta)\,d\theta\,dE \qquad (2)$$

where $\phi(E)$ is the flux density energy distribution with units of number per unit area per unit time per unit energy. The solid angle $d\Omega = \sin\theta\,d\theta\,d\phi = 2\pi\sin\theta\,d\theta$; $d\phi$ is the azimuthal angle about which the flux is assumed to be isotropic. According to Thompson,[21] $n = 2$ and C' is a constant for a given primary ion, energy, and target material. The appearance of U in Eq. (2) is a consequence of the incorporation of the planar surface binding model in the theoretical development.

The predictions of Eq. (2) are that (1) the peak in the energy distribution occurs at U/n, (2) the peak position is *independent* of θ, and (3) the polar distribution is *independent* of E. Over the years this relationship has fit the experimental data quite well. This agreement is

remarkable since the underlying assumption in the Thompson model is that the atoms only undergo binary collisions. As stated above for particles that eject with energies $<2U$, the desorption process undoubtedly occurs via multiple collisions. In fact, an attractive interaction, e.g., surface binding energy, is inconsistent with binary collisions as attractive interactions are long ranged and binary collisions are only valid for close encounters. Generally, in any one experiment, either the energy distribution at one polar angle is measured or the polar angle distribution for a large energy bandwidth is measured. In the first case, the constants U and sometimes n of Eq. (2) are fitted to the data. In the case of the polar distributions, it has been observed[40–42] that the polar distribution is often closer to $\cos^2\theta$ than $\cos\theta$.

Recently energy and angle resolved (EARN) distributions of neutral atoms ejected from In and Rh foils have been measured.[29,43–47] In these experiments polar distributions at several energies and energy distributions at different polar angles were obtained simultaneously.[46] In this case the primary particle was Ar^+ with 5 keV of energy directed normal to the surface. There are three interesting deviations from the predictions of the Thompson model. (1) The peak position in the energy distribution shifts to a lower value as the polar angle from normal increases (Fig. 7a). Each of the individual curves, however, if U and n are used as parameters, can be well represented by Eq. (2), as seen in Fig. 7b. (2) The polar distribution becomes narrower at higher kinetic energies (Fig. 7c), so that at high energies the distribution is approximately $\cos^2\theta$. (3) The value of U needed to fit the data is larger than the heat of sublimation.

These discrepancies have been accounted for by analyzing the various assumptions of the Thompson model.[47,48] A reasonable agreement with the experimental distributions can be made by assuming that the velocity distribution in the solid is *not isotropic*. This assumption is completely reasonable. In a Thompson model, conceptually an infinite bulk solid is considered and then an imaginary plane is used to define the surface. In the real solid, the surface undoubtedly influences the distribution of velocities.

If one assumes that the distribution of particle energies and directions inside the solid is given by

$$f_1(E_i\theta_i) = \cos^m\theta_i/E_i^2 \qquad (3)$$

where the value of n of Eq. (2) is taken to be two. In order to get the distribution outside the solid, application of the same transformations as

Thompson results in the final distribution of the yield as

$$Y(E, \theta) \propto \frac{E \cos\theta}{(E + U)^3} \frac{[(E \cos^2\theta + U)^m]^{1/2}}{[(E + U)^m]^{1/2}} \quad (4)$$

In Thompson's case the value of m is 0, and Eq. (4) reduces to Eq. (2). The choice of $m = 2$ fits the experimental data reasonably well and simplifies the mathematics. In this case Eq. (4) becomes

$$Y(E, \theta) \propto \frac{E \cos\theta}{(E + U)^4}(E \cos^2\theta + U) \quad (5)$$

The energy and polar distributions as predicted by Eq. (5) for Rh are shown in Figs. 7a and 7c, respectively. A value of $U = 11$ eV resulted in a reasonable fit to the experimental data. The agreement between the calculated and experimental curves is remarkable. The energy peak position shifts to lower energy as the polar angle increases. In the case of the polar distributions, at very low energies the distribution is nearly $\cos\theta$. As the energy of the particles increases, the polar distribution becomes narrower (Fig. 7c). In the limit of extremely high energies the predicted distribution becomes $\cos^3\theta$. If all energies are averaged the polar distribution is

$$Y(\theta) \propto \cos\theta(2\cos^2\theta + 1)/3 \quad (6)$$

where $Y(\theta = 0°) = 1$. The deviation of Eq. (6) from $\cos^2\theta$ is less than 0.03 for all values of θ.

Computer simulations as described in Section 3.2 for the keV particle bombardment of an amorphous indium sample were performed by Lo *et al.*[49] in order to verify the assumption of anisotropic velocity distributions. The angular velocity distributions were determined for the surface layer as a function of elapsed time after the initiation of the collision cascade. Their results as seen in Fig. 9 indicate that the presence of the free surface (neglected in the Thompson model) cause significant anisotropy in the outermost surface region. The distribution quickly became isotropic in the subsurface region.[49] Of note is that the simulations reproduced the shift in peak position in the energy distribution with polar angle and the narrowing of the polar distribution with increasing desorbed particle energy.

The final issue is the choice of a value for U. As a matter of convenience (and lacking a better choice), the value of the surface binding energy is often equated to the heat of sublimation of the solid, ΔH_s. The choice of ΔH_s for the energy parameter in the prediction of the sputtering yield gives reasonable agreement with the measured

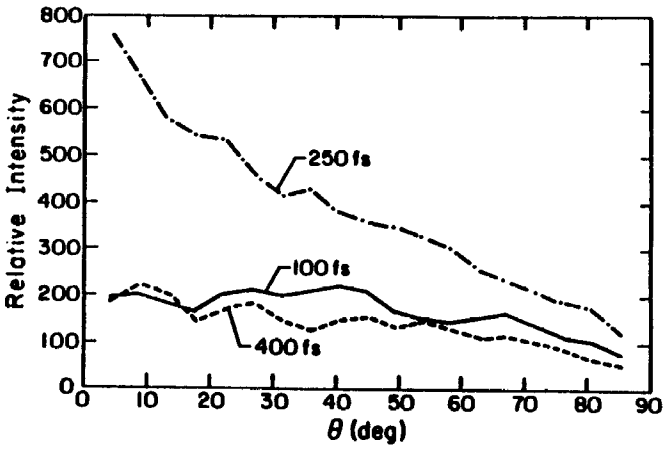

Figure 9. The development of the angular distributions in the first surface layer. The majority of particles eject between 100 and 250 fs (2 fs = 10^{-15} s). (From Ref. 49.)

quantities.[31] However, Husinsky[50] has pointed out that the values of U fitted to experimental energy distributions are sometimes larger than the ΔH_s value of the material.

One possibility is that the energy cost to remove an atom from a solid is actually greater than the heat of sublimation.[51–53] The roots of this idea lie in two virtually unnoticed papers by Jackson.[54,55] He simulated the ejection of a surface atom by giving it an initial kinetic energy. The final kinetic energy (for a pairwise additive potential approximation) corresponds to an energy loss greater by 30%–40% than the bulk ΔH_s. One would think that this implies that by ripping the entire solid apart it would take more energy than it had in the first place.

This dilemma is best described by examining a diatomic molecule that has a bond strength of D_e. Under the rules used for solids, the binding energy of each atom is $D_e/2$. If, however, one atom is clamped fixed and one asks how much kinetic energy must be supplied to the other atom so that the bond can be ruptured, then the answer is D_e—twice the "binding energy". Note that it now costs nothing to remove the second atom. An analogous situation occurs in the solid. In one extreme in the ion bombardment procsss, all atoms but one are fixed. The energy cost for this atom to escape the solid is greater than ΔH_s, in line with recent experimental results. It is not clear either theoretically or experimentally precisely what is the value of the energy cost to remove an atom from a surface. It is also not clear which factors influence the

magnitude of this energy cost. Should it be the same for amorphous Rh, Rh{111}, Rh{110}, and Rh{100}, for example?

Another problem with the picture as painted by the transport theory has recently been pointed out by Shapiro.[56] From molecular dynamics simulations he found that a significant portion of ejected atoms actually lost more kinetic energy in their escaping trajectory than was required to overcome the surface binding energy. This conclusion is in conflict with the assumptions made in the transport theory.[52,57–59] This energy loss phenomenon has recently been observed by Reimann *et al.*[60] in a series of EARN experiments on clean Rh{111} and oxygen covered Rh{111}. The energy distribution of the neutral Rh atoms ejected from the oxygen covered substrate was found to peak at a *lower* energy than the distribution from the clean surface. Computer simulations (Section 3.2) on the same systems confirm this trend. Although the relative binding energies of the Rh atoms in the real system are not known, it is known from the simulations that the Rh{111} surface atoms with an oxygen overlayer have a *larger* binding energy than those of the clean surface. This trend is in contradiction to the transport theories which predict that the peak in the energy distribution should be proportional to the binding energy. Obviously there are other factors such as collisions that influence the peak position.

In addition to the problems with describing the details of the energy and angular distributions, the transport theories are not equipped to describe the ejection of clusters. For example, the linear cascade approximation is inconsistent with the ejection of clusters such as Ni_2, which, as described below, forms via a recombination mechanism involving two interlinking cascades. There is no way to incorporate into the transport models explicit molecules (e.g., benzene) and examine the relative ejection yields of the fragment, C_2H_2, and the molecular, C_6H_6, species. Finally, the transport theories do not include single-crystal structures, an important aspect of the studies which is of interest to many surface scientists.

Our intent here is not to denigrate the transport theory, as it has been a reasonably good qualitative guide for experimentalists over the years. However, we wish to point out that if one wants a detailed qualitative and quantitative picture of the particle bombardment process one must look beyond transport theory. The approach that we feel has had considerable success is described in the next section.

3.2. Molecular Dynamics Calculations

Many of the difficulties associated with transport theory can be overcome by utilizing a molecular dynamics calculation on a large ensemble of atoms to compute actual nuclear positions as they change in time subsequent to the primary ion event. Classical dynamics calculations have, of course, been very successful in explaining trajectories in atom–diatom scattering,[61] properties of liquids,[62] gas–surface scattering,[63] and even the solvation of large molecules like dipeptides.[64] For describing the desorption process this approach has the distinct advantage of utilizing many fewer approximations than required for the statistical theories. On the other hand, no simple equation falls out of the calculations, although important concepts may emerge from the resulting numbers. The calculations often prove very useful in testing the validity of possible analytical theories. In general, these calculations require considerable computer time. With the recent surge in computer efficiency and decrease in costs, it would appear that this is becoming less of a difficulty.

The computation of the classical trajectories using the molecular dynamics procedure rests on Hamilton's equations of motion. For a particle i of mass m_i, the equations of motion are

$$m_i d\mathbf{v}_i/dt = \mathbf{F}_i = -\nabla_i V(r_1, r_2, \ldots, r_N) \tag{7}$$

and

$$d\mathbf{r}_i/dt = \mathbf{v}_i \tag{8}$$

where $\mathbf{r}_i$, $\mathbf{v}_i$, and $\mathbf{F}_i$ are the position, velocity, and force of the ith particle. The interaction potential V depends on the positions of all the N particles. It is the quality of V that determines the reliability of the results of the molecular dynamics simulations. Since V is such an integral part of the calculation an entire section, 3.3, is dedicated to a discussion of the various types of available interaction potentials. For the moment, we will assume that there is a suitable interaction potential and examine the results of the classical dynamics calculations.

The presence of N particles results in $6N$ coupled first-order differential equations. There is a plethora of numerical schemes for solving these equations.[65] The general idea is to take sufficiently small time increments Δt such that the force is approximately constant. The positions and velocities of all the particles are then generated through time. For the ion bombardment process the timestep is typically 0.1 fs (1 fs = 1×10^{-15} s) at the beginning of the bombardment event when the primary particle is moving rapidly and increases to about 3–10 fs at the end of the event. Most of the ejection events occur in less than 500 fs, which means that there are 50–1000 time steps.

To integrate Hamilton's equations of motion, the initial positions and velocities of all the particles must be specified. In most simulations to date the substrate atoms are placed at their equilibrium positions with

zero velocity. These values could be chosen from a Maxwell–Boltzmann distribution at the appropriate temperature but there is no overwhelming evidence that ejection events are strongly temperature dependent. One can thus choose to mimic a Rh{111} crystal,[66,67] an amorphous In sample,[49] or an overlayer of benzene on Ni{100}.[68] That leaves the primary particle's initial conditions to be chosen. In general the experimental conditions are such that the initial kinetic energy, E_{in}, polar angle, θ_{in}, and azimuthal angle, φ_{in}, are prescribed. These values then determine the initial velocity of the primary particle as

$$v = (2E_{in}/m)^{1/2} = (v_x^2 + v_y^2 + v_z^2)^{1/2} \tag{9a}$$

where

$$v_x = v \sin\theta_{in} \cos\varphi_{in} \tag{9b}$$

$$v_y = v \sin\theta_{in} \sin\varphi_{in} \tag{9c}$$

$$v_z = -v \cos\theta_{in} \tag{9d}$$

and m is the mass of the particle. To ensure that the incident particle does not interact with the crystallite at $t = 0$, the z component of the position should be infinite. Most interaction potentials have a finite range (2–6 Å), however, so that infinity is not that large. The lateral positions (x, y) must be chosen to mimic the experimental conditions. Since in the laboratory reference it is not possible to choose an impact coordinate, the data are actually averages over many primary particle impacts on the surface. In the calculations one must also perform numerous simulations in which different sets of initial (x, y) aiming points are chosen. This leads to "statistical noise" in the calculated observables. The yield is calculated from the average number of particles that eject per incident particle. It is usually possible to obtain a statistically reliable value with 50–100 different impact positions. For energy and angle resolved distributions, several thousand impacts may be required to obtain a respectable signal-to-noise ratio.

The remaining initial condition to choose is the number of atoms, N, in the sample. Ideally, N should be as large as possible. Depending on the nature of the interaction potential, however, the required computer time scales somewhere between N^1 and N^3. Thus, a practical number of atoms must be chosen by performing test calculations on samples of various sizes and making a determination of what is sufficiently large to accurately reproduce the observables. The crystal size will depend on exposed crystal face, overlayer unit cell size, and primary particle kinetic energy and angle. Typically for calculations below 1 keV of energy we have used crystals of 1000–2000 atoms. Normally, a flat and wide-shaped

crystal rather than a cubic one yields more accurate results with the same number of atoms. Typical execution times on an IBM 3090 for one primary particle impact are 30–900 s for a 1450-atom Si{110} target and 100–1000 s for a 700-atom Rh{111} target. There is a large variation in time since various aiming points on the surface may result in rather simple trajectories or extremely complex ones.

A unique feature of the sputtering simulations, in contrast to other simulations of solids and liquids, is the choice of boundary conditions on the sides and bottom of the crystallite. There can easily be one or two very energetic (20–500 eV) particles that reach the edge of the crystallite. These particles in a real solid penetrate further into the bulk, damaging the sample along their path. By enlarging the crystallite in the simulations it can be verified that these energetic particles do not substantially contribute to the ejection of atoms and molecules into the gas phase. Thus, these atoms are truncated from the simulation once they leave the side or bottom edge. Periodic boundary condition should *not* be employed as it is nonphysical to have the energy enter the other side of the crystal. Likewise the generalized Langevin[69,70] prescription or a rigid layer would cause reflection of the energy back into the crystal, again a nonphysical phenomenon.

Finally, the atomic motion subsequent to the primary particle impact is computed for enough time such that no particles have sufficient total energy to escape the solid. For a metal such as Rh, we have found that after the most energetic particle left in the solid (not counting those ejected or those that left via the sides of the crystal) has less than 0.2 eV of energy (kinetic plus potential energy) that integration for longer times does not produce any more ejected particles.

After the integration has been terminated, a number of quantities can be calculated from the final positions and velocities of the atoms. These range from experimentally observable quantities such as the energy distribution to unobservable features such as ejection mechanisms. Below we give examples of the various output data that can be obtained from computer simulations of the sputtering process.

3.2.1. Yields

The average number of particles ejected per incident ion is one of the easiest properties to determine numerically yet one of the hardest to calculate reliably. The calculated value depends on the crystal face of the sample, the primary particle–substrate interaction potential, the substrate–substrate interaction potential, etc. In addition, reliable experimental values are almost impossible to obtain under the same

conditions as the calculations are performed. Virtually all the simulations are performed in the low-dose mode, i.e., each primary particle impacts a fresh sample. Most experimental measurements of yields are carried out under high-dose conditions where there is a sufficient dose of primary particles such that portions of the sample are rebombarded. This means that the crystal structure has been altered during the course of the measurement and that primary particles have been implanted. Shown in Fig. 10 are yields calculated by Stansfield *et al.*[71] for the sputtering of Si{100} as a function of Ar^+ kinetic energy. They have used different Ar–Si and Si–Si repulsive interaction potentials along with the attractive many-body potential for silicon as given by Stillinger and Weber.[72] They have compared their yields to experimental values obtained using a weight-loss procedure.[73] The calculated yields depend strongly on the type of potential function. Moreover, the yields for unreconstructed

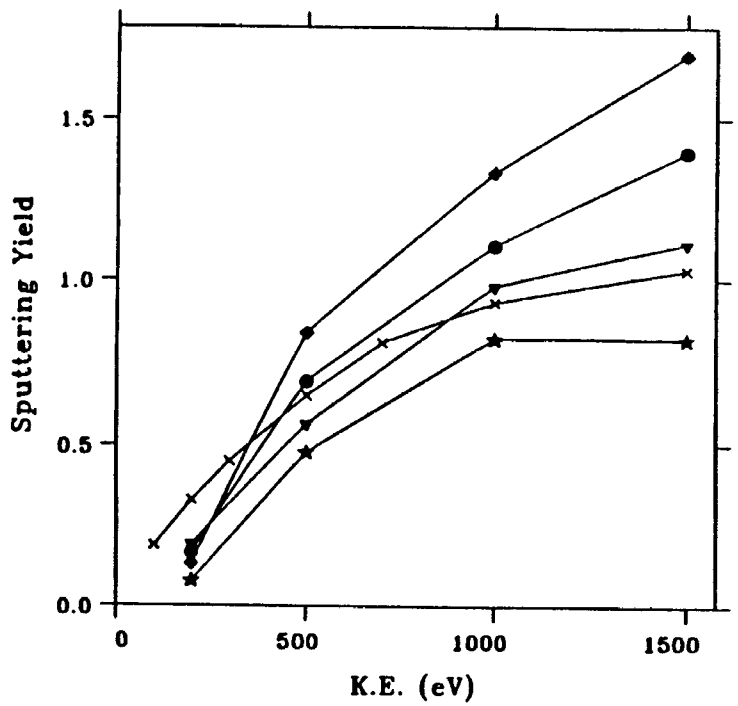

Figure 10. Experimental and calculated Ar^+ +Si{100} sputtering yields. ×, Experiment[73] (steady-state yield); •, the SDCI and SCF potentials (unreconstructed surface); ◆, the Smith modified Wedepohl potentials (unreconstructed surface); ▼, the Biersack-Ziegler universal potentials (unreconstructed surface); ★, the SDCI and SCF potentials (reconstructed surface).

Si{100} and the dimer reconstructed face vary even with the same potential. As stated in Section 1 an average quantity like yield does not help to discriminate among the various assumptions inherent in any given model.

3.2.2. *Energy and Angular Distributions*

The final velocities yield sufficient information to calculate the kinetic energy (E) of each ejected particle as

$$E = \tfrac{1}{2}mv^2 \tag{10}$$

where

$$v^2 = (v_x^2 + v_y^2 + v_z^2) \tag{11}$$

with angles

$$\theta = \arccos(v_z/v) \tag{12}$$

and

$$\varphi = \arctan(v_y/v_x) \tag{13}$$

To obtain either an energy or angle distribution, the particles from a multitude of different primary particle hits on the surface are collected. The energy and angle distributions are mutually interdependent. Shown in Fig. 11 are the polar angle distributions from Rh{111} from both the EARN experiment described in Section 2 and from calculations using a pairwise additive potential and an embedded atom method (EAM) potential (Section 3.3). The azimuthal angles for the Rh{111} crystal face are defined in Fig. 12. The peak intensity along the azimuthal direction $\varphi = -30°$ is greater than along $\varphi = +30°$ or 0° for all secondary-particle ranges. As the Rh atom energy increases, the $\varphi = +30°$ intensity increases relative to the $\varphi = 0°$ intensity. Moreover, both theory and experiment find that the intensity at $\theta = 0°$ increases relative to the peak intensity at $\theta = 25$–$40°$ as the energy increases . Of note is that the polar distributions are quite complex and as stated in Section 1 are an aid in discriminating among various theories and models. The relative agreement between the data from two calculations and the experiment will be discussed in Section 3.3. The reasons behind this structure will be unraveled in Section 5.

In a similar fashion it is possible to calculate the secondary particle kinetic energy distributions. As shown in Fig. 13, these distributions for Rh{111} agree well with those determined from EARN experiments.[67] Both the angle-integrated distributions and the distribution at $\theta = 40°$

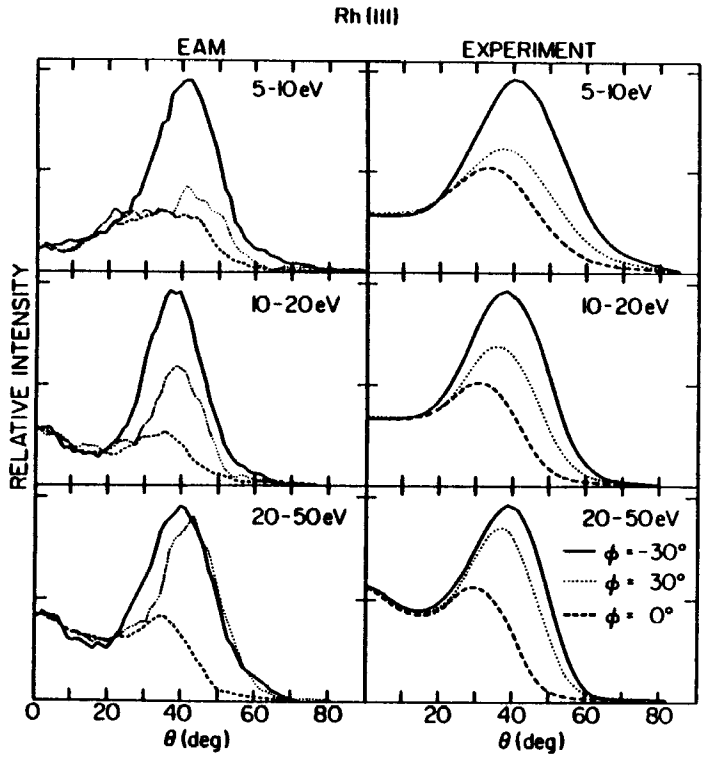

Figure 11. Polar angle distributions for various azimuthal angles for fixed secondary kinetic energy of the Rh atoms. In each frame the data are normalized to the $\phi = -30°$ peak intensity. The calculated data using the EAM potential are reported with a full width at half maximum (FWHM) resolution of 15° in the polar angle. A constant solid angle is used in the histogramming procedure. The experimental resolution is also approximately 15°. The surface normal corresponds to $\theta = 0°$.

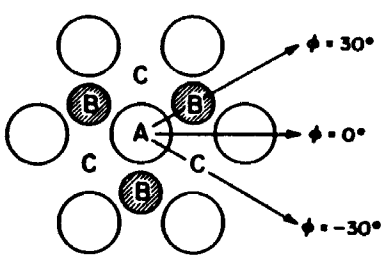

Figure 12. The azimuthal directions are defined above. A polar angle of 0° is normal to the surface and 90° is parallel. Open circles designate first layer atoms and shaded circles second-layer atoms. The letters A, B, and C designate possible adsorption sites for oxygen atoms.

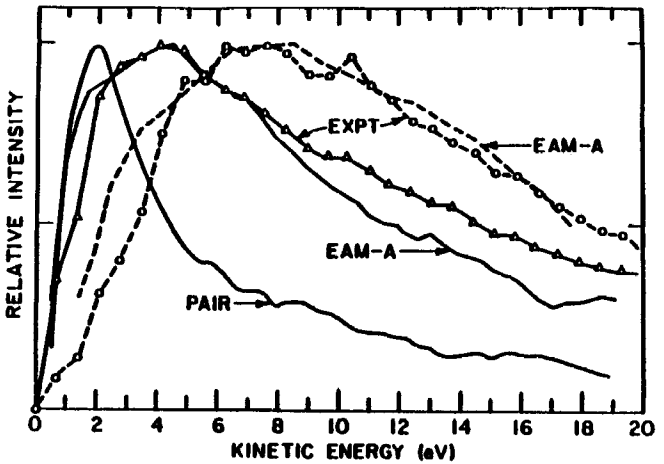

Figure 13. Experimental and calculated kinetic energy distributions. In all cases the curves are peak normalized. The two experimental curves are the angle-integrated distribution and one at $\phi = -30°$ and $\theta = 40 \pm 3°$. The EAM-A curves are the angle-integrated distribution and one at $\phi = -30°$ and $\theta = 38 \pm 7.5°$. Only the angle-integrated distribution is shown for the pair-potential calculation. The angle-integrated distributions are shown as solid lines and the ones at $\theta \sim 40°$ as dashed lines. (From Ref. 67.)

and $\varphi = -30°$ have been determined. It is quite clear that in a fashion similar to the polycrystalline surfaces (shown in Fig. 7), the energy distribution depends on the take-off angle of the secondary particles. As we shall see below the molecular dynamics calculations using the EAM potential do an excellent job of reproducing the experimental distributions.

3.2.3. *Clusters*

One of the intriguing aspects of the particle bombardment process is the appearance in the mass spectra of molecules or clusters. These species can be of the type Ni_n, where $n \geq 2$ from a Ni substrate or C_6H_6 which is observed from a bombarded film of benzene on Ni. Do these clusters actually exist on the surface? Initially one may think that the bombardment process is too catastrophic to preserve the fragile information encoded in chemical bonds. On the other hand, if everything is dissociated into atoms, how does the C_6H_6 molecule get back to its original composition? If the clusters do arise from contiguous surface atoms, can their presence provide key information regarding the local atomic structure of surfaces of alloys and supported metal catalysts?

A powerful aspect of classical mechanics is that the microscopic motions of the atoms arise *from* the calculations. That is, one does not have to *assume* that one particular collision sequence is more important than another. This allows formulation of the mechanisms of cluster formation directly from the simulations. To check for the appearance of the clusters, the total internal energy is computed. This energy consists of the relative kinetic energy plus potential energy of an aggregate of m atoms above the surface. If the total internal energy is greater than zero, then the aggregate is not bound. If it is less than zero, then the cluster is at least temporarily stable. If m is greater than 2, then the cluster may decompose on the way to the detector as has been observed in alkali–halide clusters.[74] The center-of-mass velocity of the cluster can be used to predict energy and angular distributions.

Computer simulations have clearly demonstrated that molecules such as CO and C_6H_6 can survive the ion bombardment process without fragmentation. A graphic representation of a computer simulation of molecular ejection is illustrated in Fig. 14. There are two principal reasons for this result. First, the roughly equivalent effective sizes of metal substrate atoms and adsorbed hydrocarbon molecules facilitates the ejection of molecules without significant fragmentation. For example, the hard-sphere diameter for a single Rh atom in a crystal is 2.7 Å and the van der Waals diameter for a four-atom CH_3 group is 4 Å.[75] This means that a moving Rh atom encounters this group as a single species and can eject it without dissociating the CH bonds. The second reason for the intact ejection of these molecules is that they contain many vibrational degrees of freedom that can absorb kinetic energy that would otherwise lead to fragmentation. This contribution becomes more important for intact ejection as the size of the molecule increases.

The fact that molecules can survive the ion impact is encouraging for correlating the composition of the desorbed species with surface composition. Unfortunately, sputtered atoms and molecules have also been observed in the simulations to recombine into bound molecules in the near-surface region. This mechanism can lead to the detection of stable molecules that were not present on the surface, and can complicate the interpretation of results. For example, the observation of NiCO and Ni_2CO clusters from the sputtering of a CO covered Ni surface could be interpreted as indicating that chemisorbed CO molecules are bound both to single Ni atoms (atop binding sites) as well as pairs of Ni atoms (bridge-binding sites).[76] This could be an erroneous interpretation because recombination processes can also lead to the formation of multiply bonded CO molecules.[77] The recombination mechanism, however, does not completely destroy the ability to evaluate the significance

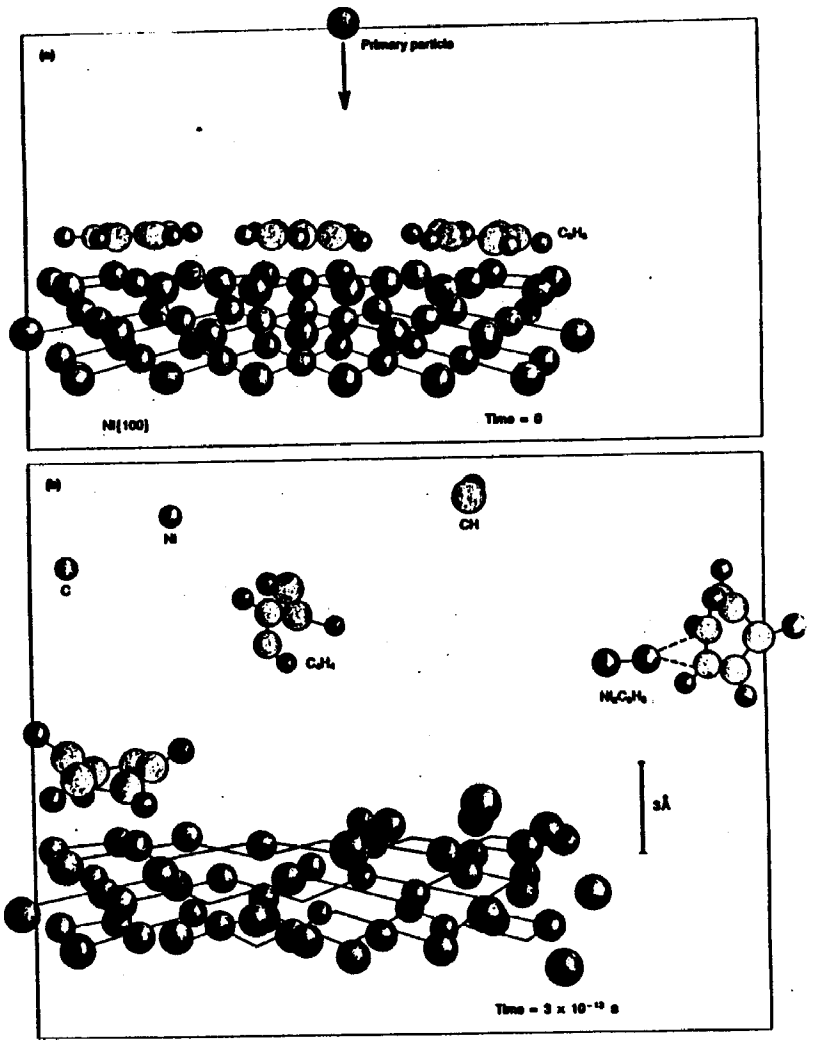

Figure 14. Ion bombardment event on a benzene covered Ni{100} surface. (a) Before the primary particle has stuck the surface. (b) After 3×10^{-13} s. The benzene is initially bonded parallel to the surface. Frame (b) shows several possible outcomes of the collisional event. The center benzene molecule was hit sufficiently hard that it fragmented with parts of the molecule ejecting and one of the H atoms implanting into the solid. In this particular hit on the surface, the primary particle also implanted. One benzene molecule (on the left) remained bound to the surface although it did get distorted. Another benzene molecule ejected, in this case in close proximity to two Ni atoms, thus there is the possibility of a $Ni_2C_6H_6$ formation.

of the composition of desorbed particles because it only occurs between species that are originally in close proximity on the surface. The general picture from simulations is that the identity of desorbed material can be used to assign surface species, but that care must be exercised in making such assignments.

An example of how two surface atoms that are not contiguous might recombine in the near-surface region to form a dimer or diatomic molecule is shown in Fig. 15. In this case[78] both experiment and calculation found that Ni_2 dimers are ejected from a Ni{001} surface preferentially along the $\varphi = 0°$ azimuth or ⟨100⟩ direction. An analysis

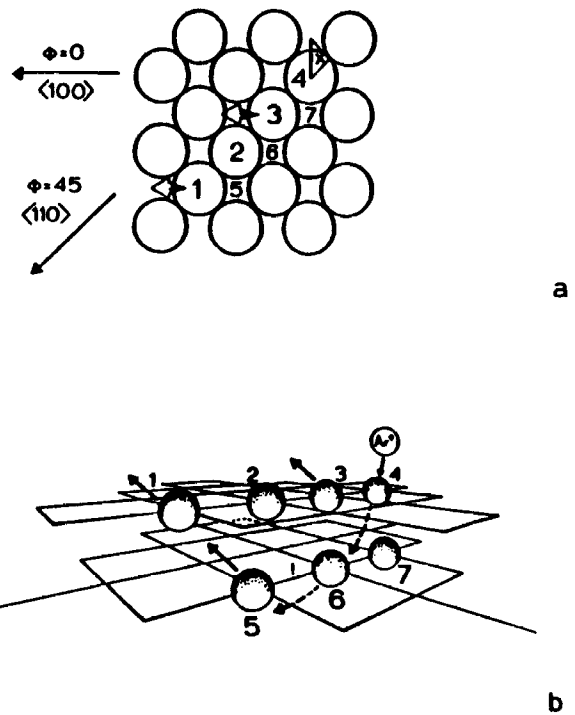

Figure 15. Mechanism of formation of the Ni_2 dimer, which preferentially ejects in the ⟨100⟩ directions, contributing the majority of intensity to the peak in the angular distribution. (a) Ni{001} showing the surface arrangements of atoms. The numbers are labels while the × denotes the Ar^+ ion impact point for the mechanism shown in (b). Atoms 1 and 3 eject as indicated by the arrows forming a dimer, which is preferentially moving in a ⟨100⟩ direction. (b) Three-dimensional representation of a Ni_2 dimer formation process. The thin grid lines are drawn between the nearest-neighbor Ni atoms in a given layer. For graphical clarity, only the atoms directly involved in the mechanism are shown.

of the dimers that eject in the simulation show that one mechanism of formation is dominated in the peak of the angular distribution of the dimers. This mechanism is shown schematically in Fig. 15b. The Ar^+ ion strikes the target surface atom, No. 4, which moves under No. 3, ejecting it. Atom No. 3 is channeled through the fourfold hole in the surface and thus escapes in the ⟨100⟩ direction. Concurrently, atom No. 4 is moving toward the second layer pushing atoms No. 6 and No. 7 down. In the same manner in which atom No. 4 ejected atom No. 3, No. 6 pushes No. 5 up toward the first layer. Atom No. 1 is subsequently ejected by atom No. 5. Again, No. 1 is channeled through the fourfold hole in the ⟨100⟩ direction. These two atoms, No. 1 and No. 3, are moving parallel to each other, are in close proximity, and are thus susceptible to dimer formation. In this case, the relative kinetic energy is less than 1 eV, the center-of-mass kinetic energy is 20 eV and the potential energy −1 eV. When ejected as monomers, these two atoms (No. 1 and No. 3) exhibit the same azimuthal anisotropy; however, these are a relatively minor part (~10%) of the corresponding energy selected monomer peak.[78]

There is an important ramification of the prediction that the dimers that give rise to the maxima in the angular distribution are formed primarily from constituent atoms whose original relative location on the surface is known. If this result were extrapolated to alloy surfaces such as CuNi, the relative placement of the alloy components on the surface would be determined. Recent calculations indicate that other originating sites of ejected dimers can be preferentially enhanced by varying the angle of incidence of the primary Ar^+ ion.[79] It is hoped that information on the surface structure of alloys can be obtained from an analysis of the angular distributions of the multimers. Preliminary experiments and calculations of other clusters which form via a recombination mechanism also display angular anisotropies. These include such species as Ni_3, NiO, and NiCO. The ejection direction tends to be toward the surface normal and thus is difficult to measure with the existing experimental setup.

The interpretation of the meaning of the cluster composition is obviously a complex issue. The molecular dynamics calculations provide insight into the basic formation mechanisms. These mechanisms have forced investigators to devise special experiments to test for the presence of recombination. Examples of these tests will be presented in Section 5. In the future, it will be valuable to see if more quantitative predictions will be possible. Perhaps by measuring the vibration and/or rotational excitation of neutral molecules as a function of kinetic energy and take-off angle, it will be possible to formulate more specific models. In

the meantime these calculations provide at least a critical guide to the experimentalist.

3.2.4. *Damage to the Substrate*

Concurrent with the ejection of particles into the vacuum there is considerable action in the solid which leads to damage to the remaining substrate. This damage ultimately limits the resolution of depth-profiling analyses and is a limiting factor in the applications of ion-beam processing of microelectronic materials. These processes have typically been modeled by BCA codes such as TRIM[80] since the crystal sizes

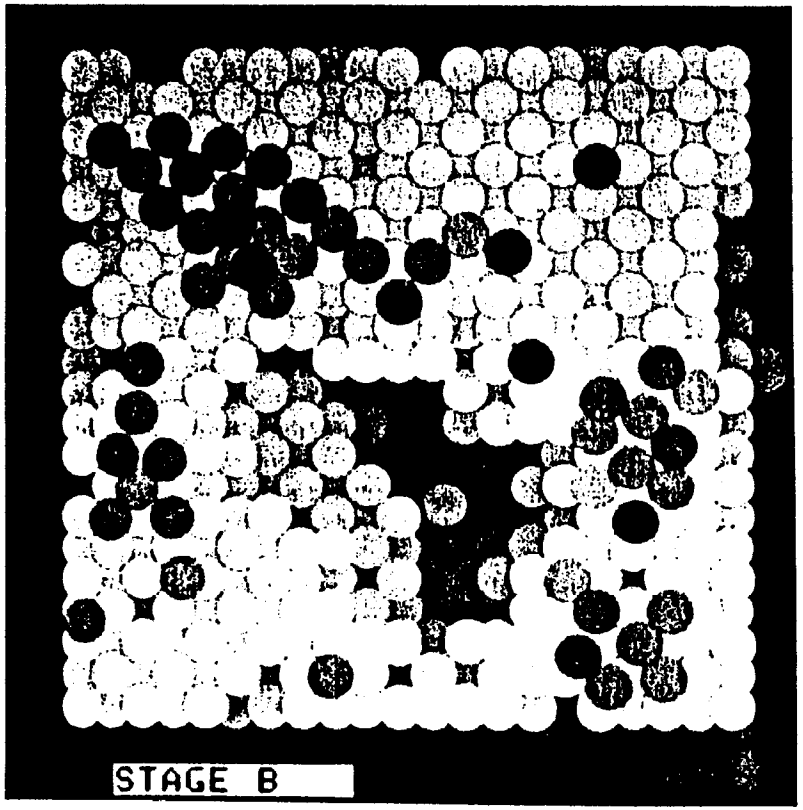

Figure 16. Computer simulations of radiation damage. A Cu{100} crystal was bombarded by a single Ar^+ ion with 500 eV of kinetic energy. The dynamics of the energy relaxation are then followed for several picoseconds as described in the original article. The size of this crystal is approximately 35 $Å^2$. This picture was provided by D. E. Harrison, Jr.

needed to describe the damage region are too large for molecular dynamics simulations. Webb and Harrison,[81] however, did model the formation of pits that form during bombardment of a Cu{100} surface. The surface rearrangement which occurs after a single bombardment event is shown in Fig. 16. The surface is about 35 Å wide. The open circles represent surface atoms that have not changed their lattice sites. The atoms in the layers below the surface are shown in increasing shades of gray. Note that a few atoms have been deposited on top of the surface during the collision cascade. Recently, it has been possible to observe these pits directly on PbS with a scanning tunneling microscope (STM).[82] The STM image is shown in Fig. 17. The agreement between the qualitative features of the surface damage is remarkable. Note that the dimensions of the surfaces are the same for both examples. In both cases a pit is formed with a buildup of atoms around the edges of the pit. To

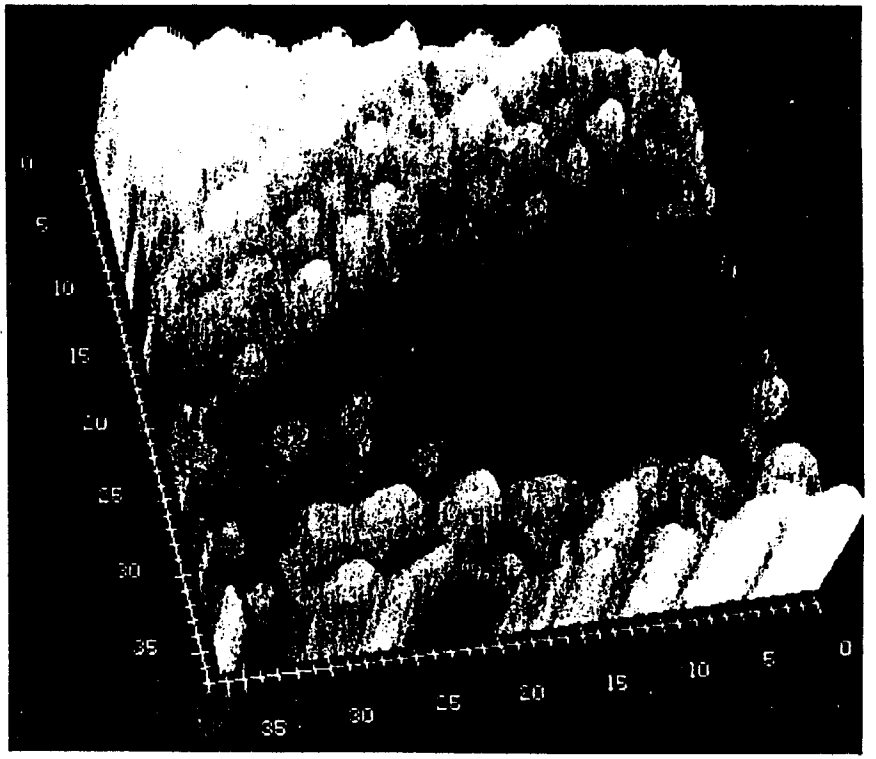

Figure 17. A three-dimensional STM image of freshly cleaved PbS{001} bombarded by 8-KeV Kr^+ ions.

date, there have not been many systematic studies of lattice damage with molecular dynamics owing to the extensive computer time required. As this technology is rapidly improving, we expect this area to be quite active in the future.

3.3. Interaction potentials

The reliability of the results from any molecular dynamics simulation depends on the quality and appropriateness of the interaction potential that is assumed in the calculation. For example if one wanted to examine the dissociative chemisorption of O_2 molecules on Ni{001}, then the potential must include the proper interactions that allow the molecules to separate into atoms on the surface and must not assume that the molecule is a point mass of 32 amu. Moreover, the repulsive part of the potential must be suitable for representing keV interactions. For example, several many-body potentials have recently been developed to examine the equilibrium properties of silicon.[72,83–86] All except one[84] of the potentials have very weak repulsive walls and are inappropriate for simulations of keV particle bombardment. It is well known that the desorption yields are in some sense inversely proportional to the binding energy of atoms to the solid. Thus, if a potential has a drastically incorrect binding energy, the predicted yields and energy distributions will also be incorrect.

In the most rigorous sense, we require a complete many-body description of the interaction potential of the model microcrystallite. The dynamical calculations must then be performed within this framework by including the interaction of each particle with all other particles. The integration of the classical equations of motion are inexorably intertwined with the form of the interaction potential function. During the early years, many attempts were made to simplify this interrelationship using the BCA. Interestingly, the BCA itself imposes certain restrictions on the potential function. We next review how the sophistication of molecular dynamics calculations has increased in recent years, beginning with the simplest models and finishing with the most complex ones. In each case we will concentrate on the potentials appropriate for the description of the substrate interactions. These interactions involve a wide kinetic energy range and are most influential in leading to particle ejection.

3.3.1. Repulsive Pair Potentials and the BCA

The simplest interaction among a group of atoms is one that is pairwise additive. In this case, the total potential energy, E, can be written as

$$E = \sum_i \sum_{j>i} V(r_{ij}) \tag{14}$$

where V is a pair-potential, r_{ij} is the scalar distance between atoms i and j, and the sums are over all the particles in the simulation. The assumption of pairwise additivity of the potentials physically means that the interaction between two atoms is independent of the presence of a third or fourth atom. This approximation is chemically not correct. For example, if pair potentials were used to describe ozone, O_3, then the molecule would be an equilateral triangle with a binding energy three times that of O_2. Both the qualitative and quantitative descriptions are wrong. Why then, has a multitude of simulations of the keV particle bombardment process used pair-potentials quite successfully?

For atomic collisions of energies greater than typical bond energies (a few eV's), strong repulsive forces dominate the dynamics. In other words, the motion of the atoms and molecules are governed by the presence of other species in a given geometrical arrangement. This structural dependence is quite strongly seen in the angular distributions of the ejected particles discussed elsewhere in this chapter. The angular distributions from different fcc materials are strikingly similar, again confirming the idea that the crystal structure dominates the collision process. Chemical effects such as the bonding of O_3 are not overly important, as least for a first-order description of the sputtering process. Thus for many years, pair potentials have been used in sputtering simulations.[13,55,80,87–93]

The pair potentials generally come in two forms—one is purely repulsive and the other includes an attractive portion at nuclear separations corresponding to bond lengths. Popular analytic forms for the repulsive portion at small internuclear distances include the Molière and Born–Mayer potentials. Both of these are described in detail elsewhere.[93] Some researchers[13] also include an attractive portion, often a Morse potential, which is splined to the repulsive potential in order to incorporate the binding interactions in the solid.

The use of a repulsive pair potential allows one to make an approximation in the integration of the classical equations that greatly reduces the required computer time. The BCA assumes that the atoms interact only with the nearest-neighbor atom. In addition, the atoms are followed in turn from the most energetic atom downward. The fact that only nearest-neighbor atoms interact means that tables of deflection angles for a given interaction potential can be stored and used from a look-up table in the computer program. This eliminates the need for

actually integrating the equations of motion and the computer time is greatly reduced. There are really two approximations in the implementations of the BCA, one that involves collision dynamics and one that involves the interaction potential. We will discuss them in turn.

The BCA assumes that only two atoms interact at a time during the collision cascade. This seems quite reasonable when the atoms have hundreds to thousands of eV of energy. For example, the BCA has been used quite successfully to model the reflection of the primary particle where there are just one or two collisions at a high energy.[94] Even for this case, however, it has been shown that the BCA is not always appropriate.[95] For sputtering, the peaks in the energy distributions (Figs. 7 and 13) occur in the range 5–10 eV. At these energies the atoms are hitting more than one neighbor at a time. Thus, for the majority of the collisions important for the ejection process, the BCA is not appropriate. The other inherent assumption in the implementation of the BCA is that the cascades are "linear." That is, the trajectory of the most energetic atom is followed until the atom "stops" by some criteria. Then the trajectory of the next most energetic atom is followed, etc. It is assumed that these motions are independent. Processes such as the ejection of dimer molecules as given in Fig. 15 above cannot be treated directly.

Although we seriously question whether the BCA is appropriate for modeling the sputtering process, especially in this era when computer resources are bountiful, computer codes such as TRIM[80] and MARLOWE[93] have been successful in modeling some aspects of the sputtering process. In addition, TRIM is routinely used to model the depth of implantation of ions into substrates. In this case the crystal sizes needed for a proper description of the ion implantation are too large for a molecular dynamics simulation.

Tied to the BCA is the use of purely repulsive pair potentials. It must be pointed out, however, the repulsive pair potentials can and have been used with molecular dynamics simulations that do not utilize the BCA.[55,87,88,90] The lack of any attractive interaction means that assumptions must be made about the surface binding energy or there will be no peak in the energy distribution of the ejected atoms. Likewise, energetic thresholds for displacements of the atoms in the solid must be assumed or the atoms would never stop moving through the solid. The incorporation of molecules such as CO or C_6H_6 on the surface is not possible if one only uses repulsive pair potentials. Some of these difficulties may be removed by including attractive interactions in the pair potentials, the next level of calculational complexity.

3.3.2. *Attractive Pair Potentials*

In the molecular dynamics simulation, it is relatively straightforward to move from pair potentials that are purely repulsive to those that include an attractive interaction. The logic in the computer program is the same. The only additional factor is that more computer time is required. Generally the interaction potentials are cut off at some distance beyond which it is assumed that the potential and force are negligible. If only the repulsive interactions are included, then this cutoff distance is typically smaller than the nearest-neighbor distance in the solid. If attractive interactions are included then this distance is increased to between the second and third neighbor atom distances. Thus interactions between more pairs of atoms are included and the computer time required is increased.

The advantage of using attractive pair potentials is that displacement energies, surface binding energies, and bond energies in molecules are automatically included in the simulation. The comparisons between the experimental and the calculated data include such detailed features as the angular distributions of Rh atoms ejected from Rh{111} as we shall see in Section 5. Many of the examples discussed in this chapter are from simulations using these potentials.

As mentioned above with the O_3 example, it is not possible to fit pair potentials to both the energy of a diatomic molecule and the energy of the corresponding bulk phase. For example, pair potentials that have been fit to the bulk heat of sublimation of Rh (5.75 eV)[96] have a well depth of 0.82 eV. The diatomic molecule, Rh_2, however, has a bond strength of 2.92 eV.[97] Conversely, if one uses the pair potential for Rh_2 to describe the bulk metal, the predicted heat of sublimation is a factor of 3.5 too large. Conceptually this same problem arises when one wants to describe the energetics of atoms in the surface layer. The pair potential formulation is not equipped to describe the interactions of atoms in a variety of bonding configurations.

Although we know that pair potentials contain inherent deficiencies, it is logical to inquire whether the experimental data are sufficiently good to find the flaws. The first evidence that pair potentials were not sufficient to describe the ejection process arose from the EARN experiments on Rh{111}. Concurrent with these experimental observations was a flurry of activity into the development of many-body potentials to describe bulk phases. Below we describe various approaches for many-body interactions, some of the first sputtering calculations using many-body potentials and our projections for the future.

3.3.3. *Many-Body Potentials—Metals and the Embedded Atom Method*

The glaring deficiency of using attractive pair potentials in the simulations of the keV particle bombardment process is shown in Fig. 13. Here the angle integrated energy distributions of Rh atoms ejected from Rh{111} from the EARN experiments and the simulations using attractive pair potentials are shown. The normalization of the curves is explained below. The most obvious problem is that the peak in the calculated curve is 2–3 eV below that of the experimental curve. No reasonable adjustment of the parameters in the pair potentials could be made to bring the peaks into alignment.

Fortuitously, about the same time that these experiments were being carried out, a functional form for describing the many-body interactions among metal atoms was presented by Daw and Baskes.[98] As with the pair potentials this embedded atom method (EAM) potential is empirical and the parameters must somehow be determined. However, the functional form is inherently many-body in nature. The first step in determining the potential is to define a local electron density at each atomic site in the solid. A simple sum of atomic electron densities has been shown to be adequate in many cases, and often a sum of free atom densities is used.[90,99] The second step is to determine an embedding function that defines the energy of an atom for a given electron density. Finally, the attractive contribution to the binding energy produced by this embedding function is balanced by pairwise additive repulsive interactions. The expression for the total binding energy is given by

$$E = \sum_i F_i(\rho_i) + \tfrac{1}{2}\sum_i \sum_j \Phi(r_{ij}) \tag{15}$$

where ρ_i is the electron density at each atomic site, $F_i(\rho_i)$ is the embedding function, and $\Phi(r_{ij})$ is the pair term arising mainly from the core–core repulsions. The function ρ_i is given by the expression

$$\rho_i = \sum_j \rho(r_{ij}) \tag{16}$$

where $\rho(r_{ij})$ is the contribution of electron density to site i from atom j and is a function of the distance r_{ij}. This dependence of the electron density on the interatomic distances facilitates the determination of the forces that are simply derivatives of the energy with respect to distance.

If free atom densities are used in the sum from Eq. (16) above, the embedding function is left to determine the properties of the condensed phase. An accurate determination of this function is therefore important

for modeling realistic systems. The approach commonly used is to fit this function to a large number of properties. For example, experimentally determined values of the lattice constant, sublimation energy, elastic constants, and vacancy formation energies are often combined with theoretically determined relations such as the universal equation of state[100] to provide an extensive data base.[99] This formalism has proven to provide both a realistic and easily evaluated potential which is suitable for describing a large range of properties of various pure metals and alloys.[67,101–111] To date, the EAM potentials have been found to be successful with close-packed metals although some progress has been made towards modeling covalent bonding by the introduction of angle-dependent electron densities.[112]

A preliminary fit of the embedding function and the core repulsive term was made to the properties of Rh metal in order to determine whether the EAM description of the interaction predicts the EARN data of Rh atoms ejected from Rh{111} better than the pair-potentials.[67] The most dramatic change in the predicted distributions is observed in the angle-integrated energy distributions. As shown in Fig. 13, the experimental and calculated distributions using the EAM interaction are in excellent agreement, while the calculated distribution using pair potentials is quite different from the experimental curve. The peaks in the polar angle distributions as calculated using the EAM potential are also found to increase by about 10° from those predicted by the pair potentials (Fig. 11). The agreement between the EAM and the experimental energy distributions is most convincing and the improvement in the accuracy of the polar distribution is encouraging.

Is the closer agreement fortuitous or is there a sound basis for it? It has been known that the pair-potential description is inadequate in the surface region, but the detailed data that exposed the nature of the deficiencies were not available. There are several fundamental differences between the EAM and the pair potentials. First, the surface binding energy of the EAM potential is larger (5.1 eV) than that of the pair potential (4.1 eV). Of note is that both potentials were fit to the bulk heat of atomization of Rh (5.76 eV). The peak position in the energy distribution is proportional to the binding energy,[21] and thus it is logical that the peak in the EAM energy distribution occurs at a higher value than for the pair potential. In addition to the larger binding energy at the equilibrium site, the EAM potential is relatively flat in the attractive portion of the entire surface region as shown in the contour plots of Fig. 18. There is more than a 4-eV attraction for the ejecting atom even above a neighboring atom, while the pair potential exerts only ~1 eV overall attraction. Thus, particles that eject at more grazing angles will ex-

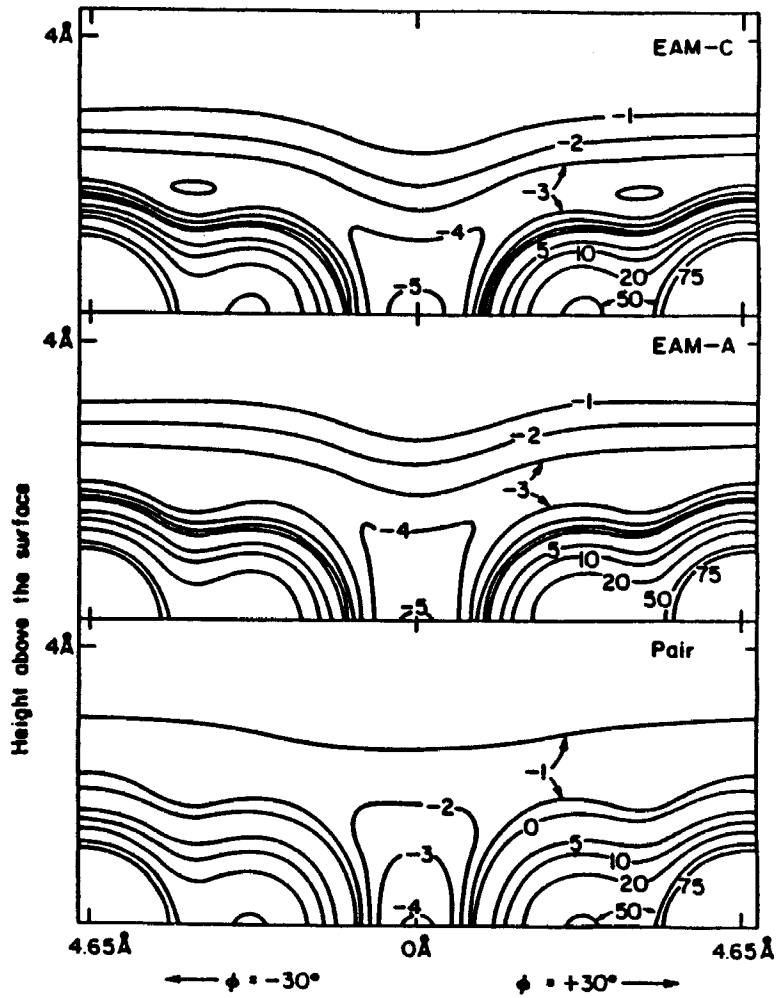

Figure 18. Contour plots of the potential energy of a Rh atom ejecting from a Rh{111} surface for the pair potential, EAM-A and EAM-C. The ordinate is the height of the atom above the surface (Å). The abscissa is the position of the atom (Å) along the surface in the $\phi = \pm 30°$ azimuths.

perience a larger attraction to the surface in the EAM potential than in the pair potential. This increase will shift the peak in the energy distribution to larger energies, reduce the ejection yield, pull the particles away from the surface normal, and move the peak in the polar distribution as seen in Fig. 13. It is the low-energy particles therefore that

are not well described by the pair potentials. The experimental and calculated energy distributions using the EAM shown in Fig. 13 are peak normalized. The area under the pair-potential curve is about 2 times that of the EAM curve. This ratio is obtained from the ratio of the calculated yields. This normalization quite clearly shows that it is the low-energy particles that have been inhibited from ejecting when the EAM potential is used in the simulations.

Recently the previously developed Rh{111} EAM potential has been employed to model the ejection process from Rh{331}, a stepped surface that consists of {111} terraces three atoms wide with a one-atom step height.[113] In this surface there are atoms that are both more and less coordinated than on the {111} surface. As we shall see in Section 5, the agreement between the experimental and calculated angular distributions is excellent. This same EAM potential was used for the Rh interactions in the O/Rh{111} study and is also discussed in Section 5.

In a similar study, Lo *et al.* have compared the characteristics of atoms sputtered from copper surfaces in simulations that used both pair potentials and EAM potentials.[114] Significant differences were found for many properties of interest, including the peak in the energy distributions. Although adjustment of the potentials to fit experiment was not attempted, this study concluded that many-body potentials are required to realistically model much of the sputtering process.

The EAM approach appears to provide a formalism within which realistic potentials describing atomic dynamics can be developed. It should also provide a method for realistically incorporating adsorbates into dynamics simulations. Both of these applications can be considered significant advances, and will help molecular dynamics simulations to continue to contribute to the understanding of keV particle bombardment processes.

3.3.4. Many-Body Potentials—Silicon and Covalent Solids

Even more difficulties arise when attempting to describe covalently bonded systems such as silicon or even proteins. The crux of the problem is that there is a strong angular dependence in the bonding since the number of neighbors is smaller than in close-packed systems. For improperly constructed potentials, the system will tend to collapse into a close-packed array of atoms during the molecular dynamics simulation. There has been a flurry of activity recently centered mainly on describing solid silicon. Silicon serves as a good model system since it is homonuclear.

A convenient starting point for developing covalent interactions is to write the energy as a many-body expansion of the form

$$E_{tot} = V_2 + V_3 + V_4 + \cdots \quad (17)$$

where the first term represents a sum over pairs of atoms, the second term represents a sum over triads of atoms, etc. A well-known example of this type of expansion, even though restricted to atomic displacements near equilibrium, is the valence-force field. While this expression is exact if all terms are included, computational restrictions demand that it be truncated. In most applications, it is truncated at three-body interactions. This is partly for computational convenience and partly because the three-body term can be written in the form of a bond-bend—a concept that is physically appealing. While this approach is well developed for few-body, gas-phase reactions,[115-116] it has only recently been extended to condensed phases.

Silicon has been the test case for potentials of this type, and so this discussion will be restricted to this element. The most widely used silicon potential was developed by Stillinger and Weber.[72] The interactions used are composed of a sum of two-body and three-body terms, with the three-body interactions serving to destabilize the sum of the pair terms when bond angles are not tetrahedral. The parameters for this potential were determined by reproducing the binding energy, lattice stability, and density of solid silicon and also by reproducing the melting point and the structure of liquid silicon. Although this potential was originally developed to model liquid–solid properties, subsequently studies have demonstrated that it also provides a good description of the Si{001} surface.[117,118] The wide applicability of this potential can be considered a testament to the care (and computer time) invested by Stillinger and Weber in its development.

A simpler potential of the form of Eq. (17) has been used by Pearson *et al.* to model Si and SiC surfaces.[83] The two-body term is of the familiar Lennard–Jones form while the three-body interaction is modeled by an Axilrod–Teller potential.[119] This potential form is restricted to weakly bound systems, although it apparently can be extended to model covalent interactions.

Brenner and Garrison introduced a potential that was derived by rewriting a valence force expression so that proper dissociation behavior is attained.[84] Because the equations were extended from a set of terms that provided an excellent fit to the vibrational properties of silicon, this potential is well suited for studying processes that depend on dynamic properties of crystalline silicon. For example, Agrawal *et al.* have studied

energy transfer from adsorbed hydrogen atoms into the surface using this potential.[120]

While these potentials have been successful in modeling dynamic processes on silicon surfaces, the many-body expansion as applied in this case suffers from several drawbacks. Because each of the three potentials above has been fit to properties of the crystalline silicon solid, they implicitly assume that the bonding is tetrahedral in nature. Atoms on the surface of silicon are known to exhibit nontetrahedral hybridizations, and so the results for surfaces are at best uncertain. Also, none of these potentials reproduce accurately the properties of the Si_2 diatomic molecule. This again inhibits a complete description of surface reactions.

A related potential form, primarily developed to reproduce structural energetics of silicon, was introduced by Tersoff[85,121] and later by Dodson[122] and was based on ideas discussed by Abell.[123] The binding energy in the Abell–Tersoff expression is written as a sum of repulsive and attractive two-body interactions, with the attractive contribution modified by a many-body term. The stability of the diamond lattice is achieved by modifying the attractive pair terms according to local coordination, so that the atomic binding energy is at a minimum when each atom has four nearest neighbors. The parameters in this potential were determined by fitting to the properties of the Si_2 molecule, and by reproducing the binding energies and lattice constants of several crystal structures of silicon. The Tersoff style potentials are expected to yield a good overall expression for silicon because they correctly describe the isolated dimer, and because they are fit to nontetrahedral structures. This means that they should provide an adequate description of silicon surfaces, although thorough testing is still being carried out.[121]

Additional silicon potentials have also been introduced, but they appear to be cumbersome for studying large numbers of atoms.[86] Also, several of the silicon potentials mentioned above have been modified to represent germanium, carbon, and the heteronuclear compounds SiC and SiGe.[124-125]

To date two simulations on the keV particle bombardment of silicon using many-body potentials have been performed. Stansfield *et al.*[71] have modeled Ar bombardment of Si{100} and the dimer reconstructed Si{100}(2 × 1) surfaces using the Stillinger and Weber potential.[72] They found that, for bombardment at energies between 100 and 1500 eV, Si atoms ejected from 1–4 layers in the solid. This is in contrast to bombardment of the low index faces of metals where the ejection is primarily from the first atomic layer. Smith *et al.*[126] modeled the Ar bombardment at 1000 eV of Si{110}, Si{100}, and Si{100}(2 × 1) using the Tersoff-II potential and showed that the angular distributions are very

sensitive to the structure of the original surface. Both studies showed that the important collision mechanisms in the solid were different than for close-packed systems because of the openness of the crystal. This is especially apparent in the energy distributions as shown in Fig. 19.[126] The sublimation energy of Si is 4.63 eV, yet the peak in the energy distribution occurs at about 7.5 eV. The openness of the crystal prevents randomization of the energy and thus the distributions are not described by the transport theory expressions.[21] On a technical note, the Smith study shows that a moving atom approximation can be used reliably to reduce the required computer time for the simulation.[126]

The silicon and carbon–germanium potentials are certainly a significant step forward in terms of having realistic many-body potentials for describing bulk phases. However, the reactions of molecules ranging from H_2 and C_2H_4 to DNA on the surface are also of interest. Many-body potentials for these systems are just now beginning to be developed and have not as yet been used in simulations of the energetic particle bombardment event.

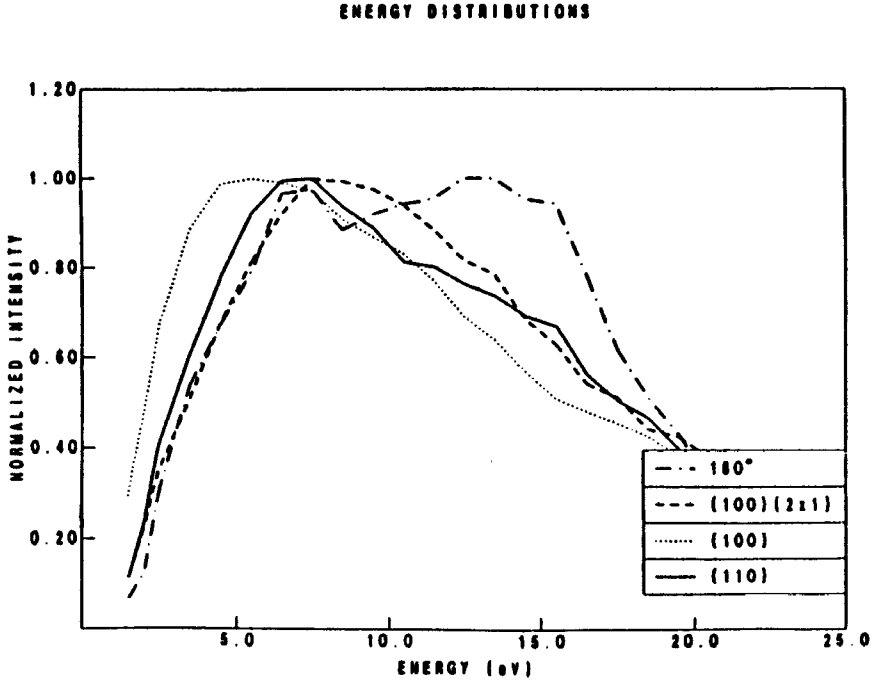

Figure 19. Angle-integrated distributions as a function of crystal face. The fourth curve is for Si_x atoms that eject from Si(110) at $\theta = 40° \pm 10°$ and $\varphi = 180°$, i.e., the most intense feature of the angular distribution. In all cases the Ar had 1000 eV of kinetic energy.

3.3.5. *Many-Body Potentials—Reactions on Surfaces*

The main many-body interaction that has been used for reactions of gases (mainly diatomic molecules) with surfaces has been a modification of the London–Eyring–Polanyi–Sato (LEPS) method used successfully for gas-phase potential surfaces.[127] The spirit of this type of approach is to consider the entire surface as one body of a few-body reaction. This method has been used for examining the reaction of H_2 on W{100},[128] H_2 on various Cu faces,[129–131] the dissociative chemisorption of N_2 on W{011},[132] the anisotropic chemisorption of O_2 on Ag{110},[133] and the abstraction of a C atom adsorbed on the Pt{111} surface by a gas-phase O atom.[134] There are two problems with using the LEPS potential for simulations of keV particle bombardment. First, the LEPS approach requires diagonalization of a matrix at each integration step. The size of this matrix increases dramatically with the number of particles. For large systems the computer time will be quite large. Secondly, in the reactions studied to date, the surface has just been a heat bath and surface atoms have not participated directly in the reaction. In the sputtering process, the entire surface cannot be thought of as one body of a many-body system. The LEPS matrix would be astronomically large. Although this formulation of a potential for gas reactions with solid surfaces is not quite optimal for sputtering simulations, in the very near future some formulations may well be. .

3.3.6. *Many-Body Potentials—Molecular Solids*

Recently Brenner has developed a many-body potential for modeling the chemical reactions in shock waves.[135] The protypical reaction is

$$2NO(g) \rightarrow N_2(g) + O_2(g) \qquad (18)$$

Brenner's potential is based on the Tersoff–Abell approach for many-body interactions described above. The key feature is that one potential surface describes the bonding interaction in NO, the van der Waals interaction among NO molecules, the bonding interactions in N_2 and O_2, and the van der Waals interactions among the product molecules. This is real reaction chemistry. This type of potential could well describe the events that take place when water ice is bombarded in the high-dose regime and eventually O_2 is ejected. Obviously during the course of the experiment, reactions are taking place that cause the formation of O_2 in the solid. As with LEPS potentials, this type of potential may not prove to be the best for use in sputtering calculations. However, there is no doubt that potentials will be developed to examine complex reaction systems useful in simulations of the particle bombardment process.

3.3.7. *The Future*

We are very optimistic that in the near future very realistic potentials will be available for examining chemical reactions in bulk phases and at surfaces. Already the EAM potentials have been used to predict which of the face-centered-cubic {110} surfaces will reconstruct and which will not.[100,136,137] We have performed molecular dynamics calculations of the microscopic reaction mechanisms that are important for the opening of the dimers on the Si{100}(2 × 1) surface during molecular beam epitaxy.[138,139,140] As mentioned above, Brenner has examined chemical reactions in shock waves. The ability to model the reaction of ethylene on Rh{111} to form ethylidyne is not that far away. There is considerable activity in modeling the van der Waals interactions among protein and DNA molecules. These groups are also interested in incorporating chemical reactions into their approach. A merging of their potentials with others for the bulk substrate will make the modeling of the sputtering of a protein from a surface possible. Of note is that as the potentials improve, it will also be possible to examine events such as damage quite realistically. The nature and distribution of the defects could be reliably predicted.

There is one broad class of potentials that we have omitted from this chapter. In all the cases discussed above, we have assumed that the reaction occurs on one potential surface, that is, electronic effects have been omitted. Potentials to describe both the neutral and charge transfer states are still a long way from being developed for a large number of atoms. In addition, if there are electronic effects, then some quantum mechanics is needed in the dynamical description. Performing calculations to describe the charge transfer among many particles is still far off.

4. Electronic Effects

There is ample evidence to believe that the dynamics of neutral particle motion subsequent to the ion impact event is reasonably well understood for quite a few different types of systems. Electronic excitations that may accompany the classical motion, however, add an enormous degree of complexity to the theory. It is extremely important to be able to predict how important these excitations may be. In SIMS, for example, it has been known for many years that the number of ions detected is more dependent on the electronic properties of the matrix than on the concentration of the species on the surface. This very practical annoyance, however, presents a challenging fundamental problem to investigate and understand. What are the electronic events that occur in the solid due to the keV particle bombardment and how do these influence the properties of the ejected particles?

In this section we focus on those theories and experiments that help to extract the underlying mechanism of the excitation/ionization/neutralization process. Although an understanding of these mechanisms will ultimately be crucial to performing better quantitative measurements with SIMS, it is not certain that such a goal is yet possible, given the potential complexities of the electronic events. It is not clear, first of all, that one theory is applicable to all types of electronic processes. Should a theory appropriate for metals where there is significant electron delocalization be also appropriate for an oxide where there are localized electron densities? Can one always assume that the electronic states of the substrate connected to the ejected species is the same as the original quiescent surface? The figures in Section 3 would lead one to doubt this assumption.

A final consideration, and a nontrivial one at that, is to directly compare experimental with theoretical results. In the laboratory, it would be desirable to measure the intensity of each electronic state of the desorbing particle as a function of velocity (v) and angles of ejection (θ, φ). For simplicity, assume that the ion and neutral atom distributions are under consideration. The measured ion intensity is $I^+(v, \theta, \varphi)$ and the measured neutral distribution is $I^0(v, \theta, \varphi)$. The temptation is to define the ionization (or excitation) probability as

$$R^+(v, \theta, \varphi) = I^+(v, \theta, \varphi)/[I^0(v, \theta, \varphi) + I^+(v, \theta, \varphi)] \qquad (19)$$

Here v is the measured velocity of each particle, θ is the polar angle as measured from the surface normal, and φ is the azimuthal angle.

The problem with this definition is that ions and neutral atoms depart the surface region with trajectories that are influenced by different potential energy surfaces.[141] For a particle near the solid surface, two schematic potential curves are shown in Fig. 20. At the time of collision, assume the particle is at the bottom of the lowest surface-potential well($-D$) and has a kinetic energy E' and velocity v'. There is a curve crossing or decision point at a distance z^* from the surface. At this point, the particle has energy $E^+(=E' - D)$ and corresponding velocity v^*. If the particle ejects along the neutral surface (lower one) the measured velocity will also be nearly v^*. However, if the particle is ionized, there is still a barrier of energy ΔE that must be overcome before the particle finally reaches the detector. An image charge in the solid is one possible source of this energy barrier.

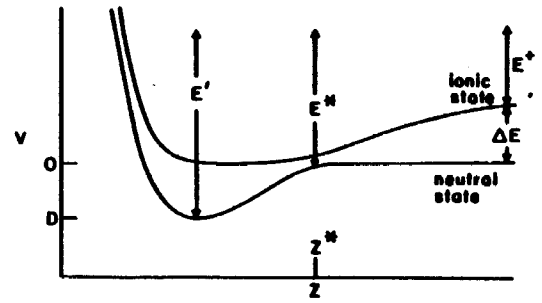

Figure 20. Schematic potential energy curves for a particle at a distance z from the surface.

The easiest way to analyze the experimental data in order to extract the ionization probability is to determine the ratio of the ion to neutral yield as a function of the measured velocity of each species. However, to compare the neutral and ionic particles that had analogous histories of motion in the solid, the neutral species that eject with v^* must be compared with ions that eject with velocity v^+ where $(v^+)^2 \propto E^+ = [(v^*)^2 - 2\Delta E/m]$. The appropriate ratio for ejection normal to the surface thus becomes

$$R^+(v^*) = I^+(v^+)/[I^0(v^*) + I^+(v^+)] \tag{20}$$

or

$$R^+(E^*) = I^+(E^* - \Delta E)/[I^0(E^*) + I^+(E^* - \Delta E)] \tag{21}$$

Furthermore these expressions might be expressed in terms of the velocity associated with the energy E'.

Given the above complications, we proceed with some highlights of experiments and theories that help to elucidate the fundamental processes of electronic motion. The two most fundamentally sound theories are the resonant tunneling model and the bond-breaking model. A number of reviews[142–150] on both of these have appeared over the years so we will only give an overview. In fact, these two models are quite similar; however, they are generally applied to different types of systems. The tunneling model is generally used to describe charge exchange in systems where there are delocalized electrons (e.g., metals) whereas the bond-breaking model is more applicable to systems where there are localized electron densities (e.g. oxides). In addition to the above models, which are primarily for describing ionization events, we also describe a model that explains the velocity distributions of neutral atoms in excited electronic states. Our particular focus in this review is to emphasize the current need to connect the ionization theories which

involve macroscopic parameters such as work function to the dynamics of nuclear motion in the solid.

4.1. Tunneling Model

The tunneling model has been one of the most widely applied explanations for the work function and velocity dependences of the ionization probability of species ejected from metal surfaces. A number of workers[141–154] have given excellent descriptions and reviews of the topic so a brief summary will be given here along with experimental examples that illustrate different features of the predictions of each model.

The main concepts behind the tunneling model are shown schematically in Fig. 21. The free-electron-like metal surface is assumed to be smooth with no inhomogeneities and has a Fermi energy, E_F, which is equal to the work function ϕ. The sputtered atom (assumed for this discussion to be one that will form a cation) has an energy level E_a. When the atom is at infinity, this energy is the ionization energy. At closer distances to the surface, the energy level shifts upward due to the image potential. Finally the electron in the atomic energy level has a finite lifetime, so the level is broadened with a half-width of $\Delta(z)$. The

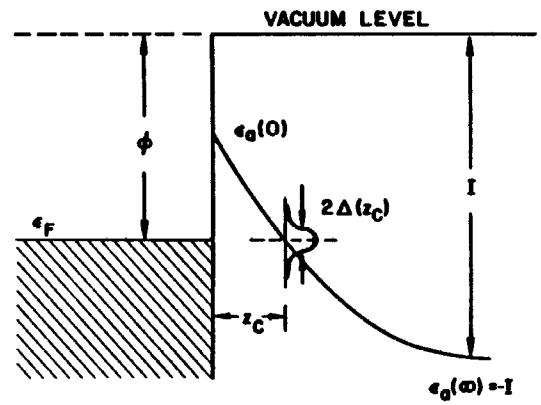

Figure 21. Schematic energy diagram of an atom leaving a metal surface. The Fermi level E_F lies below the vacuum level by the work function value ϕ. Initially the atomic level E_a is broad and may lie above E_F before the atom is sputtered off. The variation of the image potential causes E_a to lower with separation until $E_a = E_F$ at the crossing point. Electrons in the metal can tunnel out to fill the atomic level once $E_a < E_F$ beyond the crossing point (From Ref. 147.)

essence of the tunneling model then is that electrons can tunnel between the atomic level and levels in the solid of the same energy.

Lang[151] has made the assumption that the particle moves in a straight line trajectory

$$z = v_\perp t \tag{22}$$

where $v_\perp$ is the velocity component perpendicular to the surface and t is the time. This assumption, coupled with the idea that the critical-level width is determined at the point when the atomic energy level equals the Fermi energy, yields the following expression for the ionization probability:

$$R^+ \propto \exp[-2\Delta(z^*)/\hbar\gamma v_\perp] \tag{23}$$

where γ is the decay length of the width of the atomic level. Since the crossing point, z^*, depends on the Fermi energy or the work function, the above equation reduces to

$$R^+ \propto \exp[-c(I - \phi)/v_\perp] \tag{24}$$

or

$$R^- \propto \exp[-c(\phi - A)/v_\perp] \tag{25}$$

where A is the electron affinity of the sputtered anion. The energy difference ΔE of Fig. 20 is $(I - \phi)$ or $(\phi - A)$.

This model predicts that the ionization probability depends on the difference in the ionization energy and the work function and on the perpendicular velocity of the sputtering atom. Some of the more detailed experiments that test the ideas in this model have been performed by Yu and co-workers. In one experiment Cs was adsorbed onto a substrate at a fractional monolayer coverage. The work function of the surface was then systematically varied by coadsorbing small amounts of Li. The intensity of Cs^+ ions ejected as a function of the work function change was then carefully measured.[155] As shown schematically in Fig. 22, if the work function is larger than the ionization energy, then the probability of an ion being ejected is unity. The electron remains in the metal which has a lower energy state. For smaller work functions, the atomic level crosses the Fermi level and thus the ionization probability depends exponentially on the difference between the ionization energy and the work function. Shown in Fig. 23 is the measured Cs^+ ion intensity as a function of work function along with the predictions of Eq. (23).

In another set of experiments Yu measured the O^- ion intensity for different angles of ejection.[156] This approach allowed a clever means of changing $v_\perp$ without changing v. As shown in Fig. 24 the ion intensity

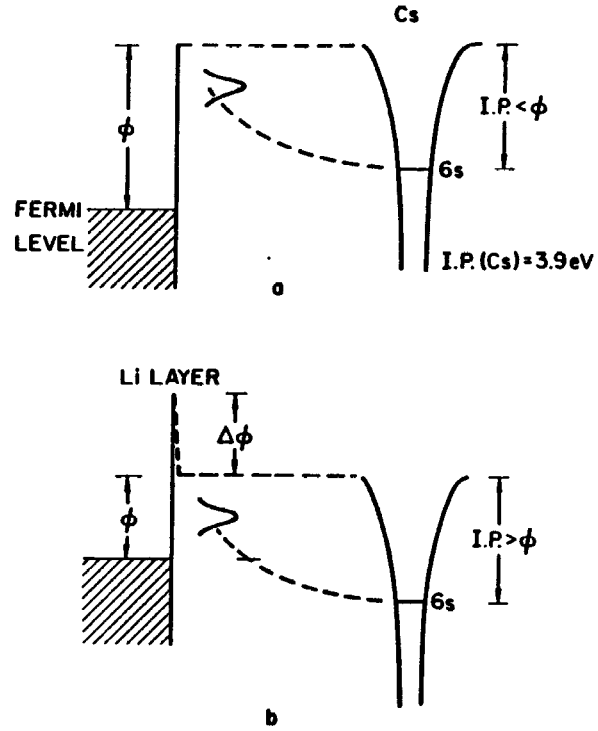

Figure 22. Schematic energy diagram for the sputtering of (a) $\phi > I$, (b) $\phi < I$ after the work function is lowered by the deposition of Li. (From Ref. 147.)

depends exponentially on the inverse of the perpendicular velocity except for small velocities. This seems to indicate that the tunneling model is appropriate for predicting the ionization probability of ions that eject from metal surfaces.[156–159] There are a number of other studies, both experimental and theoretical, however, which predict that R^+ should be proportional to $v_\perp^n$ where n is between 0 and 3.[160–162] It is not clear how well in many cases the ionization probability has actually been measured. Often only the energy distribution of the ions has been measured at one exiting angle. The neutral distribution is assumed to follow that predicted by Thompson.[21] As discussed above the assumptions of isotropy inherent in this model and the ad hoc choice of the heat of sublimation as the energy cost to remove an atom are not fully established.[47,48,51,52,53] In addition, the choice of velocities at which to compare the ion and neutral distributions must be carefully evaluated.[141]

Although the tunneling model appears to do quite well in

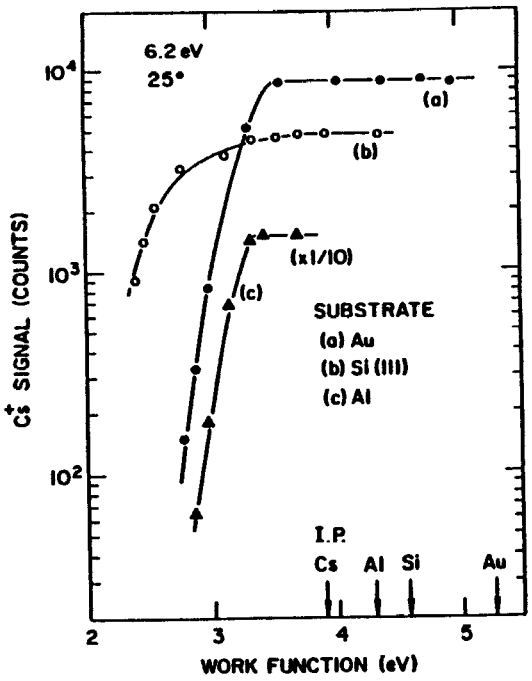

Figure 23. A 1-nA, 500-eV Ne^+ beam was used to sputter in the static mode. The Cs^+ ions emitted have a $v_\perp$ of 2.7×10^5 cm/s. (From Ref. 155.)

accounting for the experimental observations, the pictures presented by the dynamics simulations leave one concerned about several of the fundamental assumptions of these approaches. One feature that the dynamics simulations point out is that the velocity of the ejecting atom is not constant as is assumed in Eq. (23). In model cluster calculations of an ionization model, it is possible to systematically vary the binding energy of the atom to the surface and also to monitor the initial velocity and the measured velocity.[163] As shown in Fig. 25, the ionization probability scales with the initial velocity (v' of Fig. 20) rather than the measured velocity (v^*). This effect was used by Yu and Lang to explain the low velocity deviation of the O^- intensity from the tunneling model prediction.[155]

The other assumption of concern is that there is a homogeneous electron density in the metal. In the pictures shown in the previous section, the environment around the departing atom can be severely distorted. There are some ion impacts, however, where there is significantly less damage around the ejection site. Harrison[ ] and

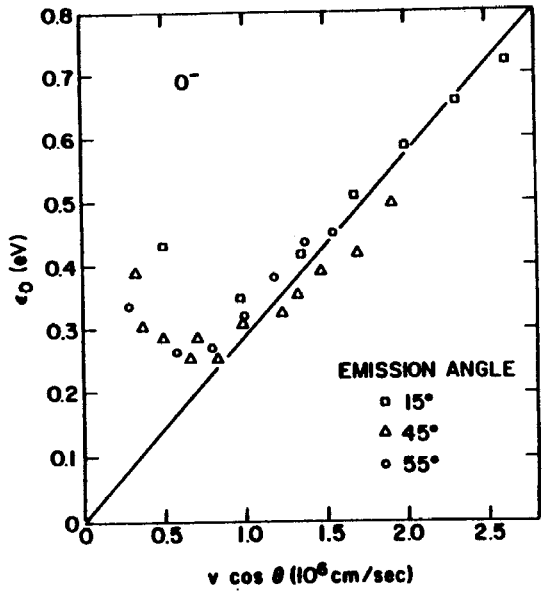

Figure 24. The dependence of ϵ_0 for O^- sputtered from oxygenated Nb surfaces on the normal component $v_\perp$ of the emission velocity. Here $\epsilon_0 = v_\perp/c$ of Eq. (24). (From Ref. 156.)

Williams[143] have suggested that *megaevents*, that is, impacts where there is significant damage in the surface region at the time of particle ejection, may require a different model of ionization. In this regime, the electron density may be severely distorted. In a similar vein, Nourtier[164] has assumed that for metal ion ejection from the same substrate, specific collision sequences may preferentially give rise to ion ejection.

4.2. Bond-Breaking Model

To account for the presence of an inhomogeneous electron density, Slodzian[145] and Williams[143] have proposed a bond-breaking model which is based on the Landau–Zener model.[165] The process is depicted in Fig. 20 and is similar in spirit to the tunneling model except that at the crossing point (z^*) there are discrete levels rather than a continuum of levels in the substrate.[148] As developed by Yu[166] the ionization probability for the bond breaking model is given by

$$R^+ \propto \exp(-2\pi H_{12}^2/v\,|a|) \tag{26}$$

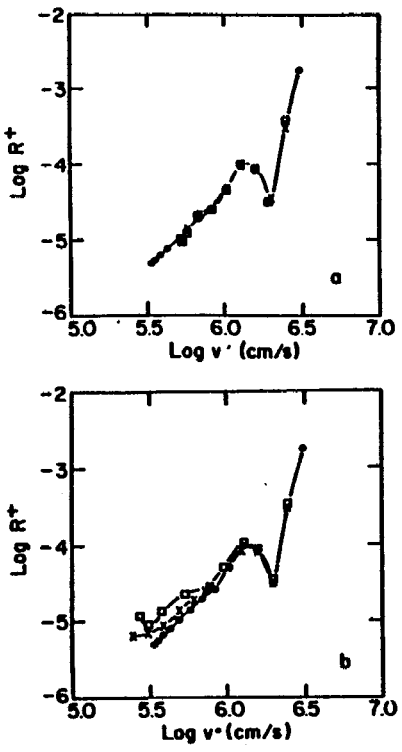

Figure 25. Log R^+ vs. log v for different binding energies, D: •, $D = 0.0$ eV; ×, D = 0.8 eV; □, D = 1.6 eV; (a) $\theta = 0°$, $v = v'$; (b) $\theta = 0°$ $v = v^*$. (From Ref. 163.)

where H_{12} is the overlap integral between the diabatic ion and covalent curves, v is total velocity, and $|a|$ is the difference in the slopes of the two diabatic curves, all evaluated at the crossing point. The velocity at the crossing point can be written as

$$v = [2(E^* + I - A)/m]^{1/2} \tag{27}$$

where $I - A$ is the energy difference between the two potential curves (Fig. 20) at infinity. For positive ion emission, I is the ionization energy of the departing cation and A is the electron affinity of the vacancy left behind. Of extreme importance is that this electron affinity is a *local* property and not the *work function* of the substrate. It is, in fact, the observation that the ion yield does not depend on the work function that allows one to assume that the bond breaking model is valid.[148]

The fact that the ionization probability in the bond-breaking model is local implies that the ion yield is proportional to coverage as long as the environment of the departing ion is constant.[167] Shown in Fig. 26 are the Si^+ and O^- SIMS intensities from a silicon sample that has been

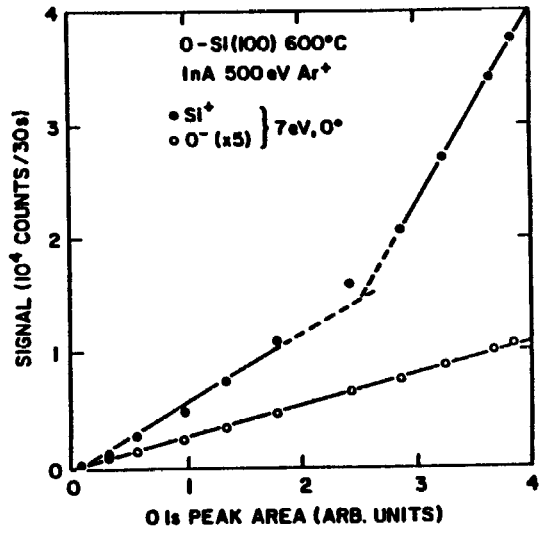

Figure 26. Sputtered Si^+ and O^- yields as a function of oxygen coverage (≤2 monolayers). (From Ref. 167.)

exposed to varying amounts of oxygen. The oxygen concentration on the surface is assumed to be proportional to the O 1*s* signal as measured by x-ray photoelectron spectroscopy (XPS). The signals are clearly linear in oxygen surface concentration. The O^- signal has only one slope. indicating that it maintains a constant environment. The Si^+ signal, however, changes slope. At the same oxygen coverage where the slope changes, the Si 2*p* signal also shifts peak position, indicating that the Si atom environments have changed.

The basic ideas behind the tunneling and bond-breaking models are quite similar. As an ion departs the surface, it reaches a decision or crossing point. In the case of the tunneling model, this crossing point occurs when the energy of the atomic level crosses the fermi level. In the case of the bond-breaking model it is the distance at which the ionic and neutral adiabatic curves cross. Both of these models have attained widespread acceptance and a multitiude of experimental data can be explained by them. However, there are constants in each that cannot be predicted theoretically and are thus used as fitting parameters to the data. It would ultimately be desirable to be able to predict the ion yields *a priori* from a first-principles theoretical basis. Factors such as the effect of individual collision sequences or different local environments (a terrace site versus a kink site) on the ionization probability are not known. In

addition, these effects are quite difficult to examine experimentally. Of note is that development of theories and experiments to predict the ion yield from a single element substrate (e.g., Ni^+ from Ni) are only in very premature stages of development.

4.3. Deexcitation Model for Sputtered Excited Neutral Atoms

One of the consequences of both the tunneling and bond-breaking models is that energy distributions of the ions peak at a larger value than the neutral distributions. A similar observation has also been made for the excited fine structure states of Ba ^1D and ^3D,[168] Ca $^3P_2$,[169] and Fe $^5F_5$[170] relative to the ground state distributions. On the other hand, the excited state distributions of Zr[171] and Fe[172] were found to be similar to the ground state distributions. Recently the energy distributions of In atoms in both the ground ($^2P_{1/2}$) and excited ($^2P_{3/2}$) states have been measured.[173] In this case the excited state distribution peaks at a *lower* energy than the ground state distribution.

A model to predict the amount of relaxation of an excited fine-structure state has recently been proposed.[173] In one limit are fine-structure states such as the ^5D_J, $3d^44s^2$ manifold of Fe and the ^3F_J, $4d^25s^2$ manifold of Zr. The fine-structure states are determined by *d*-electron coupling and not by *s*-electron coupling. In these cases the *s* orbitals are larger than the *d* orbitals, and effectively shield the *d* electrons from interaction with the metal conduction band as the atom departs from the surface. Consequently, relaxation processes have long lifetimes and the velocity distribution is independent of atomic state.

In the intermediate regime are the ^5F, $3d^74s^1$ state of Fe, the $^3P_2$, $4s^14p^1$ state of Ca, and the $^{1,3}D$, $6s^15d^1$ states of Ba. Here the velocity distributions of the excited states are broader than the ground-state distribution. Of note is that the Ba distribution depends on the electronic environment of the original matrix,[168] i.e., Ba metal, BaO, or BaF_2. The $^{1,3}D$ distributions from Ba metal and BaF_2 are broader than the one for the ^1S ground state, indicating that there is interaction of the 6*s* or 5*d* electron with the substrate. For BaO the distributions of the *D* states are similar to the ground state. The calcium process is very similar to the Ba system except that the $^{1,3}D$, $4s^13d^1$ states of Ca are not metastable in vacuum and will radiatively decay. In this intermediate case, there is partial shielding of, for example, the $3d^7$ electrons in Fe(^5F_J) by the $4s^1$ electron.

The first example of the third regime is In(^2P_J). In this case, the fine-structure states are determined by *L-S* coupling of the outermost

electron. The interaction of the 5*p* electron with the conduction band is strong and the atoms in the $^2P_{3/2}$ state are effectively deexcited to the $^2P_{1/2}$ state.

There are implications of this proposed model. First, for the well-shielded cases, the populations of atoms in each state cannot be influenced by the interaction of the departing atom with the surface, but rather by some event that occurs in the solid. It is possible that the probability of initial excitation of the *d* electron structure is determined by the degree of the electron–gas disturbance induced by the incoming bombarding particle.[174] The experimental results of the populations in the high-shielding cases show a dependence on the kinetic energy of the incoming ion.[171,172] Since there is no deexcitation as the atom departs from the surface, as determined from the velocity-distribution shapes, then the measured excited-state populations reflect the excitation process. For the moderate-shielding and exposed cases, the final-state populations reflect both the initial excitation process and the deexcitation as the atoms depart from the surface region.

There are several aspects of these proposed ideas that can be tested and examined further. Obviously, there are other elements and associated fine-structure states that will fit into the three categories. These systems can be investigated. The *a priori* determination of the interaction strength should be examined. It would be desirable to find other examples like In($^2P_{3/2}$) where the excited state is completely deexcited.

Our understanding of the ionization process for metal substrates has increased substantially in the past decade. The need is for more detailed measurements of both the ion and neutral distributions and for theoretical models that combine both the nuclear and electronic motion.

In the next section, we move forward with this knowledge to what we can learn about the structure and chemical reactivity of surfaces using these ion-beam methods.

5. Surface Characterization with Ion Bombardment

At this point, it is hopefully clear that much is known about the details of the ion–solid interaction event, of the significance of energy and angular distributions of desorbed particles from single crystals, of the mechanisms of cluster formation and of the excitation processes that lead to ionization. With this important theoretical base, it is now particularly appropriate to examine the potential application of ion beams to a variety of surface characterization experiments. There are a number of aspects to these applications that merit special consideration. First, the theoretical

modeling has suggested that the angular distributions reflect the near-surface structure. Secondly, these same calculations indicate that a large majority of the particles eject from the first layer to the target. And finally, the models suggest that the composition of the ejected clusters should embody in some fashion the chemical nature of molecular species that may exist on solid surfaces. Experimentally, as noted in Section 2, there are a number of options for realizing these applications. The detection of desorbed neutral particles is possible via several sensitive detection schemes. The detection of desorbed ions is also straightforward, both with high mass resolution and with high sensitivity. In this section, then, a sampling of the applications of importance to surface science will be reviewed. We shall restrict our examples, however, in two important ways.

Only those experiments performed using low doses of primary particles will be emphasized. Moreover, we shall focus mainly on reasonably well-defined experimental systems—those performed in UHV and/or with single-crystal substrates. These experimental aspects are critical for comparisons to theory and for elucidation of elementary surface chemical processes.

5.1. Surface Structure Studies

5.1.1. Trajectories of Substrate Species

It is of fundamental interest to accurately measure the trajectories of an atom in its ground electronic state desorbing from an ion bombarded single-crystal substrate and to compare these trajectories with those calculated using the molecular dynamics simulations. These measurements have become possible in the last few years using the EARN technique and are extremely important for validating the reliability of any theory. The Rh{111} surface bombarded at normal incidence by 5 keV Ar^+ ions has served as a convenient model system for these studies.[45] The structure of this surface, as in Fig. 12, has been well characterized using LEED and is known to exhibit little surface relaxation or reconstruction that might complicate the analysis. Note that for the {111} face of this face-centered-cubic lattice, the surface atoms exhibit sixfold symmetry. The three second-layer atoms, however, create bulk threefold symmetry with characteristic azimuthal directions along ⟨111⟩ ($\phi = 0°$ in our notation), ⟨211⟩, $\phi = -30°$, and ⟨112⟩, $\phi = +30°$. The experimental EARN distributions for this crystal face along $\phi = \pm 30°$ are shown in Fig. 27. The measurements were recorded by bombardment at normal incidence with a series of 200-ns pulses of 5 keV Ar^+ ions

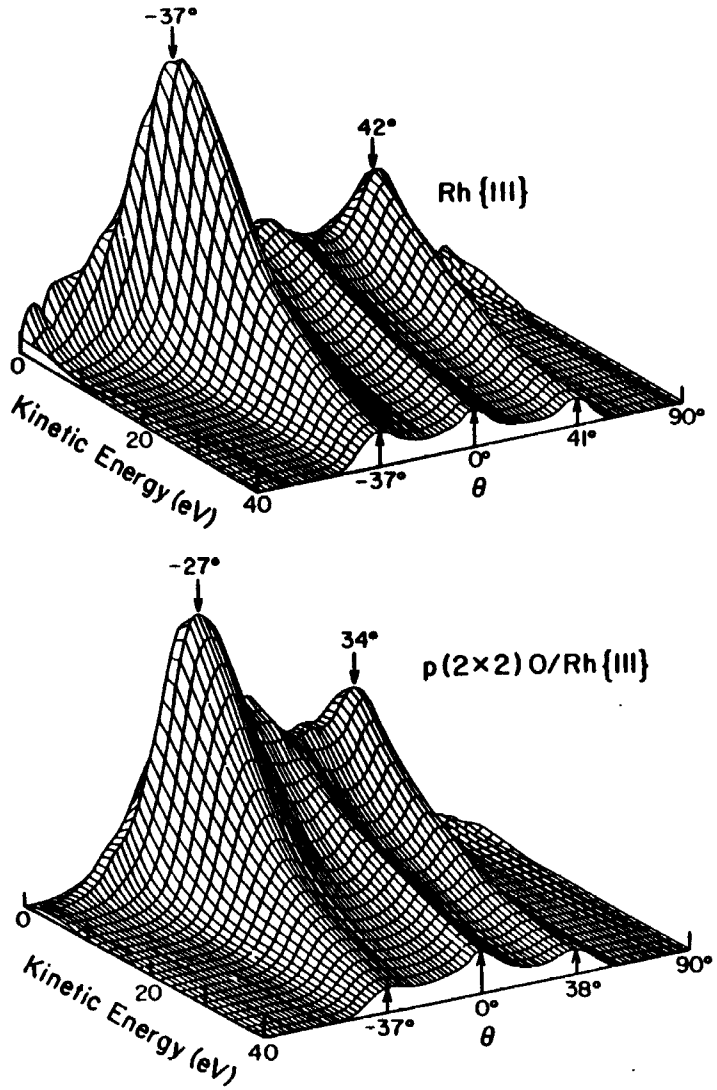

Figure 27. The EARN intensity maps for clean Rh{111} and $p(2 \times 2)$O/Rh{111}. The plots are normalized to the highest intensity peak in both cases. The positive values of θ are recorded along $\phi = 30°$ and the negative values of θ are recorded along $\phi = -30°$. (From Ref. 45.)

($\sim 2 \times 10^6$ ions/pulse). The desorbed Rh atoms were then ionized above the surface using the laser-based MPRI method described in Section 2. It is important to note that these data were recorded with a total dose of less than 10^{11} Ar^+ ions/cm^2 so that the influence of surface damage is minimized.

It is possible to gain a great deal of mechanistic information from these trajectories by comparison to molecular dynamics calculations performed using either pair potentials or many-body (EAM) potentials. These sequences begin with the alignment of atomic motions inside the solid. As these motions cause ejection of first-layer atoms, further focusing is caused by channeling or blocking by other first-layer atoms. For example, the highest intensity is observed along the open crystallographic directions ($\phi = \pm 30°$ in our case) and the minimum intensity is observed along the close-packed crystallographic direction ($\phi = 0°$). If only surface processes were important, the peaks at $\theta = -37°$, $\phi = -30°$ and $\theta = 42°$, $\phi = 30°$ should be equal in intensity and not unequal as shown in Fig. 27. The additional intensity at $\theta = -37°$, $\phi = -30°$ arises mainly from the ejection of atom A by atom B (Fig. 12) with first-layer focusing by other surface atoms. The peak at $\theta = 42°$ and $\phi = 30°$ is lower in intensity by a factor of 0.5 at low kinetic energy (KE) since no such mechanism is available along this azimuth. The peak at $\theta = 0°$ arises mainly from ejection of the second-layer atom B which is focused upward by three surface atoms. As noted in Section 3, these curves may be accurately calculated using the EAM–molecular dynamics approach, a powerful testament to the validity of the channeling and blocking concepts.

A simple test of the consistency between experiment and theory is to examine other crystal faces of Rh and to look for similar channeling and blocking mechanisms. Although there has not yet been a great deal of data of this type, a recent study on Rh{331}, an atomically stepped surface, strongly supports these ideas.[113] The Rh{331} structure is shown in Fig. 28. The corresponding EARN data and EAM calculations are shown in Fig. 29. The most interesting features of the angular distribution plot are that the ejection is strongly peaked at $\theta = 15°$ along the $\phi = +90°$ azimuth, and that the desorption along other crystallographic directions is considerably reduced. Note that these features are well reproduced by the EAM calculations. The parameters in the potential function were unchanged from those used in the Rh{111} calculation. This agreement is quite important to see since the excess electron density present at the step edge might have altered the trajectory of the departing Rh atoms. These calculations conclusively show that the peak at $\theta = 15°$ arises from the same channeling mechanism operative

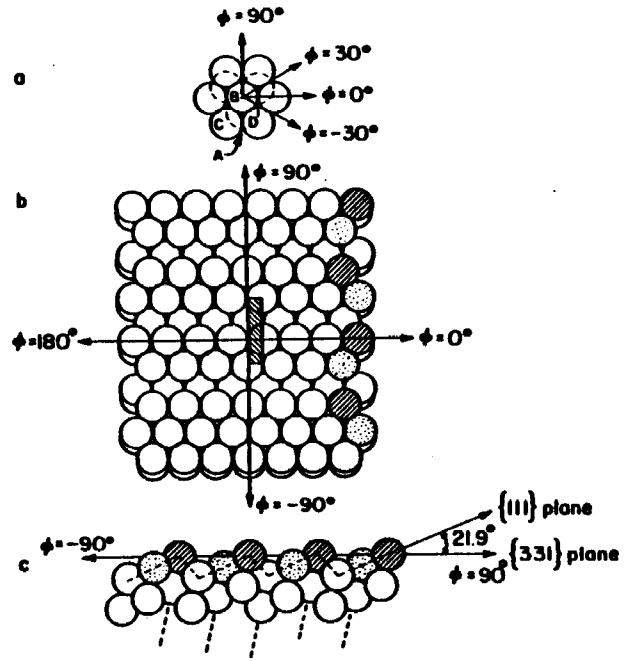

Figure 28. (a) Rh{111} surface indicating azimuthal directions used in the text. The dashed atoms are in the second layer of the crystal. (b) Rh{331} surface indicating the definition of azimuths used in the text. The $\phi = 0°$ azimuth is the same as that in (a). The impact zone used in the classical dynamical simulation is shown at the center of the crystallite as a shaded box. (c) Rh{331} surface viewed from the $\phi = 0°$ direction. The shaded atoms correspond to the shaded atoms in (b). The dotted near-vertical lines indicate a major channeling direction. (From Ref. 113.)

for {111}. This polar angle corresponds to the $\theta = 37°$ peak observed from {111} except that the crystal orientation is simply tilted by 21.9° about $\phi = 0°$ as seen in Fig. 28. The reduced intensity along the other directions arises either from the presence of open channels in the crystal (near $\theta = 0°$) or from blocking due to the atomic step along $\phi = -90°$. Overall, the structure in the angular distributions is quite striking for both clean Rh{111} and Rh{331}, especially when compared to the simple $\cos^2 \theta$ dependence exhibited by the polycrystalline Rh surface.

Since crystal structure via channeling and blocking strongly influences the EARN distributions, it follows that adsorbate atoms or molecules on single-crystal substrates should systematically alter the trajectories of the desorbing underlayer species. This concept has been tested in detail for the $p(2 \times 2)$ O ordered overlayer on Rh{111} with

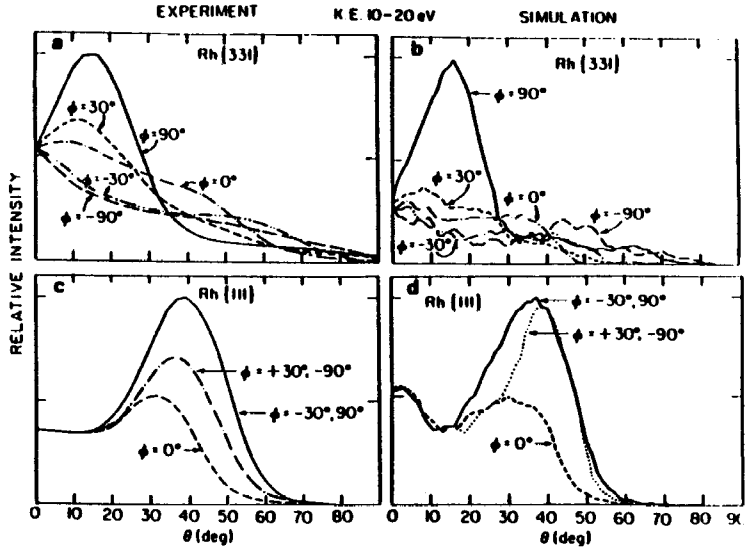

Figure 29. Polar angle Rh atom distributions of keV ion-induced desorption from Rh single crystals. The 10–20-eV kinetic energy range is shown. (a) Rh{331}, experimental data; (c) Rh{111}, experimental data; (b,d) calculated curves employing the EAM potential. (From Ref. 113.)

the EARN experiment.[67] For an atomic adsorbate of this sort, there are a number of possible high-symmetry binding sites including two different three-fold hollow sites (often referred to as the B or fcc site and the C or hcp site) and an on-top site (or A site) (Fig. 12). The simplest idea is that adsorption of oxygen atoms at a B site should preferentially block Rh atoms desorbing along the $\phi = +30°$ azimuth, adsorption at a C site should alter the path of Rh atoms leaving along $\phi = -30°$, while A site adsorption may have very little effect, except perhaps on the particles emitted at $\theta = 0°$. Preliminary polar angle measurements[45] as seen in Fig. 27 clearly show that the $\phi = -30°$ direction is preferentially reduced relative to either $\theta = 0$ or $\phi = +30°$, strongly suggesting C site adsorption.

These results are quite interesting since they clearly show how sensitive the desorption angular distributions are to small overlayer coverages. In this case, in addition to the observed perturbations in the EARN distributions, the total ground state neutral Rh atom yield was observed to decrease by a factor of about 2. These observations further illustrate that trajectory measurements that are to be compared with

theory must be performed on well-cleaned and chracterized surfaces *and* under low-dose conditions.

It would be gratifying to obtain the same excellent agreement between the $p(2 \times 2)$ O/Rh{111} EARN measurements and the EAM-molecular dynamics calculations as was found for the clean surface. The development of the EAM is not yet directly applicable, however, to chemisorbed overlayers such as oxygen. As an approximation, it has been possible to take a fairly rigorous look at overlayer effects by using EAM forces to describe the Rh–Rh interactions, but using pairwise additive potentials to describe the Rh–O surface interactions. These simulations clearly confirm that the simple blocking ideas are correct, and yield EARN distributions for the Rh atoms that are in quite good agreement with experiment.[67]

Usually, as pointed out in Section 3.1, kinetic energy distributions of ejecting atoms are not terribly relevant to studies involving surface structure. There is a situation associated with chemisorbed species, however, that merits closer attention. The KE distributions for clean Rh{111} and oxygen covered Rh{111} are shown in Fig. 30.[67] Note that the peak in the KE spectra shifts by 2–5 eV to *lower* KE. The computer simulations suggest that this lowering arises from the fact that the underlying Rh atoms lose some energy as they escape through the overlayer oxygen atoms. The effect might be misinterpreted to mean that oxygen decreases the Rh surface binding energy since analytical models predict that the peak is proportional to 1/2 of this value. The effect is even more clearly noticeable when benzene is adsorbed on Rh{111} as seen in Fig. 31.[175] Notice that the benzene overlayer is dramatically reducing the intensity of the highest-energy Rh atoms and is shifting the peak energy to lower values. These types of experiments may eventually prove valuable in following the flow of energy between the substrate and surface molecules as they are coaxed to desorb intact from the surface.

5.1.2. *Trajectories of Overlayer Species*

If channeling and blocking are important desorption mechanisms for substrate atoms, even more dramatic effects should be visible for the overlayer species themselves. To date, EARN experiments have not yet yielded significant information aimed toward this problem. This lack of progress arises, in part, as a result of the difficulty of ionizing typical adsorbate species such as oxygen, hydrogen, sulfur, or carbon layers. It has been possible, however, to obtain this information on the desorbing secondary ions. Although it is dangerous to directly compare these data with computer simulations, every experiment to date suggests that at

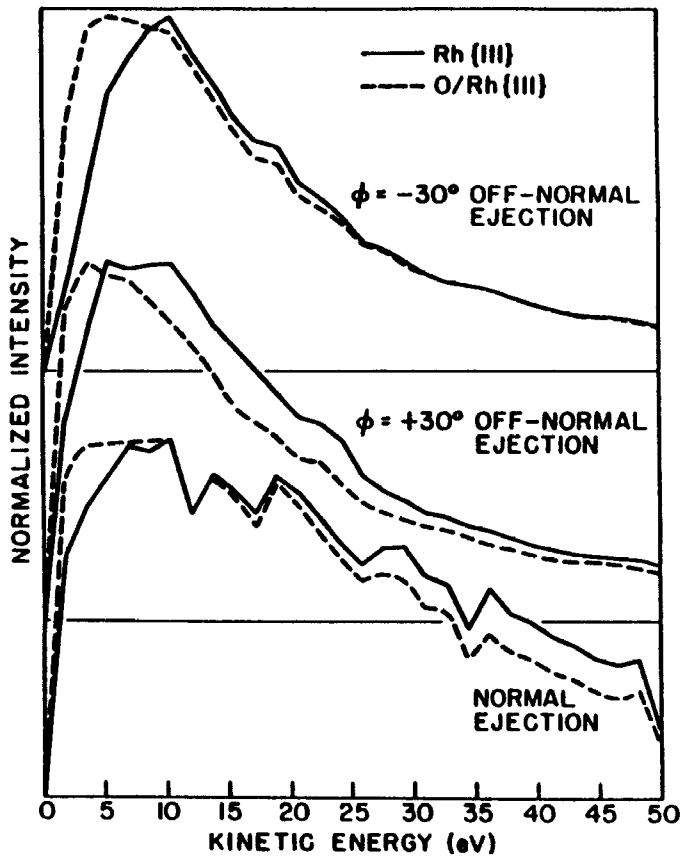

Figure 30. Experimental kinetic energy distributions of Rh atoms ejected from clean and oxygen-covered Rh{111}, taken at ejection angle $\theta = 45°$. $p(2 \times 2)$ LEED pattern was observed for the oxygen overlayer. The data are normalized to the same peak signal intensity. The polar angle resolution is ±3°. (From Ref. 67.)

least in a qualitative sense, channeling and blocking are also applicable to understand secondary ion distributions.

The first studies of this sort were reported for oxygen adsorbed on Cu{100}.[176] For this example, a quadrupole mass spectrometer was positioned to detect either Cu^+ or O^- ions ejected at a polar angle of $\theta = 45°$. The Cu crystal was exposed to 1200 L (Langmuirs) of oxygen at 300 K to yield a $c(2 \times 2)$ oxygen overlayer. The measured intensity for both Cu^+ and O^- ions as the crystal was rotated through 360° is shown in Fig. 32. Note that the Cu^+ ion yield maximizes along $\phi = 0°$, 90°, 180°

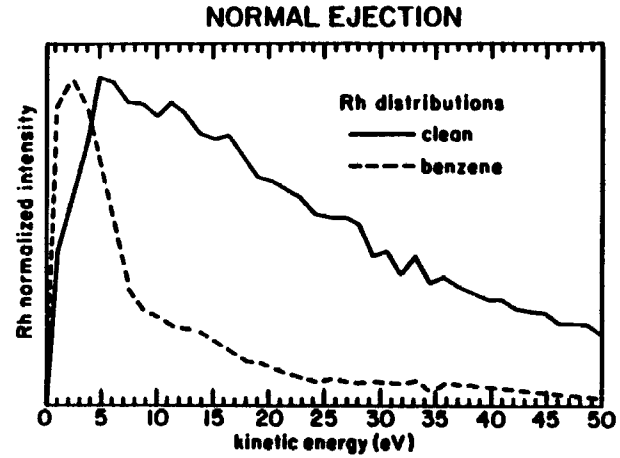

Figure 31. Experimental angle-integrated kinetic energy distribution for Rh atoms ejected from Rh{111} for a clean surface and a surface covered with approximately 1 monolayer of benzene. The sample was bombarded by 3-keV Ar^+ ions at normal incidence. (From Ref. 175.)

and 270°, corresponding to the open crystallographic directions. The $\phi = 0°$ direction is equivalent to ⟨001⟩. As has been shown for the EARN experiments for Rh{111}, the surface channels the desorbing Cu atoms specifically in these directions. The Cu^+ ion yield is a minimum along $\phi = 45°$, 135°, 225°, and 315° owing to blocking along the close-packed row. The $\phi = 45°$ direction is equivalent to ⟨011⟩.

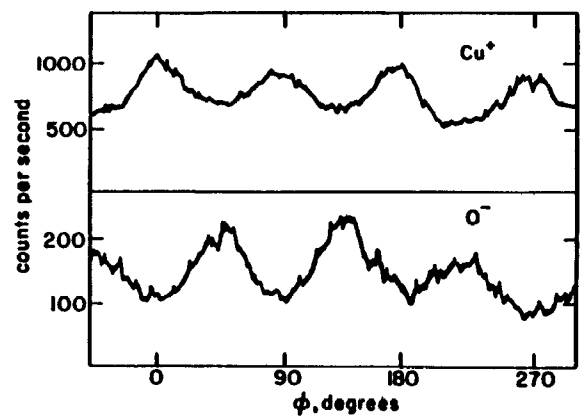

Figure 32. The Cu^+ and O^- azimuthal plots for $c(2 \times 2)$—O/Cu{100}. The sample was bombarded with 1500 eV Ar^+ ions at normal incidence. (from Ref. 176.)

Using this simple concept, it is possible to understand the azimuthal behavior of the O^- ion yield. For adsorption in the four-fold hollow site, oxygen is channeled in a direction rotated by 45° from the Cu substrate. It experiences blocking, however, in the $\phi = 0°$ direction. For adsorption in the A-top site, the oxygen azimuthal direction would be expected to match that of the substrate since the oxygen angular distributions would be controlled mainly by the desorbing substrate species. As is seen from Fig. 32, the results strongly support the assignment of the adsorbed oxygen atom to the four-fold hollow site. There are a number of complications associated with this simple interpretation. First, the magnitude of the azimuthal anisotropies is dependent upon the kinetic energy of the desorbing ion. For the very low-energy particles, there has been sufficient damage to the crystal structure near the impact point of the primary ion that the channeling mechanisms are no longer operative. On the other hand, at higher kinetic energies, say greater than 10 eV, the desorbing ion leaves the surface early in the collision cascade while there is still considerable order in the crystal. The channeling mechanisms are much stronger and the angular anisotropies are larger.

A second complication involves the determination of the height of the adsorbate atom above the surface plane. Calculations have been performed using pair potentials where this bond distance has been varied over several angstroms in order to find the best fit with experiment.[176] These studies have also shown that the polar angle distribution is sensitive to the effective size of the adsorbed atom. Thus, it is important to know more about the scattering potential parameters if this distance is to be determined accurately.

Early attempts at quantitatively calculating the O–Cu bond length were apparently unsuccessful, perhaps owing to the complexity of this system. Angle-resolved photoemission experiments indicated that although the bonding was indeed occurring in the four-fold hole site, at least a portion of the oxygen atoms were found directly in the plane of the Cu{100} surface.[177] Nevertheless, the channeling and blocking ideas were established as important for desorbing ions as well as neutral species. Apparently, effects such as azimuthally dependent ionization probabilities and bending forces such as the image force are not strong enough to mask these dominant factors, particularly if only the high-kinetic-energy ions are detected.

A second example of the importance of channeling and blocking has more recently been developed for the case of Cl adsorbed on various crystal faces of Ag. The azimuthal distributions for Cl^- ejected from Ag{110} covered with various amounts of Cl atoms are shown in Fig. 33.[178] As for oxygen on Cu, the ions were detected at $\theta = 45°$, and only

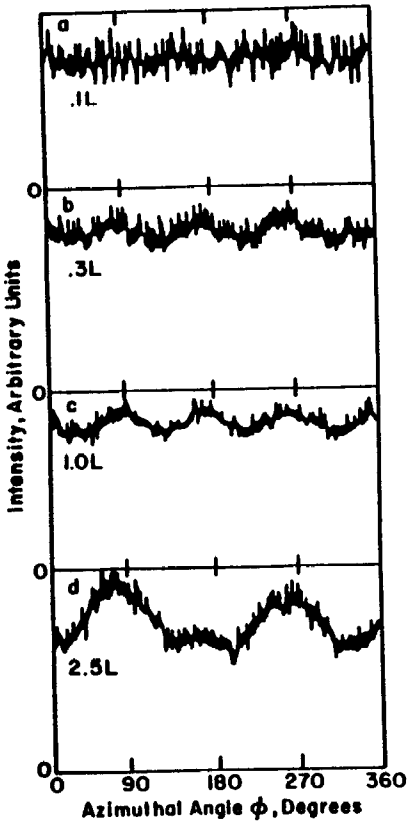

Figure 33. Azimuthal angle distributions of high-energy (18–22 eV) secondary Cl^- ions as a function of Cl_2 exposure. In our notation, $\phi = 0°$ and $\phi = 90°$ correspond to the ⟨001⟩ and ⟨110⟩ directions, respectively. The Ar^+ ion is incident at $\theta = 0°$ and the particles are collected at $\theta = 45°$ (From Ref. 178.)

those ions with high kinetic energy were recorded. For this case, it was found for values of $\theta < 45°$ that Cl–Cl scattering in the overlayer itself is the dominating mechanism for Cl^- desorption. As seen from the plots, rotation of the Cl-covered Ag{110} crystal about 360° yields systematic signal variations. The magnitude of the anisotropy increases from near zero after only 0.1 L exposure, but increases to about 12% of the total signal after 1.0 L exposure. In each case, the position of the peaks occurs along the ⟨001⟩ ($\phi = 0°$) and along the ⟨110⟩ ($\phi = 90°$) azimuthal directions. Channeling and blocking concepts lead to a straightforward assignment of the adsorption site of the Cl surface atom. At the lowest coverage point, it is proposed that the Cl atom is quite large in size and therefore resides above the trough of the {110} surface as seen in Fig. 34. At this position, it would not experience significant channeling by the substrate atoms. At higher coverages, however, it is proposed that the adsorbed Cl atom becomes significantly smaller owing

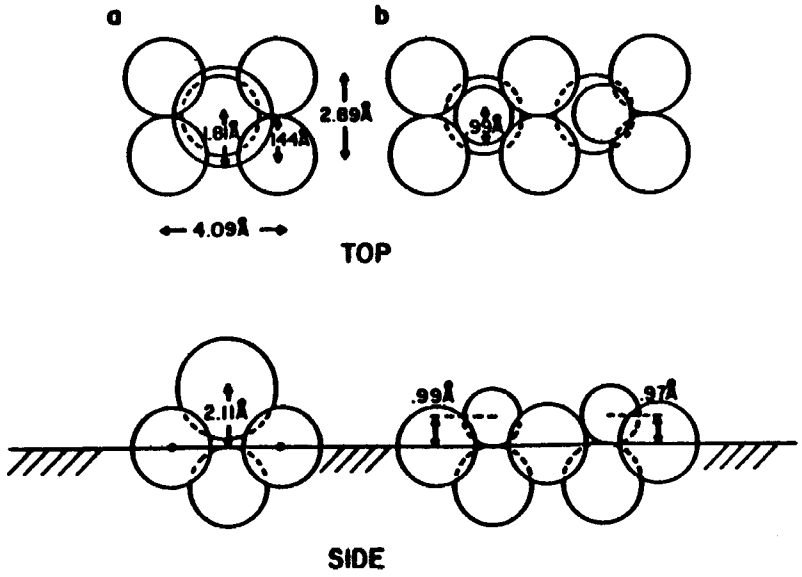

Figure 34. Possible bonding geometries of differently charged Cl. (a) Fully charged Cl^- adatoms and (b) atomic Cl. Note that the surface plane is defined by the nuclear centers of the topmost Ag atoms. In addition, note that there is a possible asymmetric bonding site in (b) which allows the Cl atom to approach to within 0.97 Å of the surface plane. (From Ref. 178.)

to the presence of dipole–dipole interactions between neighboring adsorbate atoms. As it shrinks, it literally falls into the valley of the {110} substrate and can experience channeling either along the valley direction ($\phi = 90°$ or 270°) or perpendicular to the valley ($\phi = 0°$ or 180°). In this latter case, the Cl^- ion is channeled by two Ag atoms comprising the valley wall. Thus, the adsorption site is defined as a four-fold bridge site with the Cl atom binding directly over a Ag atom in the second layer. Note that at the highest Cl coverage corresponding to an exposure of 2.5 L, the desorbing ion can more easily escape along the direction of the valley, yielding a two-fold symmetric azimuthal angle scan. As we shall see in the next section, these simple observations are entirely consistent with ion scattering studies of this system.

It will be quite interesting to examine the influence of the polar angle on the simple nature of these azimuthal scans. Very little research has yet been completed in the area, but some fascinating data for Cl on Ag{100} are available. This system is quite complicated and many different models have been proposed for the structure of the overlayer. The representation of the simple overlayer model (SOM)[179–181] and the mixed

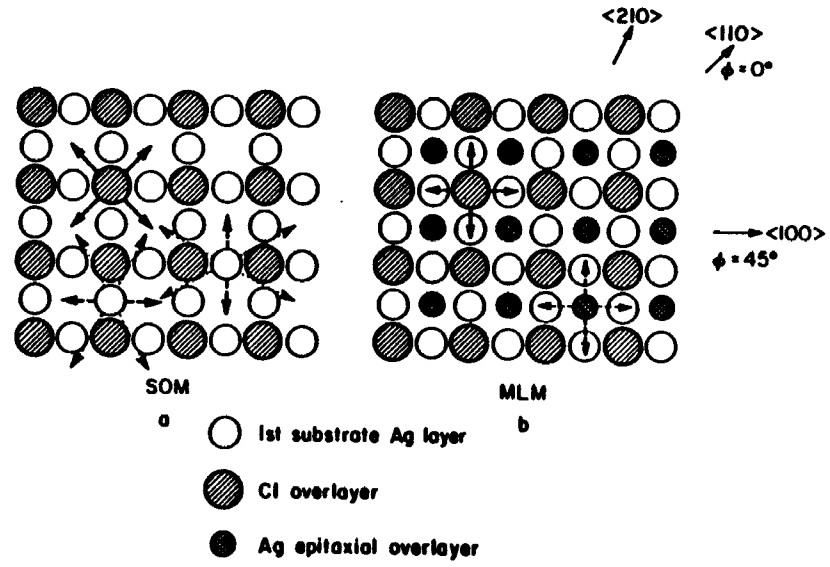

Figure 35. Schematic picture of two $c(2 \times 2)$ structures of Cl on the Ag{100} surface. (a) Simple overlayer model (SOM). (b) Mixed layer model (MLM).

layer model (MLM)[182] are shown in Fig. 35. The LEED data indicate that after 5.0 L exposure to Cl a $c(2 \times 2)$ structure is observed.[179] The angle-resolved SIMS experiments shown in Fig. 36 support the idea that the Cl adsorbates bond in the C_4 symmetry sites.[183] Minimum ion intensities are observed along ⟨110⟩ azimuths, which correspond to the direction of close-packed rows of atoms in the surface plane. Particles ejected along these directions are obstructed at small values of θ. For $\theta = 45°$ and a Cl exposure of 1.5 L, the maximum ion intensities arise along ⟨100⟩ directions. These peaks result from a strong channeling effect (dashed arrow of Fig. 35) exerted on the ejected Ag^+ ions by the nearest-neighbor Ag atoms and/or by the adsorbed Cl atoms. At large values of θ, however, the departing Ag^+ ion is scattered by the Cl adsorbate, resulting in the complex azimuthal pattern seen in Fig. 36 and explained by the diagram in Fig. 35a.

Channeling and blocking are not only observed when atomic adsorbates are found to a surface, but also are seen in the presence of molecular adsorbates. Polar angle distributions of benzene and pyridine ions ejected from ion-bombarded Ag{111} exhibit features that indicate that a vertical channeling process is occurring.[184,185] For a Ag surface covered with a monolayer of benzene or exposed to 0.15 liter of

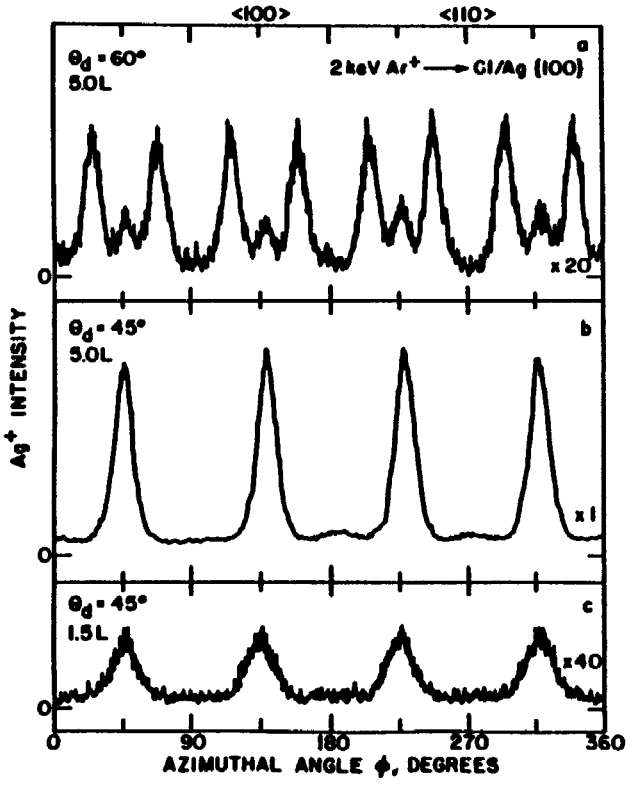

Figure 36. Azimuthal angular distributions of high-energy (20 ± 3 eV) Ag^+ secondary ions from a Ag{100} surface after exposure to (a and b) 5.0 L of chlorine, and to (c) 1.5 L of chlorine. The Ar^+ ion of 2 keV is incident normal to the surface and the particles are collected at (a) $\theta_d = 60°$ and (b and c) $\theta_d = 45°$, respectively. The angles are defined in Fig. 38. (From Ref. 183.)

pyridine, the molecules are believed to be lying parallel to the surface in a π-bonding configuration. The polar angle distributions of $(M - H)^+$ ions ($C_6H_5^+$ for benzene) and $(M + H)^+$ ions for pyridine are broad and exhibit a peak at $\theta = 20°$ as shown in Fig. 37. At high exposures of pyridine, however, the polar angle distribution is sharper and peaks at $\theta = 10°$. This result suggests that at higher coverages, the pyridine molecules are forced into a vertical σ-bonding configuration through the N atom lone pair. This bonding configuration allows more molecules to interact with the surface. This σ-bonded interaction is, of course, not possible with benzene and the polar angle distribution is invariant with

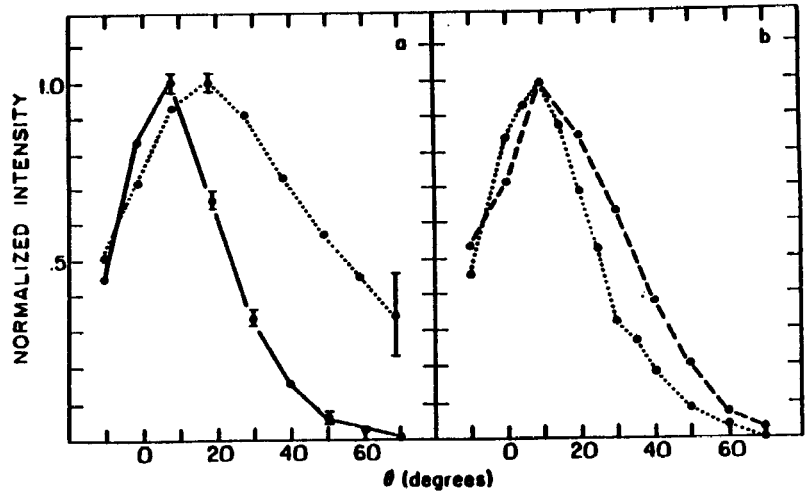

Figure 37. Normalized polar angle distributions of molecular ions ejected from overlayers of organic molecules adsorbed on Ag{111} at 153 K. The polar angle is defined with respect to the surface normal. (a) —, 4.5 L pyridine $(M + H)^+$; ···, 2.5 L benzene $(M - H)^+$. (b) 4.5 L pyridine $(M + H)^+$; – – –, 6–10 eV secondary ions; ···, 3–7 eV secondary ions. (From Ref. 185.)

coverage. The vertical array of pyridine molecules acts as a channel for directing the desorbing pyridine molecules in a direction close to the normal. It is interesting that a wide range of other surface spectroscopies including electron energy loss[186] and EXAFS methods[187] confirm that these bonding changes are, in fact, occurring in pyridine. In addition, classical dynamics calculations for this molecular desorption system reveal that such channeling mechanisms are quite commonly found.[183]

In summary then, angular distributions contain much detailed information about single-crystal surface structures which are, in fact, quite difficult to extract using other techniques. The symmetry of azimuthal scans can yield straightforward site determinations using desorbing substrate atoms or ions or using desorbing overlayer ions. As discussed in earlier sections, it has been possible in some cases to obtain quantitative agreement between calculated and measured angular distributions. In many other instances, however, the qualitative features of the angular distributions add a powerful approach to examining the bonding configuration of surface species. The next step, of course, is to see if these ion-bombardment methods could be used to obtain accurate bond-length measurements.

5.1.3. Shadow-Cone Enhanced Desorption

It has recently been discovered that the desorption yield of all particles is enhanced when the shadow cone created by a surface atom intersects a nearby atom.[188] The shapes of these shadow cones are quite well characterized since they have been utilized in Rutherford backscattering[189] and impact-collision ion scattering[190] experiments for many years. For ion-bombardment experiments, we take advantage of the fact that the flux of incident particles along the edge of the shadow cone is large. With knowledge of the angle of incidence of the primary beam, it is then feasible to determine surface bonding configurations using a strategy similar to that developed for ion scattering.

The basic experimental scheme and angle definitions are shown in Fig. 38. In principle the detector should be configured to collect all desorbing ions, regardless of their kinetic energy or angle. Most experiments to date, however, have been performed with a fixed angle β and with a detector set to collect only the high-kinetic-energy particles. With this configuration, the shadow-cone enhanced desorption concepts may be more carefully evaluated.

Representative results for Ag{110} are shown in Fig. 39.[191] There are two major features in these distributions which correspond to the

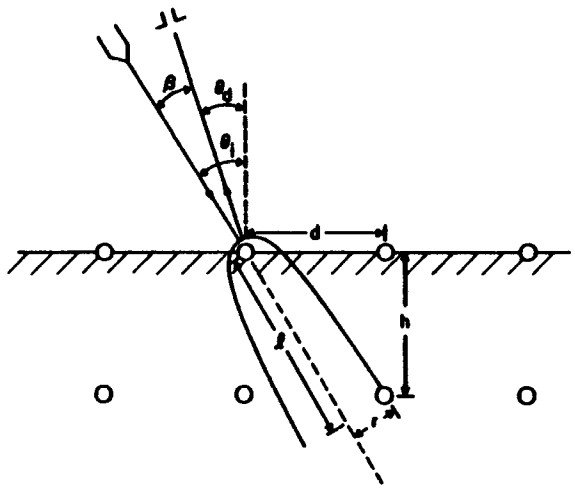

Figure 38. Parameter definitions for the shadow-cone-enhanced desorption experiment. The ion beam is incident at θ_i, the desorbed particles are detected at θ_d and $\beta = \theta_i - \theta_d$. The shadow cone is described by a radius r at a distance l behind the target atom. The d and h values describe the surface bond lengths.

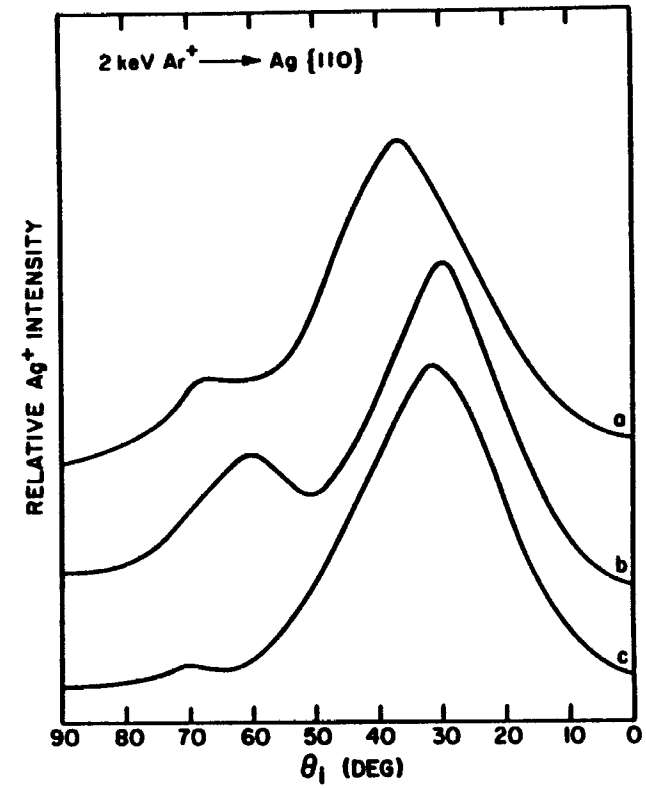

Figure 39. The shadow-cone enhanced SIMS spectra of the desorbed Ag^+-ion yield as a function of the angle of incidence. The particles are collected along the (a) ⟨100⟩, (b) ⟨110⟩, and (c) ⟨211⟩ azimuth during 2-keV Ar^+-ion bombardment at a current of ~5 nA. Only particles desorbed in plane with $\beta = 25°$ are collected. (From Ref. 191.)

intersection of the shadow-cone with a second-layer atom ($\theta \sim 35°$) and with a first-layer atom ($\theta \sim 70°$). The fact that these peak maxima actually correspond to the intersection of a shadow-cone edge with a substrate atom has been tested by using a full three-dimensional computer simulation like that discussed in Section 3. The position of this peak has been shown to be unaffected by the image interaction or other forces related to the secondary ionization process since the peak position is found to be independent of β for θ_d values between 0° and 45°. From the position of the peaks, it is possible to calculate d using a Molière potential and to compare this calculated value to the known interatomic spacing for Ag. The results compare to within ±0.5°, yielding an uncertainty of about ±0.06 Å in the bond length. Similar procedures for

determining h suggest that the spacing between the first and second layer is relaxed by (7.8 ± 2.5)% and the spacing between the first and third layer is relaxed by (4.1 ± 2.1)% relative to the bulk spacing. These values agree within the same error limits with those bond lengths found by Rutherford backscattering measurements.[192]

Adsorbate atoms will also create shadow cones that can intersect nearby substrate atoms, opening the possibility of measuring the bond length of chemisorbed species. An excellent case to test this idea is the chemisorption of Cl on Ag{110} discussed in the previous section. The channeling and blocking experiments suggest that the binding site is invariant over a wide coverage range, allowing the Ag–Cl bond length to be examined under a variety of experimental conditions. The results are shown in Fig. 40.[188,193] Of particular note is that at extremely low Cl coverages, the observed bond length is extended over that observed in the high coverage limit by nearly 0.4 Å. This change in length, accompanied by a change in the shape of the Auger electron emission spectra, has been explained as being due to a shift from highly ionic bonding at

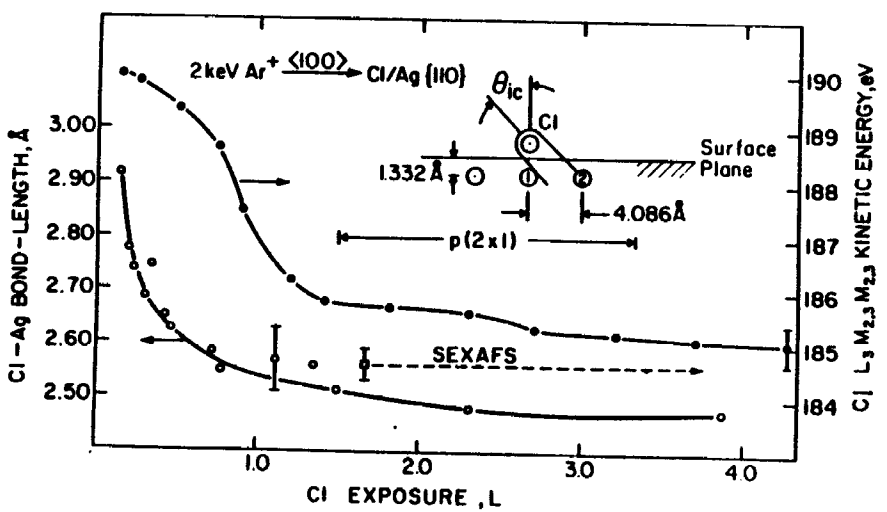

Figure 40. Ag–Cl bond-length change (O) and Auger Cl L_3 $M_{2,3}$ $M_{2,3}$ kinetic energy (•) as a function of Cl_2 exposure at 300 K. The reported value refers to the distance between the center of silver atom 1 and the Cl atom. The $p(2 \times 1)$ LEED pattern was observed in the exposure region as shown. The bond lengths from the SEXAFS experiments are associated with the LEED pattern; the same value was also obtained at a coverage beyond 4 L and associated with the $c(4 \times 2)$ LEED pattern. The shadow-cone induced desorption mechanism used to calculate the bond length is shown in the inset. The interplanar spacing refers to the relaxed clean-surface Ag{110} value. The shadow-cone shape was calculated using a Thomas–Fermi–Molière potential with a scaling factor of 0.86. (From Ref. 193.)

low coverage to more covalent bonding at high coverage. If the Ag–Cl interaction is highly ionic, the bond should have a significant dipole moment. Presumably dipole–dipole interactions between nearby Cl^- atoms force charge back into the Ag substrate. The absolute value of the bond length at high exposures agrees quite well with surface-EXAFS experiments obtained from the $p(2 \times 1)$ ordered overlayer as seen in Fig. 40.[194] The results are also consistent with the channeling and blocking experiments discussed previously, which suggest that the Cl adsorbate could more closely approach the surface at higher coverages.

These types of surface structure determinations may be extended to more complex systems provided that several different shadow-cone intersections can be found without being influenced by distortion effects. Materials such as GaAs and Si representing interesting test solids since their lattice spacings are generally large relative to the shadow-cone radius. One example has been reported using GaAs{110}.[195] In this case, the As surface atoms are forced up from their bulk-terminated lattice positions. Since lateral displacements are also possible, any given peak in the desorption yield would correspond to a large number of possible lattice positions. This degeneracy may be resolved by tracing out the locus of points associated with each desorption mechanism and then searching for intersections of the resulting lines using several different desorption mechanisms. For GaAs{110}, for example, nearly 40 different features could be discerned from the various polar angle distributions. The location of the surface Ga and As atoms relative to the second layer positions could then be uniquely determined as seen from Fig. 41. The positions are in quite good agreement with extensive LEED calculations performed over the last 15 years or so.

The fact that these simple angular distributions provide such microscopic information about surface structure is really remarkable from several points of view. Certainly, the primary beam is creating lots of damage to the surface, and yet it seems possible to obtain accurate surface bond lengths. The experimental configuration is exceedingly straightforward, requiring only a simple ion source, quadrupole mass filter and polar angle rotation capabilities for the sample holder. The potential sensitivity of this approach to low concentrations of overlayers is indeed unprecedented. The three examples presented in this review are very promising ones, but much research remains in this area. It will be interesting to examine how the distributions change with shadow-cone radius and whether it will be possible to enhance certain desorption mechanisms by changing particle mass and energy. In any case, it is clear that angular distributions tell us a great deal about the ion-impact event in particular and provide detailed surface structural information in

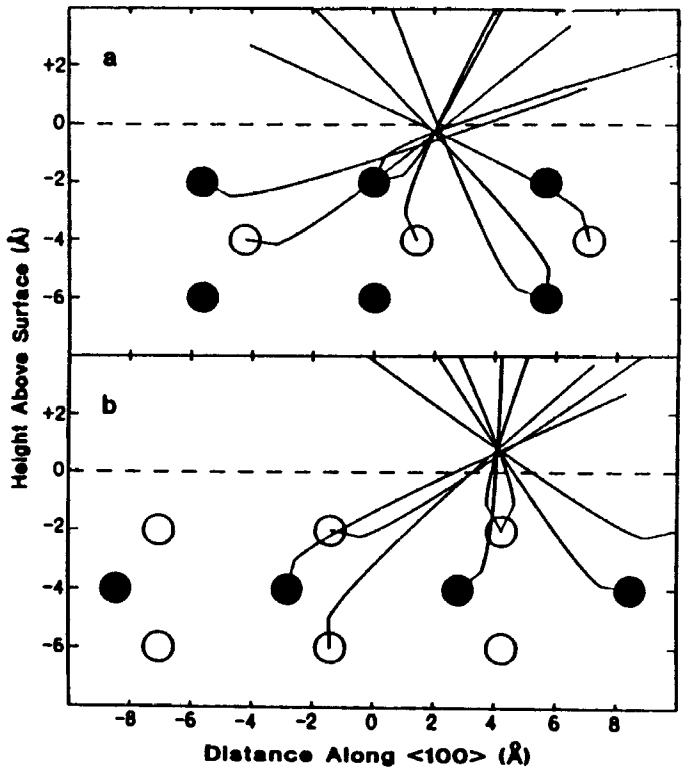

Figure 41. Cross section of GaAs{110} with Ga O and As ● atoms delineated. The top row of atoms has been removed. Panel (a) is the Ga terminated plane of atoms while Panel (b) shows the As terminated plane. Each curve represents the calculated set of surface atom positions that can result in an experimentally observed interaction. The region of the crossing of these curves represents the experimentally determined Ga(As) surface atom position. (From Ref. 195.)

general. We have concentrated so far on the desorption of atomic species. It is next of interest to see if these ion-beam techniques are useful in surface chemical applications by detection of desorbed molecular components of the top layer of the sample.

5.2. Molecular Composition Studies

There has been intense interest in measuring the mass of molecular cluster ions ejected from ion bombarded materials. These experiments can be important for the compositional analysis of solids and surfaces if

these clusters can be shown to reflect in some fashion the original make-up of the sample. It is clear from the study of a vast array of species that it is possible to desorb molecules intact with high efficiency. This observation has led to the birth of the whole field of high-molecular-weight mass spectrometry. The use of this technique for protein sequencing is now widespread. It is ironic that most of the molecules that desorb intact would decompose during thermally induced desorption.

As we have discussed in Section 3.2, the theory of molecular desorption is rather complex, suggesting that a detailed interpretation of SIMS spectra may be difficult. The molecular dynamics simulations tell us, for example, that recombination of surface atoms to form new molecules is highly probable when the solid itself does not possess a specific molecular identity as for clean metals or metals covered with a chemisorbed oxide overlayer. When the intramolecular forces are particularly strong, however, the molecule can soak up energy from the collision cascade and desorb intact. In this case, in fact, the simulations suggest that the larger the molecule, the less fragmentation will be observed. Finally, it appears that desorbing molecules can recombine with other desorbing ions to create new cationized molecules. This scheme has been used to increase the number of molecular ions relative to the number of neutral species.

Now to the point of this discussion: It is clear that the desorbed molecules in some way reflect the surface composition. In many experimental situations, this result can provide powerful surface chemical information. In other situations, however, recombination in various forms may lead to faulty data interpretation. At this point, it is not possible to quantitatively predict which mechanism of cluster formation will dominate unless all of the bond energies for the system are well known. It is imperative, then, to devise additional experimental approaches to maximize the information content contained within the mass spectra of these desorbed molecules.

5.2.1. Intact Molecular Ejection

Perhaps the least complicated system from a chemical viewpoint is the chemisorption of hydrogen on solid surfaces. In general, however, hydrogen is quite difficult to detect experimentally and is known to bind to surfaces in many atomic or molecular states. For example, three distinct hydride phases (mono-, di-, and trihydride) have been found on the important Si(111)-(7 × 7) surface, and the elucidation of their properties is important in Si etching technology. Ion beam techniques are particularly powerful for this system. Several SIMS spectra recorded at different deuterium adsorption temperatures are shown in Fig. 42. Note

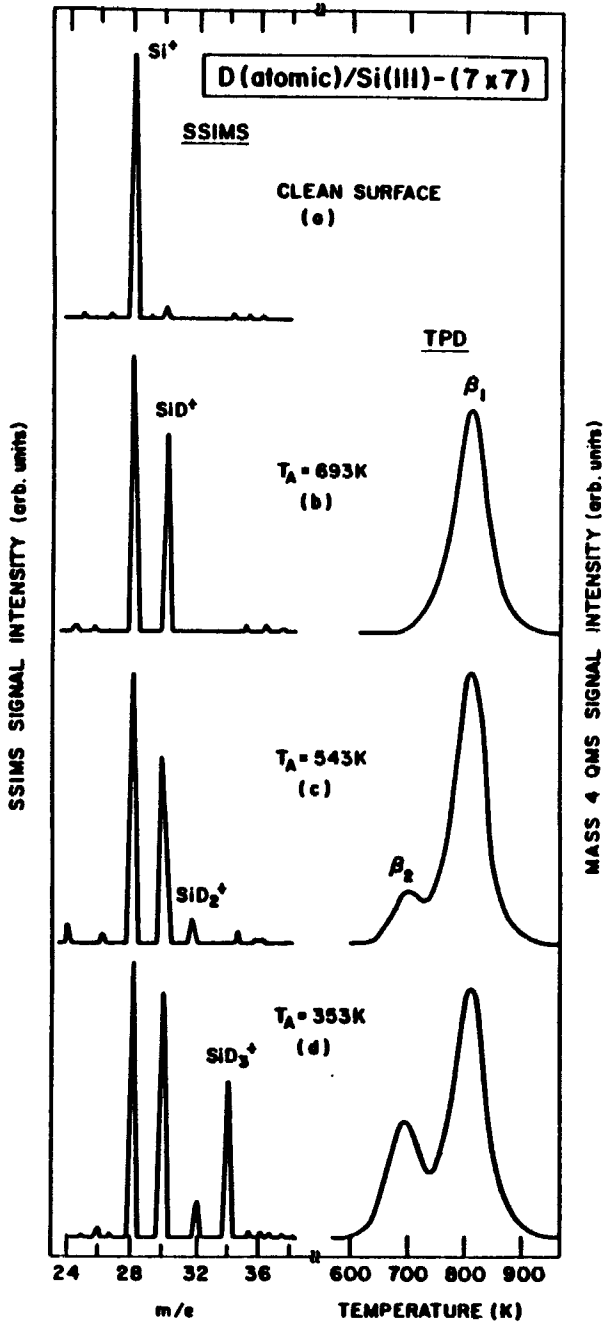

Figure 42. (a) SIMS (left side) spectrum for a clean Si(111) – (7 × 7) surface. TPD (right side) and SIMS (left side) spectra for a deuterium-saturated Si(111) – (7 × 7) surface. The adsorption temperatures are (b) 693 K, (c) 543 K, and (d) 353 K.

that at $T_A = 693$ K that the SiD^+ signal correlates well with the single β, thermal desorption peak.[196] At lower adsorption temperatures, SiD_2^+ and SiD_3^+ ions are observed which also correlate with thermal desorption features. From these data and from the known total D coverage, it has been possible to assign each of these cluster ions to the respective hydride phase and to quantify the coverage of each phase as a function of temperature. In this instance, then, apparently recombination and ion beam induced fragmentation of the cluster ion are not significant and the hydrides are being ejected from the surface intact.

If it is possible to desorb hydrides intact, it becomes of interest to examine a series of surface molecules consisting of just a few C—H units such as CH_x and $CH_2{=}CH_2$ species. A difficult case involves the commercially relevant methanation reaction via the Fischer–Tropsch process as

$$CO + 3H_2 \xrightarrow[Ni]{450\ K} CH_4 + H_2O \qquad (28)$$

In the production of CH_4, the C—O and H—H bonds must clearly be broken, but what sort of reaction intermediates are possible in the process? In a series of experiments, CO and H_2 were allowed to react over Ni{111} at peassures near 100 Torr until CH_4 could be detected by gas chromatography.[197] The crystal was then rapidly transferred into a SIMS system for analysis. Room temperature SIMS spectra are shown in Fig. 43. Note that each CH_x fragment ion is observed directly and attached to a substrate Ni atom. It was hypothesized that these reaction intermediates were indeed present on the surface since the intensity of each cluster ion decreased at a different rate as the substrate temperature was raised. If the surface concentrations of the CH_x intermediates are similar even to within an order of magnitude, a mechanism involving sequential hydrogenation of surface carbon seems most reasonable.

As the size of the adsorbate molecule increases, the SIMS spectra do get considerably more complicated. The spectrum of a condensed layer of CH_3OH on Pd{111} at 110 K is shown in Fig. 44.[198] This spectrum is characterized by a strong CH_3^+ signal, a CH_2OH^+ ion peak and a series of $(CH_3OH)_nH^+$ and $Pd(CH_3OH)_nH^+$ cluster ions. Protonation of the molecular ion is commonly observed with organic SIMS.

The presence of CH_3^+ (and the lack of CH_2^+, CH^+ or C^+ ions) is quite interesting in that it is the only CH_x fragment ion observed. Similar behavior has been reported for the adsorption of $CH_2{=}CH_2$ on Pt{111} by White and co-workers.[199] In this cae the $CH_2{=}CH_2$ converts at room temperature to ethylidyne ($\equiv C{-}CH_3$), where a carbon atom is bound directly to the metal surface and the CH_3 functionality is pointing

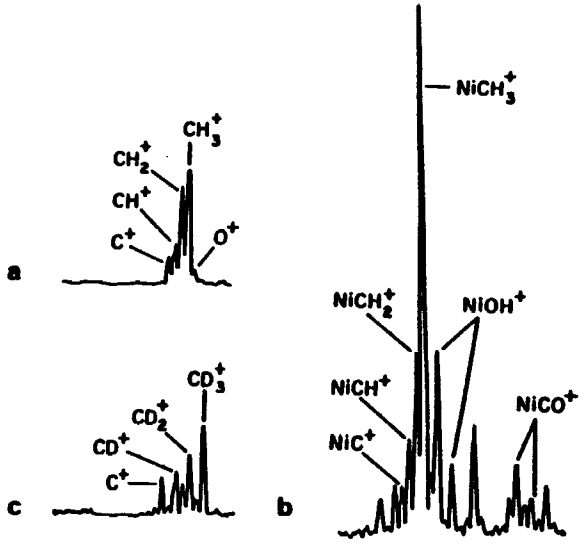

Figure 43. SIMS spectra of (a) low mass region, (b) Ni^+ region after $CO + H_2$ methanation, and (c) low mass region after $CO + D_2$ methanation (from Ref. 197).

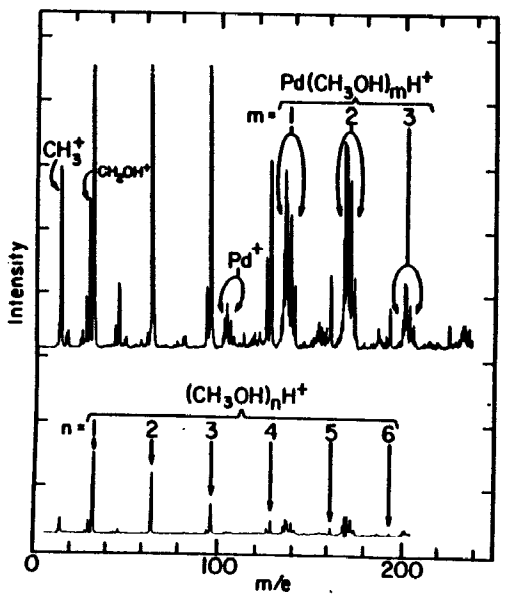

Figure 44. Positive ion SIMS spectra for Pd{111} exposed to 6 L CH_3OH at 110 K. The spectra were recorded using a 3-keV Ar^+ primary ion beam with a current density of 0.4 nA cm^{-2}. The top spectrum is shown with a 10× magnification. (From Ref. 198.)

upward. These workers found that CH_2^+ was the most intense peak at 200 K, but that the CH_3^+ ion dominated at 300 K, consistent with $\equiv C-CH_3$ formation from $CH_2{=}CH_2$.

If the CH_3^+ SIMS ion is a useful tag in hydrocarbon decomposition, it would be of interest to follow the decomposition of molecularly adsorbed CH_3OH as the temperature is raised. For this experiment, the SIMS ion signal as a function of temperature, combined with XPS measurements, yield a definitive picture of the decomposition pathway. When the temperature reaches 120 K, all cluster ion intensities begin to decrease as CH_3OH desorbs from the surface.[200] By 175 K, however, the CH_3^+ signal increases. The XPS experiments suggest that at this temperature, the CH_3OH decomposes to CH_3O_{ads} plus a hydrocarbon fragment of unknown composition. Since no CH_3^+ ion signal is seen from pure layers of CH_3O_{ads}, it was concluded that the rise in the CH_3^+ ion signal is due to the formation of a surface methyl intermediate, CH_{3ads}. The initial decomposition pathway, then, is

$$2CH_3OH \rightarrow CH_{3ads} + CH_3O_{ads} + H_2O_{ads} \qquad (29)$$

Similar results have been obtained on Pt{111} surfaces.[201] These results are particularly important since they illustrate how multicomponent surfaces may be followed with SIMS and that methyl fragments can be desorbed intact. This species may be quite important catalytically, and not many techniques are sensitive to its presence.

Similar important diagnostic surface chemical information has been found for ketene (CH_2CO) adsorbed onto Ru{111}.[202,203] In this case, at 105 K and at low exposures, the adsorption is largely dissociative. The dominant SIMS ion is found at $m/e = 14$ (CH_2^+) and the ions associated with molecular ketene ($m/e = 42$ and 43) are the smallest. At higher exposures where molecular adsorption dominates, the ion yields of $m/e = 15$ and 43 increase abruptly while those of $m/e = 14$ and 42 increase only slowly. With its sensitivity to hydrogen, these types of SIMS measurements promise to yield important new mechanistic data regarding hydrocarbon surface chemistry, particularly C_1 chemistry. This research area appears to be a rich one for the near term, since theory and experiment are in an advanced state of development.

As the adsorbed molecules get heavier, the surface chemistry becomes more complex, but still directly amenable to SIMS studies. The simplest system is CO adsorption on metal surfaces. This molecule is an especially important model compound since computer simulations have been performed for CO desorption, CO generally enhances positive ion yields by several orders of magnitude, and it has a strong intramolecular bond making recombination unlikely. The computer simulations suggest

that only a small fraction of the molecules are dissociated by the incident beam and that nearly all of the CO is ejected intact. This aspect of the problem has been quite conclusively demonstrated by Lauderback and Delgass.[204] Using isotopically labeled equal amounts of ^{13}CO and $C^{18}O$, no isotope mixing was found for the observed Ru–CO^+ cluster ions.

With this information, it is possible to employ SIMS cluster ions to determine whether CO adsorbs molecularly or dissociatively. Dissociative adsorption to carbon and oxygen atoms is, of course, an important preliminary step for promotion of the reactivity of CO on surfaces to build more complicated molecules. An interesting example involves the interaction of CO with the same Rh{111} and Rh{331} crystal planes discussed previously.[205] Does the presence of the atomic step enhance the dissociation probability of the CO molecule? This question has been debated for a number of years in the catalysis literature. The SIMS experiments, along with concomitant XPS measurements, clearly show that under low-pressure conditions, CO remains intact on both surfaces at room temperature. The $RhCO^+$ and Rh_2CO^+ ions are the only significant molecular cluster ions. They presumably form via a recombination mechanism involving Rh and CO species.

The NO molecule has a bond strength that is only ~75% of that of CO. Since it is still a tightly bound diatomic molecule, the classical dynamics models would certainly predict that NO should eject intact if it existed in its molecular state on the surface. The SIMS spectra of NO on Rh{111} at 300 K are shown in Fig. 45.[205] Note that although the $RhNO^+$ ion and Rh_2NO^+ ion are quite intense species, there are significant signals arising from Rh_2N^+, Rh_2O^+, and, to a lesser degree, RhN^+. For this case, the XPS data revealed that at least 90% of the NO is adsorbed molecularly. These fragments must therefore be at least partially created during the ion-induced desorption event. The enhanced fragmentation of NO relative to CO is in line with its slightly weaker bond strength. During thermal desorption, however, the Rh_2NO^+ signal drops in precisely the same fashion as the N 1*s* XPS peak associated with molecular NO, while the RhN^+ ion signal rises to a maximum value at 400 K before falling, mimicking the N 1*s* XPS peak intensity of dissociated NO. Thus, it appears that even though some dissociation during desorption is observed, the molecular specificity of the ejected cluster ions to the chemical state of the surface molecule is preserved. Similar experiments for NO adsorbed onto Rh{331} clearly show that approximately 50% of the molecules dissociate upon adsorption, while the remainder dissociate at higher temperatures before desorption.[206] Thus, the presence of the atomic step on Rh{331} exerts a sufficiently strong effect to influence bond cleavage for NO, but not for CO.

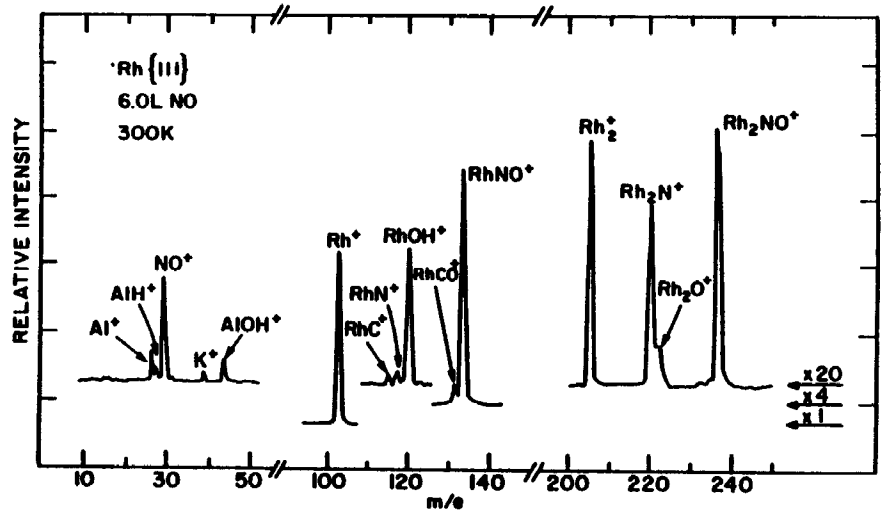

Figure 45. SIMS result of the adsorption of 6.0 L NO on the clean Rh{111} surface at 300 K. Data were taken using a 3-keV Ar^+ ion beam of ~50 pA focused into a 2 × 2-mm spot. The incident angle $\theta_i = 25°$ and the polar collection angle $\theta_d = 20°$ are measured from the surface normal. Molecular bonded NO_{ads} is monitored by the NO^+ (*m/e* 30) $RhNO^+$ (*m/e* 133), and Rh_2NO^+ (*m/e* 236) secondary ions. Dissociated products of NO_{ads} are detected by the Rh_2N^+ (*m/e* 220) and Rh_2O^+ (*m/e* 222) ion yields. Equal amounts of N_{ads} and O_{ads} determined by XPS yield a Rh_2N^+/Rh_2O^+ ion ratio of ~4. Carbon monoxide and H_2O surface contaminants adsorbed from the residual gas are seen as the Rh_2CO^+ and $RhOH^+$ ions. (From Ref. 205.)

From this discussion, it is apparent that the combination of XPS and SIMS is a particularly powerful one. There are always questions regarding quantitation with SIMS, while XPS is especially well suited to evaluating surface concentrations. The major difficulty with XPS, however, is that the BE's are often not highly specific to molecular structure, whereas the cluster ions in SIMS yield detailed compositional information. A good example of this combination is the study of the reduction of NO on a carbon pretreated Rh{331} surface.[207] The XPS measurements for this system yielded significant changes in the shape of the N 1*s* peak assigned to dissociated NO when the surface was heated from room temperature to 500 K. However, the nature of this new N-containing species could not be ascertained from the data. The SIMS spectra, shown in Fig. 46, clearly reveal that the dissociated N atoms are reacting with adsorbed C atoms to produce a surface CN^- species. The ability to characterize the surface chemical behavior of these species in the

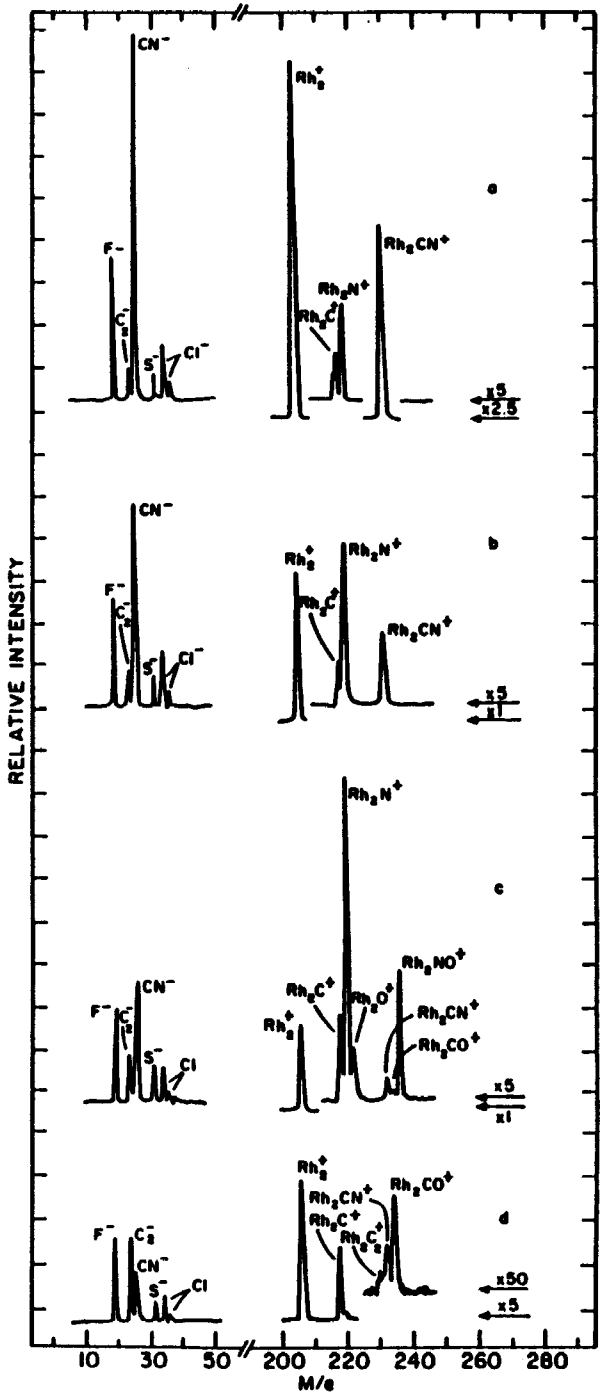

presence of other carbonaceous deposits is, of course, important in many catalytic reactions.

Thus, there are many convincing examples where intact ejection of surface molecular ions can be observed from metal and semiconductor surfaces. There are many hundreds more beyond the scope of this review where even large molecules are seen to desorb intact from a variety of complex matrices ranging from thick films to glycerol. The examples from surface science experiments, however, provide not only useful models for understanding the ion–solid interaction but also add a unique tool to the arsenal of surface analysis techniques which are specific to rather complicated surface molecules.

5.2.2. Molecular Recombination During Ejection

There have been fewer systematic efforts to quantitatively characterize the recombination process predicted by the classical dynamics simulations, perhaps due to the complexities introduced by the presence of the ions themselves. As an example of this problem, consider the case of chemisorbed oxygen on single-crystal transition-metal surfaces. The computer simulations show that O_2 formation is possible by O + O recombination. As for the case of Ni_2 discussed in Section 3.2, the O atoms that comprise the oxygen molecule do not need to be contiguous. If one of the oxygen atoms is ionized as O^+ or O^-, however, then the observed molecule would be O_2^+ or O_2^-. The probability of recombination would then be influenced by the potential surface of the charged molecule. Using these surfaces, the calculated number of dimers differs by less than a factor of 2 for the three cases O_2^+, O_2, and O_2^-. The most interesting aspect of these results, however, is that the thermodynamically most stable species, O_2^+, produces the lowest number of dimers. The reason for this fact is that the range of the potential is the smallest for this species. Apparently, the number of possible two-body interactions that a particular atom might experience is more important than the ultimate stability of a dimer in its equilibrium configuration. If it is possible to generalize this idea further, we would expect oppositely charged species such as Na^+ and Cl^- to have a high probability of forming an NaCl

Figure 46. Static SIMS spectra of the carbon covered Rh(331) surface before and after exposure to NO at 300 K. Heating to 500 K (a) and 400 K (b) produces cyanide as evidenced by the increase of the CN^- and Rh_2CN^+ ion yield. (From Ref. 207.) Exposing the carbon-covered surface to 10 L NO at 300 K results in the spectra shown in (c) Exposure to 10 L C_2H_4 at 300 K and heating to 770 K produces the spectra shown in (d). The carbon residue is evident by the C_2^-, Rh_2C^+, and $Rh_2C_2^+$ ions.

molecule owing to the infinite range associated with purely electrostatic interactions.

A test of the formation of cluster ions by an atom–ion collision mechanism was attempted using the Ni{001} surface during exposure to oxygen.[208] In this case, the ions Ni^+, $NiO^{\pm}$, $O^{\pm}$, and $O_2^{\pm}$ could be monitored as a function of the oxygen dose. The results as shown in Fig. 47 are striking, as the shapes of the ion yield versus coverage curves are quite different depending upon the ion involved. Note, however, that the

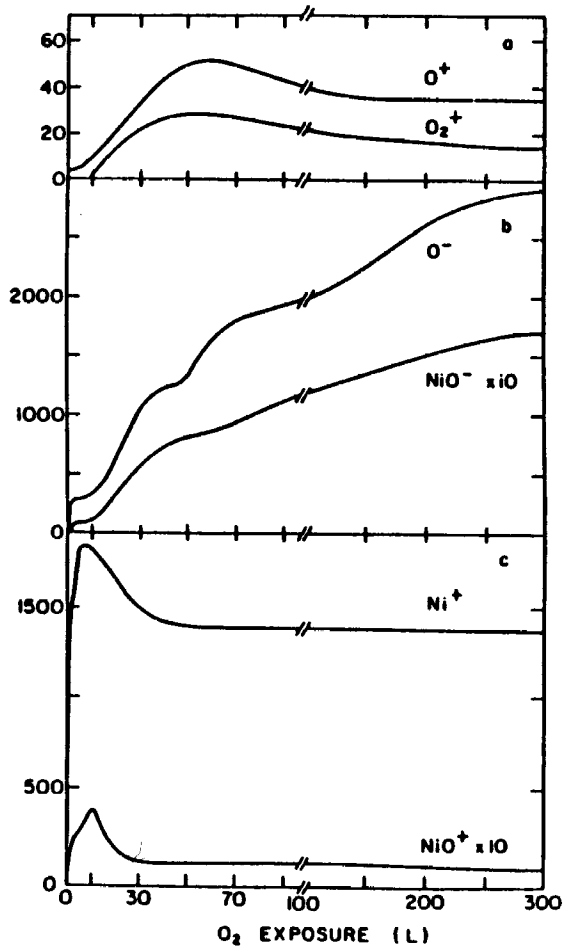

Figure 47. Experimental ion yields versus oxygen exposure for Ni{001} bombarded by 2-keV Ar^+ ions. The ordinate gives the number of ions/s detected. (From Ref. 208.)

NiO^+ yield has a shape similar to the Ni^+ yield whereas the NiO^- and O^- and the O_2^+ and O^+ curves also seem to track each other. If one invokes a cluster formation mechanism as discussed above, then the cluster ions could form as a result of collisions between neutral and ionized atoms. For example, the NiO^+ ion should form by interactions between Ni^+ ions and O atoms. The reaction of Ni atoms and O^+ ions would not be important owing to the low levels of O^+ ions. Furthermore, if the number of ions above the surface is much less than the number of neutrals (which is the case for most materials except perhaps alkali halides), the intensity of the resulting cluster ion will be controlled by the amount of the corresponding atomic ion. Thus for Ni, the clusters would form by the following reaction:

$$Ni^+ + O \xrightarrow[\text{surface}]{} NiO^+ \tag{30}$$

$$Ni + O^- \xrightarrow[\text{surface}]{} NiO^- \tag{31}$$

and

$$O^+ + O \xrightarrow[\text{surface}]{} O_2^+ \tag{32}$$

The mechanism of cluster formation for ions would therefore be very similar to that of the neutrals.

There are other complications that have yet to be checked on single crystals and will only be briefly mentioned here. When Ti is oxidized, a variety of $Ti_xO_y^{\pm}$ cluster ions are observed by SIMS.[209] When the work function of the surface is altered by Cs deposition, the positive cluster ion intensities change in a manner consistent with recombination. The negative ions deviate considerably from the predicted behavior. Yu has proposed, however, that since the electron affinity of negatively charged ions is usually low, unless the cluster constituents are in ground vibrational states electron detachment is very favorable.[210] To produce ground state molecules he feels it is necessary to invoke the condition that they form from nearest neighbors on the surface. Thus for the Ti–oxygen system, Yu proposes that the positive ions form by recombination while the negative ions are produced directly by lattice fragmentation.

To make matters even more complicated, there can be molecular ions formed by electron ejection from neutral molecules. Snowden and co-workers[211] have suggested, for nitrogen implanted into silicon

targets, that during bombardment

$$N + N \xrightarrow[\text{surface}]{} N_2 \rightarrow N_2^+ + e^-$$

This type of mechanism may indeed be quite common since unbound N_2 molecules can be stabilized as N_2^+ by electron ejection. Finally, it has been proposed that large cluster ions may be created through "solvation" of ejecting atomic ions and through a sort of Joule–Thompson condensation mechanism. All of the above ideas merit consideration, although there is yet only scant experimental evidence to back them up.

5.2.3. *Prospects for Detection of Desorbed Neutral Molecules*

There is clearly an intimate relationship between ionization and cluster formation, although the details are elusive. Because of the success of the classical dynamics models it would be valuable to be able to directly monitor the neutral molecules in a manner analogous to that with static SIMS. There have been many attempts at performing such measurements, but most postionization detection schemes are simply not sufficiently sensitive to perform static-mode measurements.

The one exception to this situation involves the use of either resonant or nonresonant laser ionization of the desorbed molecules. So far the MPRI approach has only been applied to desorbed atoms. Recently, however, Becker[212] has studied the adsorption and thermal decomposition of CH_3OH on Ni{110} using 193-nm laser light for nonresonant ionization. The initial data from these experiments are quite encouraging. Using ion doses of $<5 \times 10^{12}/cm^2$ they found several molecular signals in their spectra that were characteristic of surface chemical species. After adsorption of CH_3OH at 120 K, for example, a peak at m/e 32 could be monitored that was clearly associated with the molecular adsorbate. As seen in Fig. 48, as the temperature reaches about 240 K, all of the m/e 32 has disappeared. The slower fall of m/e 13 (—CH) is believed to be associated with the formation of CH_3O_{ads} before this intermediate decomposes to CO. The CO is seen at m/e 28. Although ion-beam-induced fragmentation as well as laser-induced fragmentation are probably both influencing the mass spectra, these experiments yield hopeful indications that static measurements on desorbed neutral molecules will soon be possible.

6. Conclusions and Prospects

In this chapter, we have attempted to present an atomic and molecular view of the interaction of keV particles with solids. The

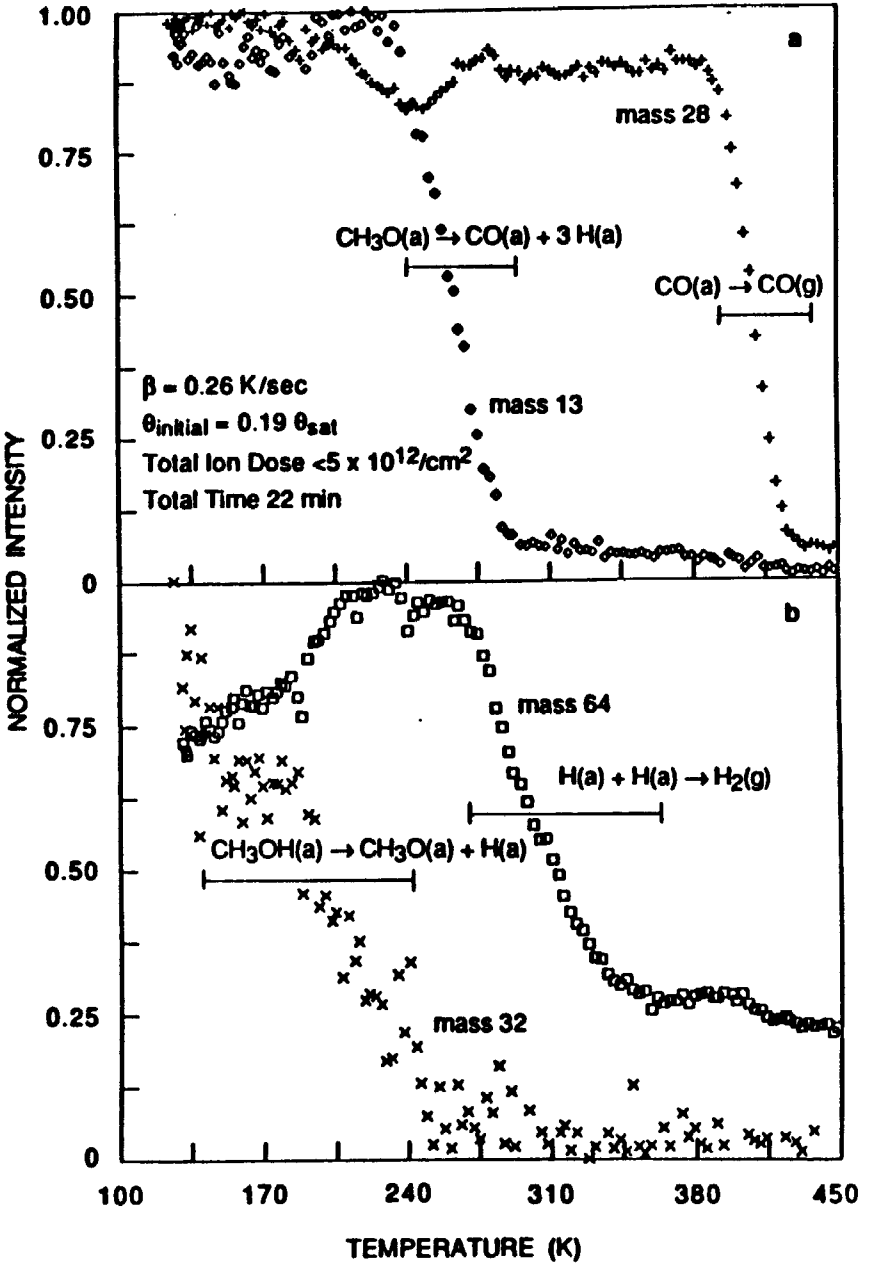

Figure 48. Normalized ion stimulated desorption intensities for masses 13 and 28 (a) and 32 and 64 (b) during a linear temperature ramp of 0.26 K/s following methanol adsorption, $\theta_{initial} = 0.19\ \theta_{sat}$, on Ni(110) at 120 K. Each point consists of an accumulation of 400 spectra obtained at a repetition rate of 40 Hz. The temperature resolution is therefore ~3 K. (From Ref. 212.)

process is clearly a complicated one. In the early days, we were forced to rely on analytical models, with so many approximations that the equations had very little predictive value. At first, the complexity of the atomic motion as seen even on primitive computers using molecular dynamics concepts was discouraging. With the dramatic improvement in computational speed, however, these early approaches have been extended to consume the resources of the most powerful supercomputers. With many-body potentials such as the EAM, accurate computer simulations of this complex process are at hand. Ironically, the massive computer print-outs have led to reasonably simple concepts regarding the important momentum dissipation mechanisms. The advances in the theory of electronic excitation presented here provide an impressive solution to understanding the mixing of the classical motion with other inelastic processes. It is satisfying, indeed, to see such dramatic progress in a field once considered beyond help.

Experimental advances have been equally impressive. The last 15 years or so have seen the ushering in of a new era of surface science. Since the ion–solid interaction event is largely a surface process at keV energies, the advance has had a direct beneficial effect on many fundamental studies. We can now trace the motion of atoms in the solid from their initial positions to their final resting locations. Measurement of the trajectories of state-selected desorbing atoms or molecules, if not yet a *fait accompli*, is at least on the drawing board. The atomic resolution images of the lattice damage provide important new experimental data which must be quantitatively understood.

If there have been great strides in recent years, there is an even more exciting future for this field. Many of the emerging new applications are, of course, outlined extensively in later chapters. The increased fundamental understanding of ion–solid interactions, however, promises new advances in reactive ion etching where the energy in chemical bonds act together with the momentum from the primary ion. The development of TOF detectors and angstrom size ion-beam sources is really in its infancy. Both of these tools should continue to inspire the construction of more sensitive and higher-resolution microscopes. All of these developments may spur another round of technological advances using, for example, ion implantation. We have been working in this general area since 1976. It has been an exciting and challenging 14 years. It is difficult to stray to other research fields.

Acknowledgments

Our venture into the detailed understanding of the ion–solid interactions began in 1977 with our initial collaboration with the late Don E. Harrison, Jr. It is the interaction with Don that led to the further development of the classical dynamics model, and it is the belief in this model that led to the design of many of the experiments described in this chapter. To him we owe our deepest thanks. Throughout the years there have been numerous students and postdoctoral associates that have contributed to the ideas and to the execution of many of the ideas. These collaborators include Che-Chen Chang, Dae-won Moon, Lisa DeLouise, Mark Kaminsky, Robert Levis, Rik Blumenthal, John Olson, Don Brenner, Jung-hui Lin, Curt Reimann, Paul Kobrin, Alan Schick, David Deaven, and Brian Craig. In addition, there are numerous scientists from other institutions that have stimulated and refined our ideas about the particle bombardment process. These investigators include Ming Yu, Peter Williams, Drew Evans, Tom Tombrello, Mark Shapiro, Roger Smith, Roger Kelly, and Stan Williams. Our secretaries, Sabrina Glasgow and Chris Moyer, have graciously spent innumerable hours helping us with this and other projects. Finally we gratefully acknowledge the financial support of the Office of Naval Research, the National Science Foundation, the Air Force Office of Scientific Research, the IBM Program for the Support of the Materials and Processing Sciences, the Shell Development Corporation, the Camille and Henry Dreyfus Foundation, the Sloan Foundation, and the Research Corporation. Three people at these agencies, Henry Blount (NSF), Larry Cooper (ONR), and David Nelson (ONR), have been particularly supportive. Penn State University has supplied a generous grant of computer time for these studies.

References

1. J. F. Zeigler, ed., *Ion Implantation, Science and Technology*, 2nd Ed., Academic Press, Boston (1988).
2. H. F. Winters and J. W. Coburn, *J. Vac. Sci. Technol.* **B3**, 1376 (1985).
3. D. E. Hunton, *Sci. Am.* **261**, 92 (1989).
4. E. M. Sieveka and R. E. Johnson, *Icarus* **51**, 528 (1982).
5. J. J. Thompson, *Phil. Mag.* **20**, 252 (1910).
6. Y. Homma, S. Kurosawa, Y. Yoshioka, M. Shibata, K. Nomura, and Y. Nakamura, *Anal. Chem.* **57**, 2928 (1985).
7. J. M. Chabala, R. Levi-Setti, and Y. L. Wang, *Appl. Surf. Sci.* **32**, 10 (1988).
8. M. J. Bernius and G. H. Morrison, *Rev. Sci. Instrum.* **58**, 1789 (1987).
9. A. Benninghoven, *Phys. Status Solidi* **34**, k169 (1969).
10. M. Barber, R. S. Bordoli, R. D. Sedgewick, and A. N. Tyler, *J. C. S. Chem. Commun.* 325 (1981).
11. I. V. Bletsos, D. M. Hercules, D. Greifendorf and A. Benninghoven, *Anal. Chem.* **57**, 2384 (1985).

12. P. Steffens, E. Niehuis, T. Friese, D. Greifendorf, and A. Benninghoven, *J. Vac. Sci. Technol.* **A3**, 1322 (1985).
13. D. E. Harrison, Jr., P. W. Kelly, B. J. Garrison, and N. Winograd, *Surf. Sci.* **76**, 311 (1978).
14. W. R. Grove, *Trans. R. Soc.* (*London*) **142**, 87 (1852).
15. H. Oechsner and W. Gerhard, *Z. Phy.* **B22**, 41 (1975).
16. D. Lipinsky, R. Jede, O. Ganshow, and A. Benninghoven, *J. Vac. Sci. Technol.* **A3**, 2007 (1985).
17. N. Winograd, J. P. Baxter, and F. M. Kimock, *Chem. Phys. Lett.* **88**, 581 (1982).
18. *Our assumption is that fast atom bombardment or FAB is generically equivalent to ion bombardment. The consequences of the bombardment are most critically dependent on the kinetic energy of the primary particle. Note that a neutral atom differs from its positive ion by the mass of the electron.*
19. G. Carter and J. S. Colligan, *Ion Bombardment of Solids*, American Elsevier, New York (1968).
20. R. E. Honig, *J. Appl. Phys.* **29**, 549 (1958).
21. M. W. Thompson, *Phil. Mag.* **18**, 377 (1968).
22. G. K. Wehner, *Phys. Rev.* **102**, 690 (1956).
23. G. Carter, M. J. Nobes, I. V. Katardjiev, J. L. Whitton, and G. Kiriakidis, *Nucl. Instrum. Methods* **B18**, 529 (1987).
24. A. Benninghoven, D. Jaspers, and W. Sichterman, *Appl. Phys.* **11**, 35 (1976).
25. R. A. Gibbs and N. Winograd, *Rev. Sci. Instrum.* **52**, 1148 (1981).
26. D. Hammer, E. Benes, P. Blum, and W. Husinsky, *Rev. Sci. Instrum.* **47**, 1178 (1976).
27. R. B. Wright, M. J. Pellin, D. M. Gruen, and C. E. Young, *Nucl. Instrum. Methods* **170**, 295 (1980).
28. C. H. Becker and K. T. Gillen, *Appl. Phys. Lett.* **45**, 1063 (1984).
29. P. H. Kobrin, G. A. Schick, J. P. Baxter, and N. Winograd, *Rev. Sci. Instrum.* **51**, 1354 (1986).
30. D. E. Harrison, Jr., *Crit. Rev. Solid State Material Sci* **14**, Suppl. 1, 1–78 (1988).
31. P. Sigmund, *Phys. Rev.* **184**, 383 (1969).
32. P. Sigmund, *Phys. Rev.* **187**, 768 (1969) (Erratum).
33. P. Sigmund, *Rev. Roum. Phys.* **17**, 1079 (1972).
34. P. D. Townsend, *Rad. Effects* **37**, 235 (1978).
35. P. Sigmund, in *Inelastic Ion–Surface Collisions* (N. H. Tolk, J. C. Tully, W. Heiland, and C. W. White, eds.), Academic, New York, p. 121 (1977).
36. I. S. T. Tsong and D. J. Barber, J. Mater. Sci. **8**, 123 (1973).
37. J. Lindhard, V. Nielsen, and M. Scharff, *Mat. Fys. Medd., Dan Vid. Selsk.* **36**(10), (1968).
38. K. S. Kim, W. E. Baitinger, and N. Winograd, *Surf. Sci.* **55**, 285 (1976).
39. D. Almen and G. Bruce, *Nucl. Instrum Methods* **11**, 257 (1961).
40. M. F. Dumke, T. A. Tombrello, R. A. Weller, R. M. Housley, and E. H. Cirlin, *Surf. Sci.* **124**, 403 (1983).
41. H. H. Andersen, B. Stenum, T. Sorensen, and H. J. Whitlow, *Nucl. Instrum. Methods* **B6**, 459 (1985).
42. S. Kundu, D. Ghose, D. Basu, and S. B. Karmohapatro, *Nucl. Instrum. Methods* **B12**, 352 (1985).
43. J. P. Baxter, G. A. Schick, J. Singh, P. H. Kobrin, and N. Winograd, *J. Vac. Sci. Technol.* **4**, 1218 (1986).
44. G. A. Schick, J. P. Baxter, J. Singh, P. H. Kobrin, and N. Winograd, in: *Secondary Ion Mass Spectrometry*—SIMS V, Springer Series in Chemical Physics Vol. **44**, p. 90, Springer-Verlag, New York (1986).

45. N. Winograd, P. H. Kobrin, G. A. Schick, J. Singh, J. P. Baxter, and B. J. Garrison, *Surf. Sci. Lett.* **176**, L817 (1986).
46. J. P. Baxter, J.. Singh, G. A. Schick, P. H. Kobrin, and N. Winograd, *Nucl. Instrum. Methods* **B17**, 300 (1986).
47. B. J. Garrison, *Nucl. Instrum. Methods* **B17**, 305 (1986).
48. B. J. Garrison, *Nucl. Instrum. Methods B* **40/41**, 313 (1989).
49. D. Y. Lo, M. H. Shapiro, T. A. Tombrello, B. J. Garrison, and N. Winograd, *Proc. Matl. Res. Soc. Mtg.* **74**, 449 (1987).
50. W. Husinsky, *J. Vac. Sci. Technol.* **B3**, 1546 (1985).
51. B. J. Garrison, N. Winograd, D. Lo, T. A. Tombrello. M. H. Shapiro, and D. E. Harrison, Jr., *Surf. Sci. Lett.* **180**, L129 (1987).
52. R. Kelly, *Nucl. Instrum. Methods* **B18**, 388 (1987).
53. G. Falcone, R. Kelly, and A. Oliva, *Nucl. Instrum. Methods* **B18**, 399 (1987).
54. D. P. Jackson, *Radiat. Effects* **18**, 185 (1973).
55. D. P. Jackson, *Can. J. Phys.* **53**, 1513 (1975).
56. M. H. Shapiro, *Nucl. Instrum. Methods B*, **42**, 290 (1989).
57. G. Falcone, *Surf. Sci.* **187**, 1212 (1987).
58. G. Falcone and F. Gullo, *Phys. Lett. A* **125**, 432 (1987).
59. G. Falcone, *Phys. Lett. A* **129**, 188 (1988).
60. C. T. Reimann, M. El-Maazawi, K. Walzl, B. J. Garrison, and N. Winograd, *J. Chem. Phys.* **90**, 2027 (1989).
61. See, for example, D. G. Truhlar and J. T. Muckerman, in *Atom Molecule Collision Theory* (R. B. Berstein, ed), Plenum Press, New York (1979).
62. See, for example, P. Lykos, ed., *ACS Symp. Ser.*, No. 86 (1978).
63. D. W. Brenner and B. J. Garrison, *Adv. Chem. Phys.*, **281**, (1989).
64. D. J. Rossky and M. Karplus, *J. Am. Chem. Soc.* **101**, 1913 (1979).
65. R. Smith and D. E. Harrison, Jr., *Computers in Physics*, Sep/Oct, 68 (1989).
66. B. J. Garrison, C. T. Reimann, N. Winograd, and D. E. Harrison, Jr., *Phys. Rev. B* **36**, 3516 (1987).
67. B. J. Garrison, N. Winograd, D. M. Deaven, C. T. Reimann, D. Y. Lo, T. A. Tombrello, and M. H. Shapiro, *Phys. Rev. B* **37**, 7197 (1988).
68. B. J. Garrison, *J. Am. Chem. Soc.* **102**, 6553 (1980); **104**, 6211 (1982).
69. S. A. Adelman, *Adv. Phys.* **44**, 143 (1980).
70. J. C. Tully, *J. Chem. Phys.* **73**, 1975 (1980).
71. R. A. Stansfield, K. Broomfield, and D. C. Clary, *Phys. Rev. B* **39**, 7680 (1989).
72. F. H. Stillinger and T. A. Weber, *Phys. Rev. B* **31**, 5262 (1985)
73. P. C. Zalm, *J. Appl. Phys.* **54**, 2660 (1983).
74. W. Ens, R. Beavis, and K. G. Standing, *Phys. Rev. Lett.* **50**, 27 (1983).
75. J. E. Huheey, *Inorganic Chemistry*, Harper and Row, New York (1978).
76. R. S. Bardoli, J. C. Vickerman, and J. Wolstenholme, *Surf. Sci.* **85**, 244 (1979).
77. N. Winograd, B. J. Garrison, and D. E. Harrison, Jr., *J. Chem. Phys.* **73**, 3473 (1980).
78. S. P. Holland, B. J. Garrison, and N. Winograd, *Phys. Rev. Lett.* **44**, 756 (1980).
79. K. E. Foley and B. J. Garrison, *J. Chem. Phys.* **72**, 1018 (1980).
80. M. T. Robinson and I. M. Torrens, *Phys. Rev. B* **9**, 5008 (1974).
81. R. P. Webb and D. E. Harrison, Jr., *Phys. Rev. Lett.* **50**, 1478 (1983).
82. I. H. Wilson, N. J. Zheng, U. Knipping, and I. S. T. Tsong, *Appl. Phys. Lett.* **53**, 2039 (1988).

83. E. Pearson, T. Takai, T. Halicioglu, and W. A. Tiller, *J. Crystal Growth* **70**, 33 (1984).
84. D. W. Brenner and B. J. Garrison, *Phys. Rev. B* **34**, 1304 (1986).
85. J. Tersoff, *Phys. Rev. Lett.* **56**, 632 (1986).
86. R. Biswas and D. R. Hamann, *Phys. Rev. Lett.* **55**, 2001 (1985).
87. J. B. Gibson, A. N. Goland, M. Milgrim, and G. H. Vineyard, *Phys. Rev.* **120**, 1229 (1960).
88. D. E. Harrison, Jr., W. L. Moore Jr., and H. T. Holcombe, *Radiat. Effects* **17**, 167 (1973).
89. M. H. Shapiro, P. K. Haff, T. A. Tombrello, D. E. Harrison, Jr., and R. P. Webb, *Radiat. Effects* **89**, 234 (1985).
90. V. E. Yurasova, A. A. Sysoev, G. A. Samsonov, V. M. Bukhanov, L. N. Nevzovova, and L. B. Shelyakin, *Radiat. Effects* **20**, 89 (1973).
91. J. P Biersack and L. G. Haggmark, *Nucl. Instrum. Methods* **174**, 257 (1980).
92. J. P. Biersack and W. Eckstein, *Appl. Phys. A* **34**, 73 (1984).
93. I. M. Torrens, *Interatomic Potentials*, Academic, New York (1972).
94. E. P. Th. M. Suurmeijer and A. L. Boers, *Surf. Sci.* **43**, 309 (1973).
95. C. C. Chang, N. Winograd, and B. J. Garrison, *Surf. Sci.* **202**, 309 (1988).
96. L. Brewer and G. M. Rosenblatt, *Adv. High Temp. Chem.* **2**, 1 (1969).
97. K. P. Huber and G. Hertzberg, *Constants of Diatomic Molecules*, Van Nostrand Reinhold Company (New York, 1979).
98. M. S. Daw and M. I. Baskes, *Phys. Rev. B* **29**, 6443 (1984).
99. S. M. Foiles, M. I. Baskes, and M. S. Daw, *Phys. Rev. B* **33**, 7983 (1986).
100. M. S. Daw, *Surf. Sci.* **166**, L161 (1986).
101. F. Ercolessi, E. Tosatti, and M. Parrinello, *Phys. Rev. Lett.* **57**, 719 (1986).
102. F. Ercolessi, M. Parrinello, and E. Tosatti, *Surf. Sci.* **177**, 314 (1986).
103. M. Garofalo, E. Tosatti, and F. Ercolessi, *Surf. Sci.* **188**, 321 (1987).
104. D. Tomanek and K. H. Bennemann, *Surf. Sci.* **163**, 503 (1985).
105. B. W. Dodson, *Phys. Rev. B* **35**, 880 (1987).
106. S. P. Chen, A. F. Voter, and D. J. Srolovitz, *Phys. Rev. Lett.* **57**, 1308 (1986).
107. S. M. Foiles, *Phys. Rev. B* **32**, 7685 (1986).
108. T. E. Felter, S. M. Foiles, M. S. Daw, and R. H. Stullen, *Surf. Sci.* **171**, L379 (1986).
109. D. M. Deaven, Honors Thesis, The Pennsylvania State University, (1988).
110. J. M. Eridon and S. Rao, *Mat. Res. Soc. Symp. Proc.* **141**, 285 (1989).
111. *Atomic Scale Calculations in Mateirals Science*, Mat. Res. Soc. Symp. Proc., Vol. 141 (1989).
112. M. I. Baskes, *Phys. Rev. Lett.* **59**, 2666 (1987).
113. C. T. Reimann, M. El-Maazawi, K. Walzl, B. J. Garrison, and N. Winograd, *J. Chem. Phys.* **90**, 2027 (1989).
114. D. Y. Lo, T. A. Tombrello, M. H. Shaprio, B. J. Garrison, N. Winograd, and D. E. Harrison, Jr., *J. Vac. Sci. Technol.* **A6(3)**, 708 (1988).
115. N. Sathyamurthy, *Computer Phys. Rep.* **3**, 1 (1985) and references therein.
116. J. N. Murrell, S. Carter, S. C. Farantos, P. Huxley, and A. J. C. Varandas, *Molecular Potential Energy Functions*, Wiley, New York (1984) and references therein.
117. K. E. Khor and S. Das Sarma, *Phys. Rev. B* **36**, 7733 (1987).
118. F. F. Abraham and I. P. Batra, *Surf. Sci.* **163**, L752 (1985).
119. B. M. Axilrod and E. Teller, *J. Chem. Phys.* **11**, 299 (1943).
120. P. M. Agrawal, L. M. Raff, and D. L. Thompson, *Surf. Sci.* **188**, 402 (1987).
121. J. Tersoff, *Phys. Rev. B* **37**, 6991 (1988).
122. B. W. Dodson, *Phys. Rev. B* **35**, 2795 (1987).

123. G. C. Abell, *Phys. Rev. B* **31**, 6184 (1985).
124. K. Ding and H. C. Anderson, *Phys. Rev. B* **34**, 6987 (1986).
125. M. H. Grabow and G. H. Gilmer, in *Initial States of Epitaxial Growth*, (J. M. Gibson, R. Hull, and D. A. Smith, eds), Materials Research Society, Pittsburgh (1987), p. 15.
126. R. Smith, D. E. Harrison, Jr., and B. J. Garrison, *Phys. Rev. B*, **40**, 93 (1989).
127. J. T. Muckerman, *J. Chem. Phys.* **57**, 3388 (1972).
128. J. H. McCreery and G. Wolken, *J. Chem. Phys.* **63**, 2340 (1975).
129. A. Gelb and M. Cardillo, *Surf. Sci.* **59**, 128 (1976).
130. A. Gelb and M. Cardillo, *Surf. Sci.* **64**, 197 (1977).
131. A. Gelb and M. Cardillo, *Surf. Sci.* **75**, 199 (1977).
132. A. Kara and A. E. DePristo, *J. Chem. Phys.* **88**, 2033 (1988).
133. J.-H. Lin and B. J. Garrison, *J. Chem. Phys.* **80**, 2904 (1984).
134. J. C. Tully, *J. Chem. Phys.* **73**, 6333 (1980).
135. D. Brenner, C. T. White, M. L. Elert, and F. E. Walker, *Int. J. Quantum Chem.*, **23**, 333 (1989).
136. S. M. Foiles, *Surf. Sci.* **191**, L779 (1987).
137. B. W. Dodson, *Phys. Rev. Lett.* **60**, 2288 (1988).
138. D. W. Brenner and B. J. Garrison, *Surf. Sci.* **198**, 151 (1988).
139. B. J. Garrison, M. T. Miller, and D. W. Brenner, *Chem. Phys. Lett.* **146**, 553 (1988).
140. D. Srivastava, B. J. Garrison, and D. W. Brenner, *Phys. Rev. Lett.*, **63**, 302 (1989).
141. B. J. Garrison, *Surf. Sci.* **167**, L225 (1986).
142. K. Wittmaack in, *Inelastic Ion–Surface Collisions* (N. H. Tolk, J. C. Tully, W. Heiland, and C. W. White, eds.) Academic, New York (1977), p. 153.
143. P. Williams, *Surf. Sci.* **90**, 588 (1979).
144. G. Blaise and A. Nourtier, *Surf. Sci.* **90**, 495 (1979).
145. G. Soldzian, *Phys. Scr.* **T6**, 54 (1983).
146. P. Williams, *Appl. Surf. Sci.* **13**, 241 (1982).
147. M. L. Yu and N. D. Lang, *Nucl. Instrum. Methods Phys. Res.* **B14**, 403 (1986).
148. M. L. Yu, *Nucl. Instrum. Methods Phys. Res.* **B18**, 542 (1987).
149. Z. Sroubek, *SIMS VI* (A. Benninghoven, A. M. Huber, and H. W. Werner, eds.), J. Wiley, New York (1987), p. 17.
150. M. L. Yu, *SIMS VI* (A. Benninghoven, A. M. Huber, and H. W. Werner, eds.) J. Wiley, New York (1987), p. 4.
151. N. D. Lang, *Phys. Rev. B* **27**, 2019 (1983).
152. A. Blandin, A. Nourtier, and D. W. Hone, *J. Phys.* **37**, 396 (1976).
153. J. K. Norskov and B. I. Lundqvist, *Phys. Rev. B* **19**, 5661 (1979).
154. R. Brako and D. M. Newns, *Surf. Sci.* **108**, 253 (1981).
155. M. L. Yu and N. D. Lang, *Phys. Rev. Lett.* **50**, 127 (1983).
156. M. L. Yu, *Phys. Rev. Lett.* **47**, 1325 (1981).
157. G. A. v.d. Schootbrugge, A. G. J. de Wit, and J. M. Fluit, *Nucl. Instrum. Methods* **132**, 321 (1976).
158. M. Bernheim, and F. LeBourse, *Nucl. Instrum. Methods Phys. Res.* **B27**, 94 (1987).
159. M. J. Vasile, *Phys. Rev. B* **29**, 3785 (1984).
160. R. G. Hart and C. B. Cooper, *Surf. Sci.* **94**, 105 (1980).
161. A. R. Krauss and D. M. Gruen, *Surf. Sci.* **92**, 14 (1980).
162. R. A. Gibbs, S. P. Holland, K. E. Foley, B. J. Garrison, and N. Winograd, *J. Chem. Phys.* **76**, 684 (1982).
163. J.-H. Lin and B. J. Garrison, *J. Vac. Sci. Technol A* **1**(2), 1205 (1983).
164. A. Nourtier, J. P. Jardin, and J. Quazza, *Phys. Rev. B* **37**, 10628 (1988).
165. L. Landau, *Z. Phys. Sov.* **2**, 46 (1932); C. Zener, *Proc. R. Soc.* **A137**, 696 (1932).

166. K. Mann and M. L. Yu, *SIMS V*, Springer Series in Chemical Physics (A. Benninghoven, R. J. Colton, D. S. Simons, and H. W. Werner, eds.), Springer-Verlag, New York (1986), p. 26.
167. M. L. Yu and K. Mann, *Phys. Rev. Lett.* **57**, 1476 (1986).
168. M. L. Yu, D. Grischkowsky, and A. C. Balant, *Phys. Rev. Lett.* **48**, 427 (1982).
169. W. Husinsky, G. Betz, and I. Girgis, *Phys. Rev. Lett.* **50**, 1689 (1983).
170. B. Schweer and H. L. Bay, *Appl. Phys. A* **29**, 53 (1982).
171. M. J. Pellin, R. B. Wright, and D. M. Gruen, *J. Chem. Phys.* **74**, 6448 (1981).
172. C. E. Young, W. F. Callaway, M. J. Pellin, D. M. Gruen, *J. Vac. Sci. Technol. A* **2**, 693 (1984).
173. B. I. Craig, J. P. Baxter, J. Singh, G. A. Schick, P. H. Kobrin, B. J. Garrison, and N. Winograd, *Phys. Rev. Lett.* **57**, 1351 (1986).
174. B. I. Craig and B. J. Garrison, unpublished.
175. C. Reimann and N. Winograd, unpublished results.
176. S. P. Holland, B. J. Garrison, and N. Winograd, *Phys. Rev. Lett.* **43**, 220 (1979).
177. S. Kono, C. S. Fadley, N. F. T. Hall, and Z. Hussain, *Phys. Rev. Lett.* **41**, 117 (1978).
178. D. W. Moon, R. J. Bleiler, and N. Winograd, *J. Chem. Phys.* **85**, 1097 (1986).
179. E. Zanazzi, F. Jona, D. W. Jepsen, and P. M. Marcus, *Phys. Rev. B* **14**, 432 (1976).
180. M. J. Cardillo, G. E. Becker, D. R. Hamann, J. A. Serri, L. Whitman, and L. F. Mattheiss, *Phys. Rev. B* **28**, 494 (1983).
181. P. H. Citrin, D. R. Hamann, L. F. Mattheiss, and J. E. Rowe, *Phys. Rev. Lett.* **49**, 1712 (1982).
182. S. P. Weeks and J. E. Rowe, *Solid State Commun.* **27**, 885 (1978).
183. C. C. Chang and N. Winograd, *Surf. Sci.*, **230**, 27 (1990).
184. D. W. Moon, R. J. Bleiler, E. J. Karwacki, and N. Winograd, *J. Am. Chem. Soc.* **105**, 2916 (1983).
185. D. W. Moon, N. Winograd, and B. J. Garrison, *Chem. Phys. Lett.* **114**, 237 (1985).
186. J. E. Demuth, K. Christmann, and P. N. Sanda, *Chem. Phys. Lett.* **76**, 201 (1980).
187. R. Dudde, E. E. Koch, N. Ueno, and R. Engelhardt, *Surf. Sci.* **178**, 646 (1986).
188. C. C. Chang, G. P. Malafsky,and N. Winograd, *J. Vac. Sci. Technol A* **5**, 981 (1987).
189. J. F. Van der Veen, *Surf. Sci. Rep.* **5**, 199 (1985).
190. J. A. Yarmoff and R. S. Williams, *Surf. Sci.* **127**, 461 (1983).
191. C.-C. Chang and N. Winograd, *Phys. Rev. B* **39**, 3467 (1989).
192. Y. Kuk and L. C. Feldman, *Phys. Rev. B* **30**, 5811 (1984).
193. N. Winograd and C.-C. Chang, *Phys. Rev. Lett.* **61**, 2568 (1989).
194. D. J. Holmes, N. Panagiotides, C. J. Barnes, R. Dus, D. Norman, G. M. Lamble, F. Della Valle, and D. A.King, *J. Vac. Sci. Technol. A* **5**(4), 703 (1987).
195. Rik Blumenthal, S. K. Donner, J. L. Herman, Rajender Trehan, K. P. Caffey, B. D. Weaver, Ehud Furman, and Nicholas Winograd, *J. Vac. Sci. Technol B* **6**, 1444 (1988).
196. C. M. Greenlief, S. M. Gates, and P. A. Holbert, *Chem. Phys. Lett.* **159**, 202 (1989).
197. M. P. Kaminsky, N. Winograd, G. L. Geoffroy, and M. A. Vannice, *J. Am. Chem. Soc.* **108**, 1315 (1986).
198. R. J. Levis, J. Zhicheng and N. Winograd, *J. Am. Chem. Soc.*, **111**, 4605 (1989).
199. J. R. Creighton and J. M. White, *Surf. Sci.* **129**, 327 (1983).
200. R. J. Levis, Z. C. Jiang, N. Winograd, S. Akhter, and J. M. White, *Catalysis Lett.* **1**, 385 (1988).
201. S. Akhter and J. M. White, *Surf. Sci.* **167**, 101 (1986).
202. M. A. Henderson, P. L. Radloff, J. M. White, and C. A. Mims, *J. Phys. Chem.* **88**, 4111 (1988).

203. M. A. Henderson, P. L. Radloff, C. M. Greenlief, J. M. White, and C. A. Mims, *J. Phys. Chem.*, **88**, 4120 (1988).
204. L. L. Lauderback and W. N. Delgass, *Phys. Rev. B* **26**, 5258 (1982).
205. L. A. DeLouise, E. White, and N. Winograd, *Surf. Sci.* **147**, 252 (1984).
206. L. A. DeLouise and N. Winograd, *Surf. Sci.* **159**, 199 (1985).
207. L. A. DeLouise and N. Winograd, *Surf. Sci.* **154**, 79 (1985).
208. N. Winograd, B. J. Garrison, T. Fleisch, W. N. Delgass, and D. E. Harrison, Jr., *J. Vac. Sci. Technol.* **16**, 629 (1979).
209. M. L. Yu, *Phys. Rev. B*, **26**, 4731 (1982).
210. M. L. Yu, *Appl. Surf. Sci.*, **11/12**, 196 (1982).
211. K. J. Snowden, W. Heiland, and E. Taglauer, *Phys. Rev. Lett.* **46**, 284 (1981).
212. J. J. Vajo, J. H. Campbell, and C. H. Becker, *J. Am. Vac. Soc. A*, **7**, 1949 (1989).